TOWARDS POPULATION BASED CHARACTERIZATION OF NEURONAL FIBER PATHWAYS WITH DIFFUSION TENSOR IMAGING

By

Qing Xu

Dissertation

Submitted to the Faculty of the

Graduate School of Vanderbilt University

in partial fulfillment of the requirements

for the degree of

DOCTOR OF PHILOSOPHY

in

Electrical Engineering

August, 2010

Nashville, Tennessee

Approved:

Professor Zhaohua Ding

Professor Adam W. Anderson

Professor Benoit Dawant

Professor Mark D. Does

Professor D. Mitchell Wilkes

Copyright © 2010 by Qing Xu

All Rights Reserved

ACKNOWLEDGEMENTS

I am extremely fortunate to be supervised by such a great committee, including Dr. Zhaohua Ding, Dr. Adam W. Anderson, Dr. Benoit Dawant, Dr. Mark D. Does and Dr. D. Mitchell Wilkes. Without their continuous supports and guidance this dissertation would not be possible. My thanks firstly go to my advisor, Dr. Zhaohua Ding, who has been pioneering the research in diffusion tensor image processing. Since the summer in 2006 he has been spending a huge amount of time on coaching and inspiring me. I still remember the first meeting with him, where he showed me brilliant ideas, a clear roadmap, and made me confident and even enthusiastic about the future. I also cannot forget the uncountable meetings, where he taught me how to be creative, how to write, how to formulate, and how to prove ideas with experiments. All these merits that I have learned from him will benefit my entire life no matter what field I will work on. I would also like to thank Dr. Adam W. Anderson, who has a long history of extraordinary research in brain imaging. Without his help on the reconstruction of diffusion tensors, all the following post-processing work on neuronal fibers would not be possible. More importantly, his insight in brain and MR imaging help me to understand the big picture of the whole neuroimaging field. I also feel very lucky to have Dr. Benoit Dawant, one of the most famous experts in the image registration field, in my committee. His lectures on non-rigid transformation and registration inspired my strong interest in this field, which later become an integral part in my dissertation. Dr. Mark D. Does, the real expert in NMR and small animal imaging technology, also has been very supportive to my research. I would like to thank him for the generous advices and encouragement. I also

want to thank Dr. D. Mitchell Wilkes, who has been teaching the EECE core class, random process. It is in his class, where I learned the Bayesian theory and estimation method that later becomes the theoretical foundation of my work. I really appreciate his deep but clear explanation of these theories.

This work would not have been possible without the financial support of the Vanderbilt University Institute of Imaging Science, the Department of Electrical Engineering or the Medical Center Department of Radiology and Radiological Sciences.

Qing Xu

May 25, 2010

Table of Contents

Page

ACKNOWLEDGEMENTS……...iii

LIST OF TABLES ……...……...viii

LIST OF FIGURES…….……..ix

Chapter

I. INTRODUCTION 1
Diffusion MRI 2
Diffusion weighted imaging (DWI) 2
Diffusion tensor imaging (DTI) 3
High angular resolution diffusion imaging (HARDI) 4
White matter fiber tracking 5
Deterministic fiber tracking 5
Probabilistic fiber tracking 7
Fiber bundle segmentation 8
Manual segmentation 9
Clustering based segmentation 9
Atlas based segmentation 11
DTI image and fiber registration 11
Image-based registration 12
Feature-based registration 13
Contributions 14

II. STATISTICAL FIBER BUNDLE MODEL 16
Vector representation for fiber 16
Uniform resampling 16
Closest point resampling 19
Statistical models for fiber bundle 22
Gaussian model 22
Gamma model 24
Evaluations 26
Conclusions 30

III. UNIFIED FIBER BUNDLING AND REGISTRATION: THOERY AND METHODS 32

Introduction 33
Problem formulation 34
MAP estimation 35
Optimization 38
Transformation 43
Estimation of rigid transformation 43
Estimation of a TPS transformation 46
Coarse-to-fine registration 48
Outline of the UFIBRE algorithm 48
A 2D example 50
Conclusions and Discussions 53

IV. UNIFIED FIBER BUNDLING AND REGISTRATION: EVALUATIONS 57

Experiment and evaluation methods 57
Imaging 57
Fiber reconstruction 57
Bundle selection 58
Performance evaluation 58
Atlas construction 61
Results 61
Performance evaluations 61
WM fiber atlas construction 71
Conclusions 73

V. GREY MATTER PARCELLATION CONSTRAINED FULL BRAIN BUNDLING 74

Introduction 74
Methods 76
Uncertainties 77
Cortex projection model 78
Cortex projection bundle model 79
Objective function 80
EM algorithm 81
Implementation issues 83
Experiments and results 83
Grey matter parcellation template 83
Imaging and fiber tracking 84
Registration of AAL mask with fibers 85
Metrics 86
Convergence 87
Effect of the cortex projection variance 87
Comparisons with baseline methods 90
Demonstrations of resulting bundles 93

Conclusions 96

VI. CONSISTENT GROUP-WISE BUNDLING 98
Introduction 98
Methods 100
Objective function 100
Optimization 101
Experiments and results 103
Baseline methods 104
Metrics 105
Results 105
Demonstration of resulting bundles 106
Conclusions 109

VII. CONCLUSIONS 110

REFERENCES 113

LIST OF TABLES

Table **Page**

Table 4.1 Statistics of Dice's coefficient for nine fiber bundles over the seven subjects using the UFIBRE with $C = 0.5$. 71

Table 4.2 Statistics of RMSE for nine fiber bundles over the seven subjects using the UFIBRE with C = 0.5 (unit: voxel)..... 71

Table 5.1 The list for all ROI definitions in the AAL mask. 91

Table 6.1 The MGIV and MBCD for all of the four bundling methods. 112

LIST OF FIGURES

Figure **Page**

Figure 2.1 A demonstration of uniform resampling for the bundle connecting the left and the right superior frontal gyrus. 18

Figure 2.2 A demonstration of incorrect point correspondence caused by uniform sampling 19

Figure 2.3 A demonstration of closest point resampling for the bundle connecting the left and the right superior frontal gyrus. 21

Figure 2.4 A comparison of the closest point and the uniform resampling for two fibers far away from each other 22

Figure 2.5 A demonstration of the Gaussian model for the bundle connecting the left and the right superior occipital gyrus. 24

Figure 2.6 Gamma distributions with different parameters. 25

Figure 2.7 The curve of average log likelihoods with respect to type of bundles. 29

Figure 2.8 Histograms of distances between fibers and their centroids for two fiber bundles. 30

Figure 3.1 Illustrations of the optimization process of the proposed UFIBRE algorithm with a simple 2D example 51

Figure 4.1 Variations of the mean overall Dice's coefficient and RMSE with respect to the weighting factor C. 62

Figure 4.2 Superimposition of the template and target fiber bundles on the FA map of the target data. 66

Figure 4.3 Comparisons between ground truth obtained by manual segmentation and the bundles estimated by the UFIBRE algorithm for one typical dataset. 67

Figure 4.4 Comparisons between F and $\overline{F}$ along bundles 70

Figure 4.5 A 3D view of the constructed bundle atlas from the template and seven target datasets 72

Figure 5.1 The axial view of a whole volume fiber set. 85
Figure 5.2 The variations of the number of fiber-to-bundle assignment changes with respect to the iteration index for all ten subjects. 87

Figure 5.3 The variations of numbers of iterations for convergences, the MIV, and the MED with respect to the cortex projection variance value. 89

Figure 5.4 Illustrative comparisons between the proposed algorithm and the baseline methods.. 92

Figure 5.5 The MIV and the MED for the proposed parcellation constrained bundling and the two baseline methods. 93

Figure 5.6 Saggital, axial and coronal view of the full brain bundling results using the proposed parcellation constrained approach. 96

Figure 6.1 Overlapping an individual fiber set on the MNI template. 104

Figure 6.2 Saggital, axial and coronal view of the full brain bundling results using the proposed parcellation constrained approach……109

CHAPTER I

INTRODUCTION

As one of the two major components in the human central nervous system, white matter, which is mainly composed of myelinated axons, connects gray matter in different cortical areas (Dale et al., 2008). The whole central nervous system can be viewed as a computer network, where gray matter is analogous to individual computing processors and white matter to network cables that connect computers. Some evidences indicate that structural abnormalities of white matter connection can cause serious brain diseases, e.g., it has been long believed that the white matter fibers that connect frontal and temporal lobes are abnormal in patients with schizophrenia (Wernicke, 1906; Kraepelin, 1919/1971; Kubicki et al., 2007). To better understand how exactly the structure of white matter connection is related to these mental disorders, it is necessary to have theoretically sound and practically robust methods that can reliably locate specific connections and compare these connections in normal subjects to patients with those disorders.

The *in vivo* reconstruction of white matter connection or fibers was not practicable until the recent introduction of diffusion based magnetic resonance imaging (MRI) (Stejskal and Tanner, 1965; Le Bihan et al., 1986; Basser, 1994; Tuch et al., 2003, Anderson, 2005). For each voxel, diffusion MRI can measure diffusion strength along a certain direction (diffusion weighted imaging), or even provide a diffusion tensor that describes the full three dimensional diffusion profile (diffusion tensor imaging). As axons in white

matter are covered with myelin, which serves as a barrier that constrains diffusion, water molecules in white matter tend to diffuse more significantly in the direction of the medial axis of neuronal fibers than in their cross section plane. Based on this fact the diffusion tensor can be used to reconstruct neural fibers. For example, a simple streamline scheme may start from some seed points and follow the major eigenvectors of tensors (eigenvectors with the largest eigenvalue) to generate representations of neural fibers (Basser et al., 2000; Mori et al., 2002). These fibers provide information about the white matter structure, which can be used for studying neural connectivity and detecting structural defects in patients with brain diseases.

For reliable analysis and characterization, the neural fibers are usually grouped into a set of bundles with anatomical correspondence and structural coherence. To make group comparison possible, bundles from different subjects need to be co-registered or spatially normalized (Jones et al., 2002; Wakana et al., 2004). The central contributions of this work is to solve the above two problems, fiber bundling and alignment.

1. Diffusion MRI

Diffusion MRI is capable of measuring local diffusion properties of tissue *in vivo* at a voxel level.

A. Diffusion weighted imaging (DWI)

DWI can generate a scalar image with contrast attenuated by tissue diffusivities. A pair of diffusion weighting field gradients are used in the image acquisition. The first gradient causes different phase shifts of molecules at different locations. Then the second gradient is applied to cancel out the phase differences by giving equal and opposite phase shifts. However, the phase differences can't be completely removed due to molecules' random

movement, diffusion. Molecules with less diffusion generate signal with less attenuation, leading to brighter intensities in reconstructed images. Let r denote the one-dimensional coordinate of a molecule in the gradient direction. Based on the assumption of a Gaussian diffusion, the probability density function (pdf) of a molecule's displacement r after time t can be expressed as follows,

$$P(r) = \frac{1}{\sqrt{4\pi D_{eff} t}} \exp(-\frac{r^2}{4D_{eff} t}), \tag{1.1}$$

where D_{eff} is the effective diffusivity of local tissue. Stejskal and Tanner (1965) showed that the DWI signal S can be related to the baseline signal S_0 generated in the absence of the gradient pair based on the below equation,

$$\frac{S}{S_0} = \exp(-bD_{eff}), \tag{1.2}$$

where the parameter b (diffusion weighting factor) incorporates information relevant to the diffusion weighting gradients such as gradient magnitude and time duration of applying the gradients (Le Bihan et al., 1986).

B. Diffusion tensor imaging (DTI)

For anisotropic tissue, which has different diffusivities in different directions, one DWI image only gives a projection of complete three dimensional diffusion profiles along a certain orientation. The pdf $P(r)$ in Equation 1.1 can be generalized to a three-dimensional (3D) Gaussian model $P(\mathrm{r})$ as follows,

$$P(\mathbf{r}) = \frac{1}{(2\pi)^{3/2} \mid 2\mathbf{D}t \mid^{1/2}} \exp(-\frac{\mathbf{r}\mathbf{D}^{-1}\mathbf{r}^T}{4t}), \tag{1.3}$$

where **r** denotes a three dimensional displacement and **D** is a diffusion tensor (3×3 positive definite matrix). To measure the tissue diffusion tensor, Basser (1994) generalized Equation 1.2 to,

$$\frac{S}{S_0} = \exp(-\sum_{i,j} \mathbf{b}_{i,j}\mathbf{D}_{i,j}), \quad (1.4)$$

where **b** is a matrix carrying information about the diffusion weighting gradients. Since **D** has six distinct components, at least six measurements with different diffusion weighting gradients are needed in order to construct a set of equations for estimating an underlying **D**.

C. High angular resolution diffusion imaging (HARDI)

A Gaussian pdf $P(\mathbf{r})$ may not be always assumed, particularly in the place where white matter (WM) fibers cross. Several approaches have recently been proposed to characterize non-Gaussian diffusion distributions. Diffusion spectrum imaging (DSI) reconstructs a pdf $P(\mathbf{r})$ by transforming (via inverse Fourier transform) signals acquired at sampled **q** vectors ($\mathbf{q} = \gamma\delta\mathbf{g}$), where γ, δ and **g** are the gyro magnetic ratio, the diffusion gradient duration and the wave vector respectively (Tuch et al., 2002). The wave vector **q** needs to be sampled over the whole 3D space (Q-space), resulting in a long time and strong gradient fields for acquisition. Instead of reconstructing a 3D $P(\mathbf{r})$, Q-ball imaging only needs to use signals sampled at a sphere in the Q-space to estimate a 2D orientation distribution function (ODF) $\varphi(\mathbf{u})$, which is the integral of a $P(\mathbf{r})$ over the radial dimension *c* as follows (Tuch et al., 2003),

$$\varphi(\mathbf{u}) = \int_0^{+\infty} P(c\mathbf{u})dc, \quad (1.5)$$

where **u** is a unit vector representing a orientation. The ODF can be approximated by taking the Funk-Radon transform of MR signals sampled on the Q-ball. Similarly Anderson (2005) estimates a fiber orientation distribution (FOD) in a voxel using continuous axially symmetrical tensor. For regularization, ODF and FOD are usually represented as linear combinations of spherical harmonics.

2. White matter fiber tracking

The diffusion imaging data can't directly provide representations of brain white matter fibers. A fiber tracking algorithm is needed to further reconstruct neural fibers. To date, a plethora of fiber tracking algorithms have been proposed, which can be categorized into deterministic and probabilistic algorithms. For a given seed point, which is the starting point for a single run of fiber tracking, a deterministic algorithm yields an optimal fiber based on certain criterion such as following the principal diffusion directions. A probabilistic algorithm generally constructs a posterior probability distribution of fibers conditioned on imaging data and then samples fibers from that distribution.

A. Deterministic fiber tracking

The streamline method is the most straightforward and popular approach employed for fiber tracking (Basser et al., 2000; Mori et al., 2002; Jones et al., 1999; Conturo et al., 1999; Stieltjes et al., 2001). Starting from a seed point, the algorithm generates a fiber by sequentially following local principle diffusion directions (PDD). Basser et al. (2000) formulated this heuristic tracking process as solving the below differential equation,

$$\frac{d\mathbf{x}(s)}{ds} = \mathbf{t}(s), \tag{1.6}$$

where $\mathbf{x}(s)$ represents a 3D curve that is parameterized by s and $\mathbf{t}(s)$ is the tangent vector along $\mathbf{x}(s)$. With $\mathbf{t}(s)$ set to the PDD at point $\mathbf{x}(s)$, the streamline method is essentially solving Equation 1.6 using a finite difference scheme as follows,

$$\mathbf{x}(s_i) = \mathbf{x}(s_{i-1}) + \mathbf{v}_{i-1}\Delta s, \tag{1.7}$$

where $\mathbf{x}(s_i)$ denotes a discrete point on $\mathbf{x}(s)$, $\mathbf{v}_{i-1}$ is the PDD at $\mathbf{x}(s_{i-1})$ and Δs is the step size. Various streamline methods differ in numerical schemes used (first order Euler's method, second order Runge-Kutta's method), interpolation methods for the PDD (linear interpolation, closest point interpolation) at $\mathbf{x}(s_i)$, and factors terminating tracking (fractional anisotropy, fiber curvature).

The tensor line approach (Weinstein et al., 1999; Lazar et al., 2003) computes the fiber tangential direction $\mathbf{v}_i$ at $\mathbf{x}(s_i)$ by modulating $\mathbf{v}_{i-1}$ at $\mathbf{x}(s_{i-1})$ based on the local diffusion tensor $\mathbf{D}(\mathbf{x}(s_i))$ at $\mathbf{x}(s_i)$ as below,

$$\mathbf{v}_i = \mathbf{D}(\mathbf{x}(s_i))\mathbf{v}_{i-1}. \tag{1.8}$$

For an isotropic $\mathbf{D}(\mathbf{x}(s_i))$, $\mathbf{v}_i$ is not deviated much from $\mathbf{v}_{i-1}$. For a prolated $\mathbf{D}(\mathbf{x}(s_i))$, $\mathbf{v}_i$ is generated by deflecting $\mathbf{v}_{i-1}$ towards the PDD of $\mathbf{D}(\mathbf{x}(s_i))$. For an oblated $\mathbf{D}(\mathbf{x}(s_i))$, $\mathbf{v}_{i-1}$ is deflected towards the flat plane of $\mathbf{D}(\mathbf{x}(s_i))$ to yield $\mathbf{v}_i$, so $\mathbf{v}_i$ would be the same as $\mathbf{v}_{i-1}$ if $\mathbf{v}_{i-1}$ is already in the flat plane of $\mathbf{D}(\mathbf{x}(s_i))$. It has been shown that the tensor line approach is less sensitive to noises on PDDs than the streamline method.

In the above methods, noises and partial volume effect may result in erroneous estimates of $\mathbf{v}_i$ and such errors can be accumulated in a tracking process. To overcome such problems, Poupon et al. (2000) regularize PDD fields to reduce the curvature of resulting

fibers. Similarly Lu et al. (2006) proposed a Bayesian framework for tracking, which estimates $\mathbf{v}_i$ by maximizing a posterior probability.

Another type of methods estimates fiber pathways by simulating a diffusion process (Parker et al., 2002; Kang et al., 2005). These methods begin by setting an initial concentration of virtual water at seed points, and then use diffusion tensors to control the diffusion process of the initial water. After simulating the diffusion process for a period of time, the final distribution of the virtual water can be used to compute the connectivity between voxels. Paker et al. (2002) used a fast marching approach and set the front movement to be driven by underlying PDDs. Kang et al. (2005) employed a classic diffusion equation, whose diffusion tensor values are set to those obtained from DTI.

B. Probabilistic fiber tracking

Noise in diffusion imaging introduces uncertainty into a fiber tracking process by causing observed diffusion tensors and PDDs to deviate from their true values. Probabilistic tracking algorithms generate a set of fibers in stead of a single one, whose distributions can reflect the underlying uncertainty.

Bjornemo et al. (2002) proposed to adapt the streamline method to a probabilistic algorithm by adding a stochastic term in the right side of Equation 1.7, which incorporates uncertainty of PDDs into tracking. They also showed the relationship of such a method with a sequential importance sampling. Similarly Hagmann et al. (2003) generates $\mathbf{v}_{i-1}$ in Equation 1.7 stochastically using a random walk model.

Instead of heuristically making Equation 1.7 stochastic, Parker et al. (2003) built a posterior probability distribution of PDD conditioned on DTI data so that tangential

vectors can be sampled from the distribution during the fiber tracking process. Friman et al. (2006) modeled the posterior probability of fibers as follows,

$$p(\mathbf{v}_{1:n} \mid \mathbf{D}) = p(\mathbf{v}_1 \mid \mathbf{D}) \prod_{i=2}^{n} p(\mathbf{v}_i \mid \mathbf{v}_{i-1}, \mathbf{D}), \tag{1.9}$$

where *p(A|B)* is the conditional probability of *A* given *B* and the sequence of $\mathbf{v}_{1:n}$ is assumed to satisfy the Markov condition. With Equation 1.9, WM fibers can be sampled by sequentially drawing a random vector $\mathbf{v}_i$ from a distribution $p(\mathbf{v}_i \mid \mathbf{v}_{i-1}, \mathbf{D})$. Using a Bayesian rule, $p(\mathbf{v}_i \mid \mathbf{v}_{i-1}, \mathbf{D})$ can be expressed as,

$$p(\mathbf{v}_i \mid \mathbf{v}_{i-1}, \mathbf{D}) = \frac{p(\mathbf{D} \mid \mathbf{v}_i) p(\mathbf{v}_i \mid \mathbf{v}_{i-1})}{p(\mathbf{D})}, \tag{1.10}$$

where $p(\mathbf{D} \mid \mathbf{v}_i)$ describes the probability of observing diffusion data **D** given a underlying fiber orientation $\mathbf{v}_i$ and $p(\mathbf{v}_i \mid \mathbf{v}_{i-1})$ models prior knowledge about two consecutive vectors $\mathbf{v}_i$ and $\mathbf{v}_{i-1}$. Zhang et al. (2007) used a particle filter sampling framework and a Von Mises-Fisher distribution for modeling $p(\mathbf{D} \mid \mathbf{v}_i)$ and $p(\mathbf{v}_i \mid \mathbf{v}_{i-1})$. The resampling process in a particle filter eliminates fibers with low posterior probability so that sampled fibers are more concentrated around the optimal fiber. In addition, Zhang et al.'s efficient sampling of a Von Mises-Fisher distribution increases the speed of fiber tracking.

3. Fiber bundle segmentation

Fibers with similar shapes and locations are often grouped into a fiber bundle for better quantitative characterization of neuronal pathways. Furthermore, it's useful for these bundles to be associated with anatomical structures in the human brain.

A. Manual segmentation

Manual methods require users to manually place several regions of interest (ROI) in the fiber space and then fibers are grouped into bundles based on a certain combination of predefined ROIs (Stieltjes et al., 2001; Wakana et al., 2004; Catani et al. 2002). The positions of such ROIs are usually determined by reviewing fractional anisotropy images and by referring to prior anatomical knowledge. Manual segmentation approaches are flexible in defining and selecting bundles of interest and they provide bundles consistent with brain anatomy, so they have gained great popularity in clinical studies (Ciccarelli et al., 2003; Kanaan et al., 2006). However, these methods suffer from inter- and intra-operator variabilities and are highly inefficient due to the manual placement of ROIs.

B. Clustering based segmentation

Fiber bundling can be automated by computer based clustering methods, which group similar fibers with minimal human interventions. To date a few algorithms of this kind have been proposed. They differ in definitions of fiber similarity and clustering approaches used (Ding et al., 2003; O'Donnell et al. 2005, 2006b; Maddah et al., 2006, 2007a, 2007b, 2008; Zhang et al., 2002, 2005, 2006, 2008; Moberts et al., 2005; Corouge et al., 2004; Brun et al., 2003, 2004; Shimony et al., 2002). Ding et al. (2003) defined the fiber similarity as the mean Euclidean distance between corresponding segments of a pair of fibers, where the correspondence is established by aligning fibers with their seed points. Starting with each single fiber as a cluster, the algorithm keeps merging neighbor clusters until their minimal distances become too large. Corouge and Gerig (2004) constructed point correspondence for two fibers by mapping each point in one fiber to their closest point in the other. They proposed three distance measures, which are

respectively the minimum, mean and maximum of the Euclidean distances between corresponding points. Brun et al. (2003) represented each fiber as a three-dimensional feature vector using a Lapacian eigenmap, and fibers with similar low-dimensional features are grouped into a bundle. In their later work (Brun et al., 2004), a fiber is represented by a nine-dimensional vector that includes the first and second order statistics of points in that fiber (centroids and covariance matrices). The Euclidean distance between fiber features are computed pairwise to create a weighted undirected graph, which is further partitioned into coherent sets with a normalized cut algorithm. Maddah et al. (2006) constructed statistical bundle models for coefficients of B-spline representation of fibers. By assuming a mixture bundle model, an expectation maximization (EM) algorithm is employed to estimate model parameters and label fibers. A gamma mixture distribution is later used in this framework to more faithfully model fiber distributions in bundles (Maddah et al., 2007a, 2007b, 2008). Zhang et al. (2002) defined the fiber distance as the mean of distances between points in the shorter fiber and their closet correspondences in the other. An agglomerative clustering algorithm is used to cluster fibers by initially treating each fiber as an individual bundle and then merging closest bundles until convergence. This framework was expanded in their later work (Zhang et al., 2005, 2006, 2008). Shimony et al. (2002) used a fuzzy clustering algorithm in their automated fiber bundling. O'Donnell et al. (2005, 2006b) selected the maximum of pointwise minimum distances between a pair of fibers as the fiber distance measure and then used a k-way normalized cut algorithm to cluster all fibers from different subjects.

The clustering-based methods are efficient, but lack flexibility in generating bundles that satisfy the need of specific studies. Moreover, most of these methods do not assign anatomical labels to bundles, which limits their direct use in clinical studies.

C. Atlas based segmentation

Atlas based methods align an input set of fibers to a pre-defined atlas with known anatomical label so that fibers can be automatically labeled by referring to the atlas (Zhang et al., 2007; Maddah et al., 2005; O'Donnell et al. 2006a, 2007; Xia et al., 2005). Xia et al. constructed an atlas with labeled grey matter, and fibers' bundle memberships are then determined by anatomical labels of their ending points. Fiber atlases/templates are more frequently used for the purpose of segmenting fiber bundles (Zhang et al., 2007; Maddah et al., 2005; O'Donnell et al. 2006a). They are typically constructed by transforming fibers from different patients into a common space and then manually labeling either raw fibers or bundles generated from a clustering algorithm. Once a fiber atlas is established, input fibers need to be transformed into the atlas space and compared with atlas fibers to determine which bundle they belong to. Atlas based methods not only group fibers into bundles but also assign them to anatomical structures in brain. The bundling performance relies on how accurately fibers from different subjects are registered with atlas.

4. DTI image and fiber registration

DTI images or fibers from different subjects are often needed to be registered into a common space for comparison. Registration techniques that have already been employed in DTI area fall into two categories, image-based and feature-based registration. Image-based methods find a transformation that maps a target image to a reference so that their

overall image differences are minimized (Alexander et al., 1999a, 1999b, 2001; Jones et al., 2002; Leemans et al., 2005; Ruiz-Alzola et al., 2000, 2002; Guimond et al., 2002; Park et al., 2003; Zhang et al., 2005, 2006; Van Hecke et al., 2007; Chiang et al., 2008). Alternatively, feature-based approaches rely on features extracted from two DTI images such as WM fibers (Leemans et al., 2006; Mayer et al., 2007; Ziyan et al., 2007).

A. Image-based registration

Registration of DTI images is more challenging than registration of grey-level images, since each voxel in DTI contains multi-channel DWI signal, a diffusion tensor or a orientation distribution (HARDI). One straightforward approach is to directly apply a scalar image registration algorithm to some scalar measures associated with DTI images, such as T2-weighted MR intensities and fractional anisotropy (FA) maps (Jones et al., 2002). Although this kind of approach is easy to use and widely adopted in clinical studies (Wakana et al., 2004), it only utilizes a subset of information from DTI data, which often results in inaccurate results. To consider more information from DTI data, Alexander et al. (1999a) heuristically designed a tensor similarity measure and embedded the metric in a multi-resolution elastic matching algorithm. They also raised the issue of tensor reorientation that tensors in warped DTI must be locally reoriented to keep consistent with its surrounding anatomical features. One reasonable reorientation scheme is to decompose a transformation to a rigid rotation and a deformation component, and only use the rotation component to reorient tensors (Alexander et al., 1999b, 2001). To take the deformation component into account, another scheme was also proposed based on preservation of the PDD (Alexander et al., 1999b, 2001). Ruiz-Alzola et al. (2000, 2002) used the correlation between two diffusion tensors as a similarity measure to

register 3D tensor data. Based on the correlation metric, image windows containing salient features are matched in a multi-resolution way, and resulting deformation fields were interpolated using a Kriging estimator. Guimond et al. (2004) used a multi-channel Demons registration algorithm for diffusion tensors represented as a six-component multi-channel data. Park et al. (2003) relied on the same registration framework but used different combinations of channel data such as T2-weighted intensity, FA, the difference between the first and second eigenvalues, etc. In both of their work, the tensor reorientation is performed in each iteration of registration algorithm. Zhang et al. (2005, 2006) incorporated the tensor reorientation factor into the registration objective function so that it can be optimized without a need to explicitly reorient tensors. They employed a L^2 tensor distance and estimated a piecewise affine transformation. Recently Van Hecke et al. (2007) proposed several definitions for the mutual information between two multi-channel DTI images and maximized their mutual information using a viscous fluid model. Chaing et al. (2008) defined the KL-divergence between two tensors or orientation distributions as the dissimilarity measure and also used a viscous fluid model for optimization.

B. Feature-based registration

While being able to provide more accurate results in principle, diffusion tensor based registration technique has not gained anticipated popularity in the DTI community, likely owing to the complications in tensor reorientation, interpolation and selection of appropriate tensor metrics. More recently there have been some endeavors in developing techniques for direct registration of WM fibers. For example, Leemans et al. (2006) and Mayer et al. (2007) each proposed an iterative scheme for estimating a rigid or affine

transformation based on the alignment of individual fibers in reference data to their closest counterparts in target data. Leeman et al. used the torsion and curvature of fibers to determine the closest target fiber; Mayer et al. downsampled each fiber to a fixed number of points and represented fibers as vectors composed of a concatenation of sampled points. Both two methods are computationally intensive due to the process of closest-fiber finding and one-to-one fiber registration given the sheer number of fibers per volume that are typically generated by tractography. In addition, the rigid and the affine transformation have limited freedoms for deformation, which restricts the accuracy of fiber alignment. In contrast to the fiber-to-fiber registration, Ziyan et al. (2007) proposed a method that aligns corresponding fiber bundles individually with an affine transformation, which is subsequently combined across bundles using a poly-affine framework. Although the computational efficiency has been improved due to the bundle-to-bundle registration, this method requires pre-clustering of fiber bundles as well as a reasonable initial affine registration.

5. Contributions

The overall contribution of this work is to solve the problem of DTI fiber bundling and alignment.

To be more specific, the first contribution is to investigate statistical models of fiber bundle, in terms of (1) how accurately the studied models fit a bundle of white matter fibers and (2) how efficiently the model parameters are estimated and an arbitrary fiber is inferred with the models. Usually a balance needs to be made between the accuracy and the efficiency of fiber bundle models. This work provides a necessary guidance to

choosing appropriate statistical models for further characterization and group comparisons of white matter bundles.

The second contribution is to design and implement a unified fiber bundling and registration (UFIBRE) algorithm that combines fiber clustering and bundle registration. This method automatically clusters the major white matter tracts into anatomical neural pathways by aligning them to a manually pre-built template bundle set. Thus the comparison of a specific white matter bundle can be made easily between two subjects. A bundle atlas for anatomical pathways can also be built by aligning all the subjects into a common template.

The UFIBRE algorithm can successfully bundle major white matter tracts, whose template can be reliably segmented by manually placing ROIs in white matter. However, it can't be applied to some bundles whose definition ROIs are not well defined or cannot be reliably segmented, e.g., bundles connecting a pair of cortical/sub-cortical units. The third contribution of this dissertation is to propose a novel clustering algorithm that leverages an inaccurate segmentation of brain cortex to cluster fibers into bundles connecting different pairs of cortical/sub-cortical ROIs.

The last but not least contribution of this work is to propose a group-wise whole brain bundling algorithm in order to achieve a more consistent and reliable bundling. This algorithm performs simultaneous group bundle estimation and registration from subjects' native spaces to a group common space.

CHAPTER II

STATISTICAL FIBER BUNDLE MODEL

Prior to fiber clustering and further bundle analysis, a suitable model needs to be firstly chosen to represent the spatial or statistical distribution of fibers in a bundle. In this chapter, we investigate two statistical models for fiber bundle and evaluate their performances in terms of both accuracy and efficiency.

1. Vector representation for fiber

Fiber tracking algorithms usually generate fibers that are composed of sequences of consecutive three dimensional points. Let $\mathbf{x}$ denote a single fiber that contains n consecutive points $\mathbf{x}_1$, $\mathbf{x}_2$, … , $\mathbf{x}_n$. Each $\mathbf{x}_i$ represents a three dimensional vector, where $\mathbf{x}_{i,x}$, $\mathbf{x}_{i,y}$ and $\mathbf{x}_{i,z}$ denote the three coordinates in the x, y, and z axis respectively. To model a bundle of fibers, each fiber needs to be represented as a vector in a high dimensional space. A straightforward approach is to directly concatenate all the coordinates in a fiber so that fiber $\mathbf{x}$ would become a vector whose size is 3n. However, as fibers in a bundle less likely have the same number of points, this simple approach would make fibers represented in different Euclidean spaces.

A. Uniform resampling

One approach to addressing the above issue is to resample each fiber inside a bundle into the same number of points. Let $\lfloor\ \rfloor$ and $\lceil\ \rceil$ denote the floor and the ceiling function that

maps a real number to its largest previous and smallest following integer respectively. To resample a fiber of length n into a fiber of length m, original points $\mathbf{x}_1$, $\mathbf{x}_2$, … , $\mathbf{x}_n$ are used to compute a new set of points $\bar{\mathbf{x}}_1$, $\bar{\mathbf{x}}_2$, … , $\bar{\mathbf{x}}_m$. Let j index points on the resampled curve. The jth point $\bar{\mathbf{x}}_j$ can be written as a linear combination of $\mathbf{x}_{\lfloor nj/m \rfloor}$ and $\mathbf{x}_{\lceil nj/m \rceil}$ as follows,

$$\begin{aligned}
\bar{\mathbf{x}}_{j,x} &= \mathbf{x}_{\lfloor nj/m \rfloor,x}(\lceil nj/m \rceil - nj/m) + \mathbf{x}_{\lceil nj/m \rceil,x}(nj/m - \lfloor nj/m \rfloor) \\
\bar{\mathbf{x}}_{j,y} &= \mathbf{x}_{\lfloor nj/m \rfloor,y}(\lceil nj/m \rceil - nj/m) + \mathbf{x}_{\lceil nj/m \rceil,y}(nj/m - \lfloor nj/m \rfloor). \\
\bar{\mathbf{x}}_{j,z} &= \mathbf{x}_{\lfloor nj/m \rfloor,z}(\lceil nj/m \rceil - nj/m) + \mathbf{x}_{\lceil nj/m \rceil,z}(nj/m - \lfloor nj/m \rfloor)
\end{aligned} \tag{2.1}$$

Such a resampling is demonstrated for the fiber bundle that connects the left and the right superior frontal gyrus in Figure 2.1, where red crosses represent points making the fibers. Each fiber in the left bundle originally contains ~70 points, and then these fibers are resampled into 30 points.

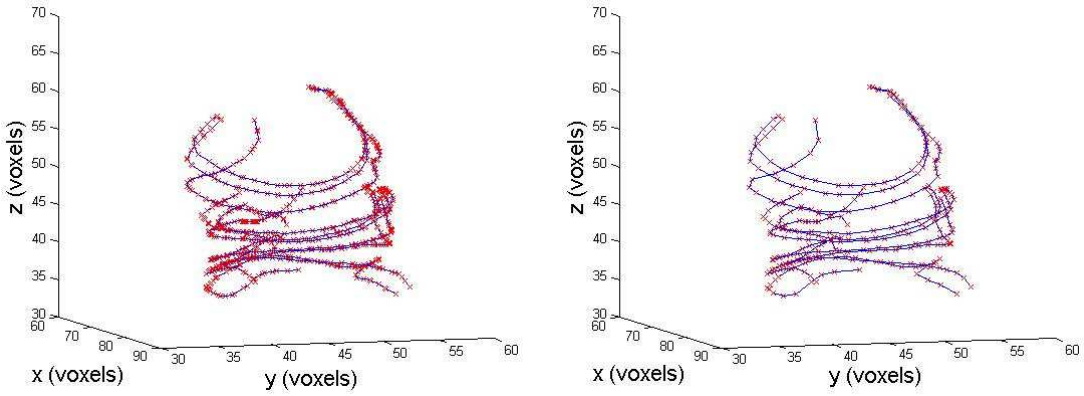

(a) (b)

Figure 2.1 A demonstration of uniform resampling for the bundle connecting the left and the right superior frontal gyrus. The left figure (a) shows the original curves and each curve is resampled into 30 points in the right figure (b).

Using such a resampling, each fiber can be represented by the same number of points and the concatenation of these points makes a high dimensional vector as below,

$$\mathbf{x} = \begin{bmatrix} \bar{\mathbf{x}}_{1,x} \\ \bar{\mathbf{x}}_{1,y} \\ \bar{\mathbf{x}}_{1,z} \\ \cdot \\ \cdot \\ \bar{\mathbf{x}}_{m,x} \\ \bar{\mathbf{x}}_{m,y} \\ \bar{\mathbf{x}}_{m,z} \end{bmatrix}. \tag{2.2}$$

Once this vector representation is built, point correspondence between all fibers is naturally constructed. In other words, for two arbitrary fiber $\mathbf{x}$ and $\mathbf{y}$, resampled point $\bar{\mathbf{x}}_j$ is assumed to be the corresponding point of $\bar{\mathbf{y}}_j$ in curve $\mathbf{x}$, as $\bar{\mathbf{x}}_j$ and $\bar{\mathbf{y}}_j$ are the coordinates of the same dimension in the fiber vector space. The uniform resampling essentially assumes that all fibers in a bundle have the same length. However, there are rarely fibers with the same exact length, and such an assumption would cause incorrect point mapping between two fibers. Figure 2.2 illustrates this problem by using two simulated fibers, a long and a short one. It can be seen that the short fiber should match the lower portion of the long fiber (see Figure 2.2 (a)), but uniform resampling would make it match the whole long fiber (see Figure 2.2 (b)).

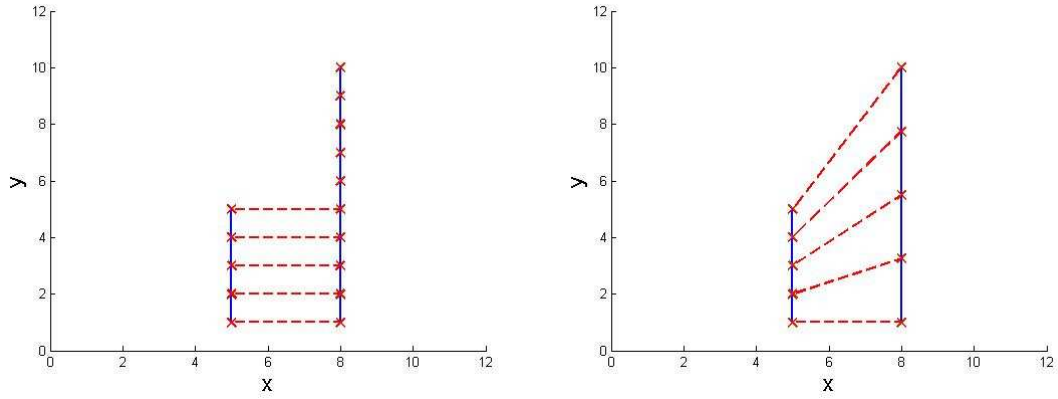

(a) (b)

Figure 2.2 A demonstration of incorrect point correspondence caused by uniform sampling. The left figure (a) displays two fibers and their true point correspondence (red dot curve). The right figure (b) shows the point correspondence after a 5 point uniform resampling.

B. Closest point resampling

An alternative approach is to map each point in a fiber to its closest correspondence in a reference fiber. Using the short fiber as a reference, the lower portion of the long fiber would be mapped to the short fiber in Figure 2.2. Prior to resampling, a reference fiber needs to be firstly selected in a bundle of fibers. Here we propose to use the median fiber as the reference. Let $\mathbf{x}_j$ (j = 1,2, …, M) denote the jth fiber in a bundle, and $\mathbf{x}_{j,i}$ represent the ith point in the jth fiber. The median fiber $\mathbf{x}_{median}$ is the fiber that has the minimum distance to the rest of fibers in the bundle,

$$\mathbf{x}_{median} = \arg\max_{x_{median}} \sum_{j=1}^{M} d(\mathbf{x}_j, \mathbf{x}_{median}), \tag{2.3}$$

where d denotes a metric that measures the distance between two fibers. Let $\mathbf{x}_i$ and $\mathbf{x}_j$ be two arbitrary fibers containing n and m points respectively. Their distance can be computed as follows,

$$d(\mathbf{x}_i, \mathbf{x}_j) = \sum_{k=1}^{n} \| \mathbf{x}_{i,k} - \mathbf{x}_{j,\varphi_{x_i,x_j}(k)} \| + \sum_{k=1}^{m} \| \mathbf{x}_{j,k} - \mathbf{x}_{i,\varphi_{x_j,x_i}(k)} \|,$$

where $\| \bullet \|$ denotes the Euclidean distance between two points and $\varphi_{x_i,x_j}(\bullet) / \varphi_{x_j,x_i}(\bullet)$ is a function that maps the k point in fiber $\mathbf{x}_i / \mathbf{x}_j$ to its closest corresponding point on fiber $\mathbf{x}_j / \mathbf{x}_i$. This metric is symmetric, i.e., $d(\mathbf{x}_i, \mathbf{x}_j) = d(\mathbf{x}_j, \mathbf{x}_i)$.

Given the mapping function φ and the median fiber $\mathbf{x}_{median}$, a fiber $\mathbf{x}_i$ can be resampled as follows,

$$\overline{\mathbf{x}_i} = \begin{bmatrix} \mathbf{x}_{i,\varphi_{x_{median},x_i}(1),x} \\ \mathbf{x}_{i,\varphi_{x_{median},x_i}(1),y} \\ . \\ . \\ . \\ \mathbf{x}_{i,\varphi_{x_{median},x_i}(n),x} \\ \mathbf{x}_{i,\varphi_{x_{median},x_i}(n),y} \\ \mathbf{x}_{i,\varphi_{x_{median},x_i}(n),z} \end{bmatrix}, \qquad (2.4)$$

where $\mathbf{x}_{median}$ has n points.

The fibers in Figure 2.1 are resampled with the closest point approach, which are illustrated in Figure 2.3.

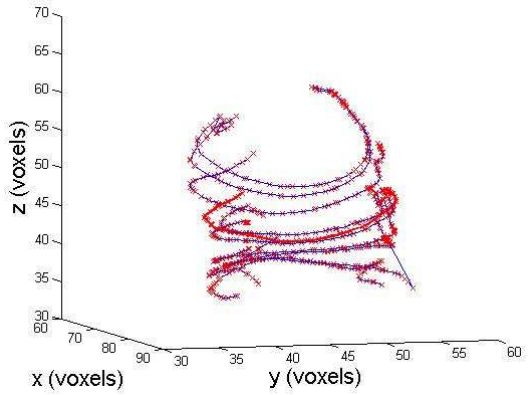

Figure 2.3 A demonstration of closest point resampling for the bundle connecting the left and the right superior frontal gyrus.

Although closest point based correspondence is more accurate, it has problems in some instances. Figure 2.4 demonstrates one of such scenarios: when a fiber is too far away from the reference, all of its points may be mapped to a single reference point, which is shown in Figure 2.4 (a). In this case, uniform resampling provides more reasonable results (Figure in 2.4 (b)). Therefore, we conclude that uniform resampling yields more reliable and robust results in the case where some fibers in a bundle deviate too much in shapes or spatial locations from other fibers; closest point resampling provides more accurate sampling in the case where all fibers in a bundle are coherent.

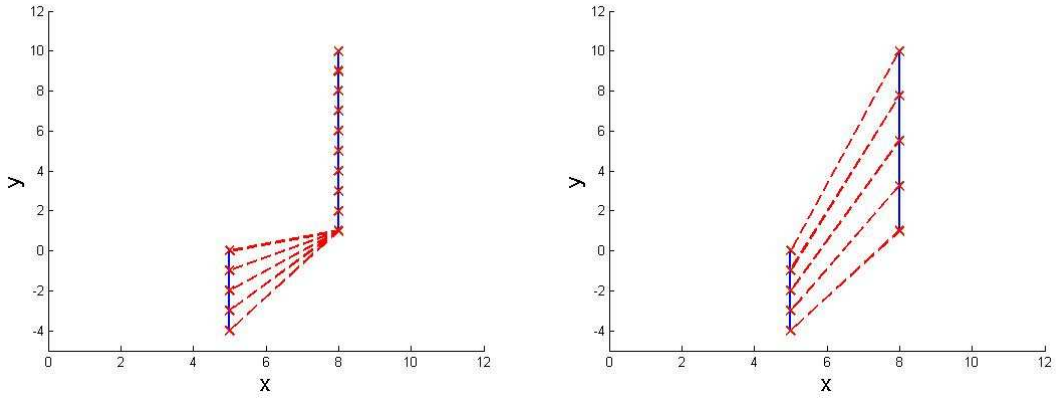

(a) (b)

Figure 2.4 A comparison of the closest point (a) and the uniform resampling (b) for two fibers far away from each other.

2. Statistical models for fiber bundle

A resampling procedure (either uniform or closest point) maps an arbitrary fiber into a high dimensional vector space, where linear algebra for fibers is made possible. In this section, $\mathbf{x}_j$ (j = 1, 2,…, M) denotes vector representations of the jth fiber in a bundle $\mathbf{x}$, and $\mathbf{x}_{j,i}$ represent the ith coordinate in the vector. A statistical bundle model would be central to fiber clustering and bundle alignment, and thus it needs to be carefully studied.

A. Gaussian model

Thanks to the vector representation, the Gaussian model for a fiber bundle can be expressed as follows,

$$p(\mathbf{y} \mid \boldsymbol{\mu}, \boldsymbol{\sigma}) = (\frac{1}{2\pi})^{3m/2} \mid \boldsymbol{\sigma} \mid^{-1/2} \exp(-\frac{1}{2}(\mathbf{y}-\boldsymbol{\mu})^T \boldsymbol{\sigma}^{-1}(\mathbf{y}-\boldsymbol{\mu})),$$

where $\mathbf{y}$ denotes a fiber in the bundle and $\boldsymbol{\mu}, \boldsymbol{\sigma}$ are the mean and the covariance matrix respectively. All fibers are resampled into m points, which makes $\boldsymbol{\mu}$ a 3m long vector representing the medial axis or centroid in this bundle. $|\bullet|$ computes the determinant of a matrix and a^T represents a transpose of vector or matrix a. As the covariance matrix is symmetric, there are totally 3m(3m+1)/2 parameters that need to be estimated. However, a fiber bundle usually doesn't contain sufficient fibers, so this estimation is at least unreliable if not impossible. To simplify the Gaussian bundle model, it is further assumed

that each point in a fiber is independent to others in the same fiber. Therefore, the above Gaussian formula can be simplified as,

$$p(\mathbf{y} \mid \boldsymbol{\mu}, \boldsymbol{\sigma}) = \prod_{i=1}^{m} (\frac{1}{2\pi})^{3/2} \mid \boldsymbol{\sigma}_i \mid^{-1/2} \exp(-\frac{1}{2}(\mathbf{y}_i - \boldsymbol{\mu}_i)^T \boldsymbol{\sigma}_i^{-1} (\mathbf{y}_i - \boldsymbol{\mu}_i)), \qquad (2.5)$$

where $\mathbf{y}_i$ is the ith point in $\mathbf{y}$ and $\boldsymbol{\mu}_i, \boldsymbol{\sigma}_i$ are the mean position and the covariance matrix for all the ith points in this bundle. Given such a Gaussian model and a resampling scheme, fiber $\mathbf{y}$ can be inferred by Equation 2.5.

Given a bundle of fibers $\mathbf{x}_j$ (j = 1,2, …, M), the above Gaussian parameters can be estimated using the below formula,

$$\begin{aligned} \boldsymbol{\mu}_i &= \frac{1}{M} \sum_{i=1}^{M} \mathbf{x}_{j,i} \\ \boldsymbol{\sigma}_i &= \frac{1}{M} \sum_{j=1}^{M} (\mathbf{x}_{j,i} - \boldsymbol{\mu}_i)(\mathbf{x}_{j,i} - \boldsymbol{\mu}_i)^T \end{aligned} . \qquad (2.6)$$

Figure 2.5 shows an example of such a Gaussian bundle model. The fibers under study connect the left and the right superior occipital gyrus (see Figure 2.5 (a)). Figure 2.5 (b) shows the medial axis $\boldsymbol{\mu}$. Figure 2.5 (c) displays the three by three covariance matrices, which are plotted with ellipsoids. It can be seen that the sizes of ellipsoids are roughly consistent with the width of the bundle cross section.

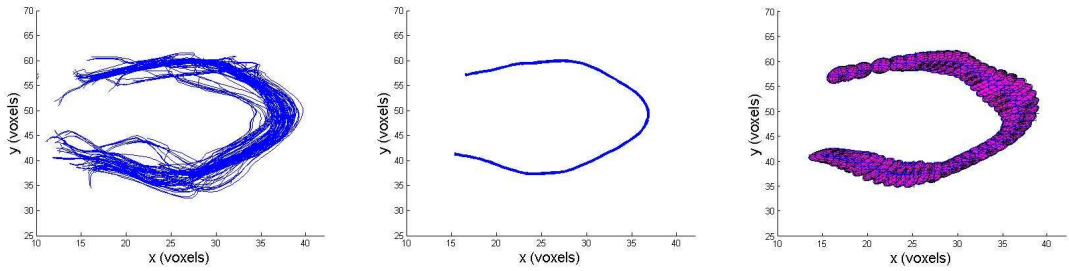

(a) (b) (c)

Figure 2.5 A demonstration of the Gaussian model for the bundle connecting the left and the right superior occipital gyrus. (a) Original fibers. (b) the centroid or medial axis. (c) the covariance matrices.

B. Gamma model

In a Gaussian distribution of fibers, the medial axis has the maximum likelihood and other fibers have smaller likelihoods, which decay exponentially with their distance to the centroid. However, this Gaussian assumption contradicts the fact of a fiber bundle being a generalized cylinder-shaped object. For a generalized cylinder, there is only a single fiber in the medial axis position and much more fibers having certain distances to the centroid. In contrast with the Gaussian assumption, the number of fibers even increases with the increase of distance as long as the distance doesn't exceed the radius of cylinder cross section. When the distance is greater than the cylinder radius, fiber's probability of being in the bundle become exponentially decaying again.

Based on the above observation, Maddah proposed a Gamma distribution, which is also a two-parameter continuous distribution, to model the distances of fibers to the centroid as follows,

$$p(\mathbf{y} \mid k, \theta) = d_{y,\mu}{}^{k-1} \frac{\exp(-d_{y,\mu} / \theta)}{\theta^k (k-1)!}, \tag{2.7}$$

where $d_{y,\mu}$ is the distance between fiber $\mathbf{y}$ and the centroid $\boldsymbol{\mu}$; k controls the shape of the Gamma distribution; θ is the scale parameter (the larger θ, the more spread out the

distribution). Both k and θ are positive values. It can be seen from Equation 2.7 that the left polynomial term increases with $d_{y,\mu}$ given that k is greater than one, while the right exponential term decays with $d_{y,\mu}$. Once $d_{y,\mu}$ exceeds a certain threshold, the exponential term dominates the probability function and the distribution becomes similar to the Gaussian distribution. Prior to the decay, the polynomial term dominates the probability, which make it increase with $d_{y,\mu}$. Figure 2.6 illustrates such a trend for a set of different k, θ.

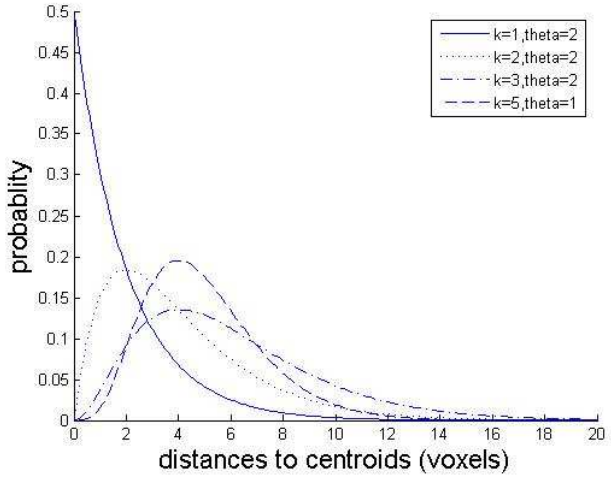

Figure 2.6 Gamma distributions with different parameters.

Given such a Gamma distribution (k, θ) and the fiber centroid, fiber $\mathbf{y}$ can be inferred by Equation 2.7.

Given a resampling scheme and a bundle of fibers $\mathbf{x}_j$ (j = 1,2, …, M), the above Gamma parameters can be computed by maximizing the log likelihood. There is no closed-form solution for k, nonlinear optimization is required to solve the optimal k accurately. Here

an approximation is used to solve k and the corresponding θ that makes the derivative of log likelihood zero,

$$\begin{aligned} k &\approx \frac{3 - s + \sqrt{(s-3)^2 + 24\,s}}{12\,s} \\ \theta &= \frac{1}{kM}\sum_{j=1}^{M} d_{y_j,\mu} \end{aligned}, \tag{2.8}$$

where

$$s = \ln\left(\frac{1}{M}\sum_{j=1}^{M} d_{y_j,\mu}\right) + \frac{1}{M}\sum_{j=1}^{M}\ln\left(d_{y_j,\mu}\right). \tag{2.9}$$

3. Evaluations

To evaluate performances of the Gaussian and the Gamma models, one human brain DTI data were acquired using a 3T Philips Intera Achieva MR scanner (Best, The Netherlands) with an eight-element SENSE coil. A volume of 256×256×120 mm^3 was scanned using 32 non-collinear weighting directions and a single shot, echo-planar, pulsed gradient spin echo imaging sequence with a diffusion weighting factor (i.e., b value) of 1000 s/mm^2. The data matrix has a size of 128×128×60, given an isotropic resolution of 2×2×2 mm^3 in the data.

To generate fibers, a streamline tracking algorithm (Mori et al., 2002) was applied to the reconstructed tensor data. All the voxels with FA above 0.15 were selected as seed points, from which fibers were reconstructed by sequentially following the local principal diffusion directions (PDDs) at a step size of 2mm. The fiber tracking process was terminated when voxels with FA below 0.15 were met or the angle between the PDDs of

two consecutive points exceeded 41°. The above procedure yielded around 20,000 fibers for this single DTI dataset.

The fibers are then spatially transformed into the Montreal Neurological Institute (MNI) space by registering the associated T2 weighted images to a T2 MNI template in SPM 5 package. In the MNI space, the cortical and sub-cortical units have already been manually labeled (Tzourio-Mazoyer et al., 2002), which allows fibers to be grouped into bundles connecting two specific cortical or sub-cortical units. In this work, bundles with good coherence are studied, including:

Bundle 1 that connects the left precentral gyrus to the left inferior parietal, but supramarginal and angular gyri,

Bundle 2 that connects the right precentral gyrus to the right inferior parietal, but supramarginal and angular gyri,

Bundle 3 that connects the left to the right superior frontal gyrus,

Bundle 4 that connects the left to the right superior occipital gyrus,

Bundle 5 that connects the left middle occipital gyrus to the left inferior temporal gyrus,

Bundle 6 that connects the right middle occipital gyrus to the right inferior temporal gyrus,

Bundle 7 that connects the left postcentral gyrus to the left putamen,

Bundle 8 that connects the right postcentral gyrus to the right putamen,

Bundle 9 that connects the left angular gyrus to the left middle temporal gyrus,

Bundle 10 that connects the right angular gyrus to the right middle temporal gyrus,

Bundle 11 that connects the left to the right paracentral lobule.

To model these coherent bundles, fibers are firstly vectorized using the closest point approach (Equation 2.3 and 2.4). Then both the Gaussian and the Gamma model are computed based on the maximum likelihood estimator (Equation 2.6 and 2.8). The accuracy of resulting models are evaluated for each type of bundle based on the average log likelihoods of fiber data on estimated models as follows,

$$A1 = \frac{1}{M}\sum_{j=1}^{M}\log(p(\mathbf{x}_j \mid \boldsymbol{\mu},\boldsymbol{\sigma}))$$
$$A2 = \frac{1}{M}\sum_{j=1}^{M}\log(p(\mathbf{x}_j \mid k,\theta))$$

Figure 2.7 shows that the average log likelihoods of the Gamma model are significantly larger than those of the Gaussian for all types of bundles. This observation suggests that the Gamma distribution has better fitting to the data of fiber bundles, which can be translated as better accuracy.

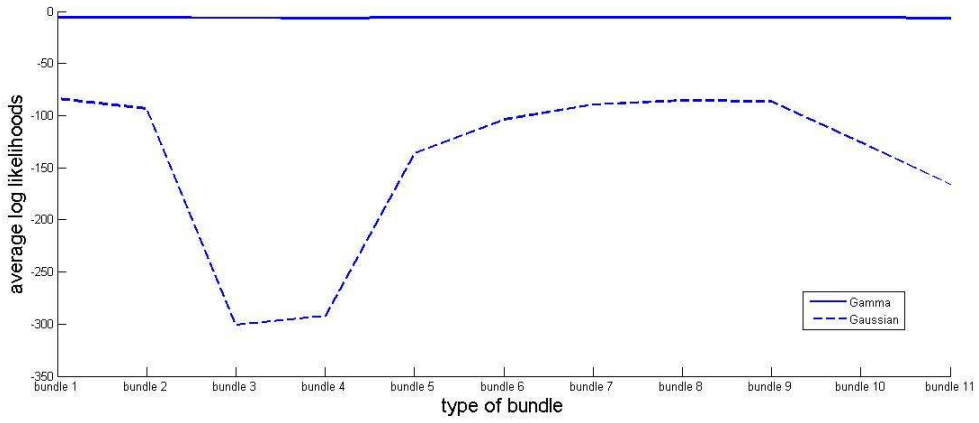

Figure 2.7 The curve of average log likelihoods with respect to type of bundles.

Histograms of distances between fibers and their centroids are plotted for two arbitrary bundles from the studied bundle set. Figure 2.8 shows that the shapes of histograms resemble those of the Gamma distribution, i.e., fibers that are 15-20 voxels distant from centroids outnumbers fibers in other distances, including those very close to the centroids. This can justify the use of the Gamma distribution and explain its better fitting to a bundle of fibers.

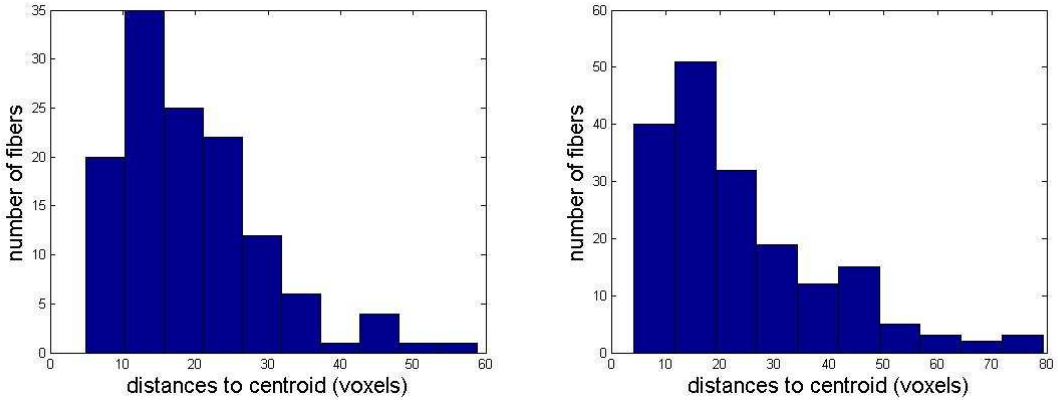

(a) (b)

Figure 2.8 Histograms of distances between fibers and their centroids for two fiber bundles.

4. Conclusions

This chapter discusses some preliminary issues for fiber clustering and registration, including fiber vectorization and bundle modeling.

Firstly, two fiber vectorization approaches are studied, showing that the closest point resampling is capable of providing more accurate fiber vectors while the uniform resampling scheme is more reliable, in particular, in the case where some fibers in a bundle are far apart from other fibers. Therefore, to maximize the advantages of these two resampling techniques, uniform resampling is recommended in the initial iterations of fiber clustering or alignment, as initially fibers from different bundles may be incorrectly included into a same bundle and thus they could be significantly different; On the other hand, in the final iteraions of algorithm, closest point sampling become a more suitable choice as most of fiber assignment is correct and thus bundles have much better coherence.

Statistical models are also studied for fiber bundles, suggesting that the Gamma distribution more accurately models fibers in a cylinder-shape bundle. However, the Gaussian model has some advantages over the Gamma: (1) The maximum likelihood estimation of its parameters has a simple and closed-form solution, which will simplify the optimization in any algorithm that involves bundle model; (2) the Gaussian bundle model is sufficiently accurate for the purpose of fiber clustering and bundle alignment. Therefore, to fully utilize the efficiency of the Gaussian model and the accuracy of the

Gamma model, we suggest performing fiber bundling and registration using the Gaussian model and modeling the resulting bundles with the Gamma so that the estimation of the Gamma model is just one-time computation.

CHAPTER III

UNIFIED FIBER BUNDLING AND REGISTRATION: THOERY AND METHODS

Fiber clustering and bundle alignment are two most fundamental requirements prior to any white matter analysis tasks. As a single fiber usually is not reliable due to imaging noises or fiber tracking errors, it is often desirable to study fibers in a unit of bundles. This kind of bundles can be generated solely by data driven clustering procedure, e.g., grouping fibers with similar shapes and locations into a bundle. Much often these bundles also should be corresponding to human brain anatomy, e.g., certain anatomic neuronal pathway or connections between two critical or sub-cortical areas. Bundle alignment is also necessary, as to compare white tracts from different subjects to detect their difference bundle must be aligned in a common space or at least have certain correspondences.

To address these needs simultaneously, a unified fiber bundling and registration (UFIBRE) framework is proposed in this work (Xu et al., 2009). The framework is based on maximizing *a posteriori* Bayesian probabilities using an expectation maximization algorithm. Given a set of segmented template bundles and a whole-brain target fiber set, the UFIBRE algorithm optimally bundles the target fibers and registers them with the template. The bundling component in the UFIBRE algorithm simplifies fiber-to-fiber registration into bundle-to-bundle registration, and the registration component in turn

guides the bundling process to find bundles consistent with the template.

1. Introduction

The existing fiber bundling methods are performed either by manually placing regions of interest (ROIs) that groups the fibers that pass through the same set of ROIs as a distinct bundle (Stieltjes et al., 2001; Wakana et al., 2004; Catani et al. 2002) , or by using computer based clustering methods that group similar fibers with minimal human intervention (Ding et al., 2003; O'Donnell et al. 2005, 2006b; Maddah et al., 2006, 2007a, 2007b, 2008; Zhang et al., 2002, 2005, 2006, 2008; Moberts et al., 2005; Corouge et al., 2004; Brun et al., 2003, 2004; Shimony et al., 2002). However, both types of these methods do have their own disadvantages: (1) manual labeling methods are tedious and suffer from inter- and intra-operator variability; (2) clustering based methods lack the flexibility in generating bundles and hardly provide bundles that have clear anatomic correspondence.

In addition to the above issues, DTI image co-registration also has its unique challenges (Jones et al., 2002; Wakana et al., 2004; Alexander et al., 1999b, 2001; Van Hecke et al., 2007): (1) Co-registration of a scalar map of DTI less likely aligns fibers as orientation information is usually not included; (2) consideration of the full tensor information also faces problems such as tensor reorientation and interpolation, etc.

Fibers co-registration has recently been proposed as an alternative to DTI image co-registration (Leemans et al., 2006; Mayer et al., 2007; Ziyan et al., 2007). However, these methods either suffer from the complexity in fiber-to-fiber mapping and alignment or requires a initial bundling of fibers prior to co-registration, which itself is already a big challenge.

To address the limitations in the afore-mentioned bundling and registration techniques, we propose a Unified FIber Bundling and REgistration (UFIBRE) algorithm (Xu et al., 2009). Our method starts with an initial bundling of fibers in a template fiber set, and uses an expectation maximization algorithm to jointly estimate corresponding fiber bundles in a target fiber set and the transformation from the template to the target coordinate system. The initial bundling is achieved by using the manual ROI method, which provides an opportunity to select or define any fiber bundles of interest. Our method is efficient, as only the Gaussian statistics of the bundle model is aligned and there is no need to seek the alignments of individual fibers. Such a computational efficiency permits the use of more complex transformations, such as thin plate spline transformations, to gain higher degrees of freedom for mapping template fibers to target fibers.

2. Problem formulation

The goal of this work is to cluster fibers in a target fiber set and align them with a labeled template fiber set. This can be cast as an optimization problem that simultaneously seeks optimal bundles in the target fiber set and an optimal transformation from the template to the target coordinate system. Let $\mathbf{x}$ and $\mathbf{y}$ denote the template and target fiber set respectively. Each set contains a collection of open space curves, with each curve represented by a sequence of discrete 3D points. Let $\mathbf{x}$ and $\mathbf{y}$ be respectively divided into K fiber bundles, each of which contains a group of fibers that belong to a certain anatomical structure. Using appropriate resampling techniques, each fiber can be represented as a high dimensional vector and each fiber bundle is modeled by a Gaussian. Naturally a Gaussian mixture model is adopted here to represent the fiber distribution in

the whole template/target fiber set. Let $\boldsymbol{\mu}_x$ and $\boldsymbol{\mu}_y$ denote the means of the fiber bundles (defined as 'central curves' henceafter) in $\mathbf{x}$ and $\mathbf{y}$ respectively, $\boldsymbol{\sigma}_x$ and $\boldsymbol{\sigma}_y$ the covariance matrices, $\boldsymbol{\pi}_x$ and $\boldsymbol{\pi}_y$ the mixture proportions of each bundle Gaussian model, and $\mathbf{T}$ the transformation that maps $(\boldsymbol{\pi}_x, \boldsymbol{\mu}_x, \boldsymbol{\sigma}_x)$ to $(\boldsymbol{\pi}_y, \boldsymbol{\mu}_y, \boldsymbol{\sigma}_y)$.

Set $\mathbf{y}$ represents the target fibers generated tractographically from all appropriate seeds in a whole DTI data volume, while $\mathbf{x}$ only contains certain fibers of interest in the template dataset for a specific study. Assuming the template bundle parameters $(\boldsymbol{\pi}_x, \boldsymbol{\mu}_x, \boldsymbol{\sigma}_x)$ are known *a priori*, one goal of this work is to determine the target fiber bundles that are consistent with the template. Another goal is to find an optimal transformation that maps fibers from the template to the target coordinate system. Taken together, these can be expressed as a joint estimation of the target bundle model $(\boldsymbol{\pi}_y, \boldsymbol{\mu}_y, \boldsymbol{\sigma}_y)$ and the transformation $\mathbf{T}$ given $(\mathbf{x}, \mathbf{y}, \boldsymbol{\pi}_x, \boldsymbol{\mu}_x, \boldsymbol{\sigma}_x)$. This can be formally defined as a Bayesian decision problem, for which an optimal solution can be obtained by a maximum *a posteriori* (MAP) approach.

3. MAP estimation

Given $(\mathbf{x}, \mathbf{y}, \boldsymbol{\pi}_x, \boldsymbol{\mu}_x, \boldsymbol{\sigma}_x)$, the estimation problem is to find an optimal $(\boldsymbol{\pi}_y, \boldsymbol{\mu}_y, \boldsymbol{\sigma}_y)$ and $\mathbf{T}$ that maximizes the posterior probability as below,

$$\begin{aligned} \boldsymbol{\theta} &= (\mathbf{T}, \boldsymbol{\mu}_y, \boldsymbol{\sigma}_y, \boldsymbol{\pi}_y) \\ &= \arg\max_{T, \mu_y, \sigma_y, \pi_y} p(\mathbf{T}, \boldsymbol{\mu}_y, \boldsymbol{\sigma}_y, \boldsymbol{\pi}_y \mid \mathbf{x}, \mathbf{y}, \boldsymbol{\mu}_x, \boldsymbol{\sigma}_x, \boldsymbol{\pi}_x) \\ &\approx \arg\max_{T, \mu_y, \sigma_y, \pi_y} p(\mathbf{y} \mid \boldsymbol{\mu}_y, \boldsymbol{\sigma}_y, \boldsymbol{\pi}_y)\, p(\boldsymbol{\mu}_y, \boldsymbol{\sigma}_y, \boldsymbol{\pi}_y \mid \boldsymbol{\mu}_x, \boldsymbol{\sigma}_x, \boldsymbol{\pi}_x, \mathbf{T})\, p(\mathbf{T}) \end{aligned} \quad , \quad (3.1)$$

where $p(\mathrm{A}|\mathrm{B})$ denotes the conditional probability of A given B.

Assuming $\mathbf{y}$ is a set of independent and identically distributed fibers that are drawn from the target mixture Gaussian model $(\boldsymbol{\pi}_{\mathbf{y}}, \boldsymbol{\mu}_{\mathbf{y}}, \boldsymbol{\sigma}_{\mathbf{y}})$, the likelihood of $\mathbf{y}$ conditioned on $(\boldsymbol{\pi}_{\mathbf{y}}, \boldsymbol{\mu}_{\mathbf{y}}, \boldsymbol{\sigma}_{\mathbf{y}})$ can be simplified as the product of the likelihood of each fiber as follows,

$$\begin{aligned} & p(\mathbf{y} \mid \boldsymbol{\mu}_{\mathbf{y}}, \boldsymbol{\sigma}_{\mathbf{y}}, \boldsymbol{\pi}_{\mathbf{y}}) \\ &= \prod_{j=1}^{M} p(\mathbf{y}_j \mid \boldsymbol{\mu}_{\mathbf{y}}, \boldsymbol{\sigma}_{\mathbf{y}}, \boldsymbol{\pi}_{\mathbf{y}}) \quad , \\ &= \prod_{j=1}^{M} \sum_{k=1}^{K} \boldsymbol{\pi}_{\mathbf{y},k}\, p(\mathbf{y}_j \mid \boldsymbol{\mu}_{\mathbf{y},k}, \boldsymbol{\sigma}_{\mathbf{y},k}) \end{aligned} \tag{3.2}$$

where

$$p(\mathbf{y}_j \mid \boldsymbol{\mu}_{\mathbf{y},k}, \boldsymbol{\sigma}_{\mathbf{y},k}) = \prod_{i=1}^{N_k} \frac{1}{(2\pi)^{3/2} \mid \boldsymbol{\sigma}_{\mathbf{y},k,i} \mid^{1/2}} \exp(-(\mathbf{y}_{j,i} - \boldsymbol{\mu}_{\mathbf{y},k,i}) \boldsymbol{\sigma}_{\mathbf{y},k,i}^{-1} (\mathbf{y}_{j,i} - \boldsymbol{\mu}_{\mathbf{y},k,i})^T) \,. \tag{3.3}$$

Note that *k, j* and *i* index fiber bundles, fibers in the target fiber set and the points along each fiber respectively; there are *M* fibers in $\mathbf{y}$, *K* bundles of interest that need to be estimated, and N_k points on the central fiber $\boldsymbol{\mu}_{\mathbf{y},k}$ of the kth fiber bundle. Therefore, $\boldsymbol{\mu}_{\mathbf{y},k,i}$ is the coordinate of the ith point on the central fiber of the kth target bundle, and $\boldsymbol{\sigma}_{\mathbf{y},k,i}$ is the 3×3 covariance matrix of the distribution of the points corresponding to $\boldsymbol{\mu}_{\mathbf{y},k,i}$. Variable $\mathbf{y}_{j,i}$ denotes the point in the jth fiber corresponding to $\boldsymbol{\mu}_{\mathbf{y},k,i}$, which is generated by the resampling scheme introduced in chapter II.

It should be noted that the soundness of Equation 3.3 above is based on the assumption that each fiber point can be modeled as a mixture of 3D Gaussian probability distributions and the distribution of each point is independent of other points in the same fiber.

The probability in Equation 3.2 describes the likelihood of the target fibers conditioned on the Gaussian mixture model $(\boldsymbol{\pi}_y, \boldsymbol{\mu}_y, \boldsymbol{\sigma}_y)$ (i.e. how well the target fibers data fit the model). It can be regarded as a clustering term, whose maximization would lead to optimal bundling of the fibers into *K* clusters on the basis of the target data only. However, maximization of such a clustering term alone cannot ensure the consistency in the fiber bundles between the target and the given template, nor does it give any alignment information. To associate the target with the given template, the prior probability $p(\boldsymbol{\mu}_y, \boldsymbol{\sigma}_y, \boldsymbol{\pi}_y \mid \boldsymbol{\mu}_x, \boldsymbol{\sigma}_x, \boldsymbol{\pi}_x, \mathbf{T})$ has to be optimized as well.

A reasonable expression of $p(\boldsymbol{\mu}_y, \boldsymbol{\sigma}_y, \boldsymbol{\pi}_y \mid \boldsymbol{\mu}_x, \boldsymbol{\sigma}_x, \boldsymbol{\pi}_x, \mathbf{T})$ should be related to the similarity between the warped template model $\mathbf{T}(\boldsymbol{\mu}_x, \boldsymbol{\sigma}_x, \boldsymbol{\pi}_x)$ and the target model $(\boldsymbol{\mu}_y, \boldsymbol{\sigma}_y, \boldsymbol{\pi}_y)$. There exist metrics that measure the similarity between Gaussian mixture models (e.g. Kullback Leibler divergence), whose optimization would lead to alignment of both central fibers and covariance. However, they are not used in this work due to difficulties in their optimizations. To make the optimization more tractable, only the similarity between $\mathbf{T}(\boldsymbol{\mu}_x)$ and $(\boldsymbol{\mu}_y)$ is considered, i.e., only the consistency between the central fibers of the template and target bundles is sought. The mixture proportions $\boldsymbol{\pi}_y$ and the covariance matrices $\boldsymbol{\sigma}_y$ of the target bundles are determined by the clustering term (Equation 3.2). Therefore, $p(\boldsymbol{\mu}_y, \boldsymbol{\sigma}_y, \boldsymbol{\pi}_y \mid \boldsymbol{\mu}_x, \boldsymbol{\sigma}_x, \boldsymbol{\pi}_x, \mathbf{T})$ can be simplified as $p(\boldsymbol{\mu}_y \mid \boldsymbol{\mu}_x, \mathbf{T})$. It is further assumed that the probability distribution of errors between the central fibers of the target and template data is Gaussian, and the covariance matrices are proportional to those of the target models. Therefore, $p(\boldsymbol{\mu}_y \mid \boldsymbol{\mu}_x, \mathbf{T})$ is expressed as

$$p(\boldsymbol{\mu}_{\mathbf{y}} \mid \boldsymbol{\mu}_{\mathbf{x}}, \mathbf{T})$$
$$= \prod_{k=1}^{K} \prod_{i=1}^{N_k} \frac{1}{(2\pi)^{3/2} \mid \boldsymbol{\sigma}_{\mathbf{y,k,i}} \mid^{1/2}} \exp(-\boldsymbol{c}(\boldsymbol{\mu}_{\mathbf{y},k,i} - \mathbf{T}(\boldsymbol{\mu}_{\mathbf{x},k,i}))\boldsymbol{\sigma}_{\mathbf{y,k,i}}^{-1}(\boldsymbol{\mu}_{\mathbf{y},k,i} - \mathbf{T}(\boldsymbol{\mu}_{\mathbf{x},k,i})^T)), \quad (3.4)$$

where $|\boldsymbol{\sigma}_{\mathbf{y},k,i}|$ denotes the determinant of $\boldsymbol{\sigma}_{\mathbf{y},k,i}$ and c is a parameter that controls the contribution of $p(\boldsymbol{\mu}_{\mathbf{y}} \mid \boldsymbol{\mu}_{\mathbf{x}}, \mathbf{T})$ to the overall objective function. Maximization of above probability would yield a transformation **T** that optimally registers the central fibers of template fiber bundles with those of target fiber bundles, and also leverage the computation of $(\boldsymbol{\mu}_{\mathbf{y}}, \boldsymbol{\sigma}_{\mathbf{y}})$ by giving preference to target bundles that are consistent with template bundles.

Finally, $p(\mathbf{T})$ denotes the prior distribution of the transformation **T**. It needs to be selected such that the trade-off between the registration accuracy and the smoothness of the deformation fields is adequately balanced. The form of $p(\mathbf{T})$ used in this study will be detailed later.

Taken together, maximization of all the probabilities in Equation 3.1 yields an optimal set of parameters that allow the target fibers to be bundled consistently with the given template bundles.

4. Optimization

Based on the above derivations of the posterior distribution, the MAP estimation can be expressed as maximization of the following Log probability function,

$$E(\mathbf{T}, \boldsymbol{\mu}_{\mathbf{y}}, \boldsymbol{\sigma}_{\mathbf{y}}, \boldsymbol{\pi}_{\mathbf{y}})$$
$$= \sum_{j=1}^{M} \log(\sum_{k=1}^{K} \boldsymbol{\pi}_{\mathbf{y},k} \prod_{i=1}^{N_k} \frac{1}{(2\pi)^{3/2} \mid \boldsymbol{\sigma}_{\mathbf{y,k,i}} \mid^{1/2}} \exp(-(\mathbf{y}_{j,i} - \boldsymbol{\mu}_{\mathbf{y,k,i}})\boldsymbol{\sigma}_{\mathbf{y,k,i}}^{-1}(\mathbf{y}_{j,i} - \boldsymbol{\mu}_{\mathbf{y,k,i}})^T)) \quad (3.5)$$
$$- \sum_{k=1}^{K} \sum_{i=1}^{N_k} c(\boldsymbol{\mu}_{\mathbf{y},k,i} - \mathbf{T}(\boldsymbol{\mu}_{\mathbf{x},k,i}))\boldsymbol{\sigma}_{\mathbf{y,k,i}}^{-1}(\boldsymbol{\mu}_{\mathbf{y},k,i} - \mathbf{T}(\boldsymbol{\mu}_{\mathbf{x},k,i}))^T + \log(p(\mathbf{T}))$$

The above function can be maximized by using the well-known expectation-maximization (EM) algorithm. Starting with an initial parameter $\boldsymbol{\theta}$, this algorithm finds the optimal parameter $\boldsymbol{\theta}$ by iteratively performing an expectation step and a maximization step until convergence.

1) Expectation step: In the expectation step of the nth iteration, the membership probability $m_{j,k}{}^{n}$ of each fiber $\mathbf{y}_j$ belonging to the fiber bundle $(\boldsymbol{\mu}_{\mathbf{y},k}, \boldsymbol{\sigma}_{\mathbf{y},k})$ is estimated using the most recent estimate of parameter $\boldsymbol{\theta}^{n-1}$:

$$m_{j,k}{}^{n} = \frac{\pi_{y,k}{}^{n-1} p(\mathbf{y}_j \mid \boldsymbol{\mu}_{\mathbf{y},k}{}^{n-1}, \boldsymbol{\sigma}_{\mathbf{y},k}{}^{n-1})}{\sum_{k=1}^{K} \pi_{y,k}{}^{n-1} p(\mathbf{y}_j \mid \boldsymbol{\mu}_{\mathbf{y},k}{}^{n-1}, \boldsymbol{\sigma}_{\mathbf{y},k}{}^{n-1})}, \tag{3.6}$$

where the superscript denotes the iteration number.

2) Maximization step: In the maximization step of the nth iteration, the parameters $(\boldsymbol{\mu}_{\mathbf{y}}{}^{n}, \boldsymbol{\sigma}_{\mathbf{y}}{}^{n}, \mathbf{T}^{n})$ are optimized to minimize the objective function below:

$$\begin{aligned}
&E_{EM}(\mathbf{T}^{n}, \boldsymbol{\mu}_{\mathbf{y}}{}^{n}, \boldsymbol{\sigma}_{\mathbf{y}}{}^{n}) \\
&= -\sum_{j=1}^{M}\sum_{k=1}^{K} m_{j,k}{}^{n} \log(p(y_j \mid \mu_{y,k}, \sigma_{y,k})) - \sum_{k=1}^{K} \log(p(T(\mu_{x,k}) \mid \mu_{y,k}, \sigma_{y,k})) - \log(p(\mathbf{T}^{n})) \\
&= \sum_{j=1}^{M}\sum_{k=1}^{K} m_{j,k}{}^{n} \sum_{i=1}^{N_k} (\frac{1}{2}\log \mid \boldsymbol{\sigma}_{\mathbf{y,k,i}}{}^{n} \mid + \frac{1}{2}(\mathbf{y}_{j,i} - \boldsymbol{\mu}_{\mathbf{y,k,i}}{}^{n})(\boldsymbol{\sigma}_{\mathbf{y,k,i}}{}^{n})^{-1}(\mathbf{y}_{j,i} - \boldsymbol{\mu}_{\mathbf{y,k,i}}{}^{n})^{T}) \qquad ,(3.7) \\
&+ \sum_{k=1}^{K}\sum_{i=1}^{N_k} c(\frac{1}{2}\log \mid \boldsymbol{\sigma}_{\mathbf{y,k,i}}{}^{n} \mid + \frac{1}{2}(\boldsymbol{\mu}_{\mathbf{y},k,i}{}^{n} - \mathbf{T}^{n}(\boldsymbol{\mu}_{\mathbf{x},k,i}))(\boldsymbol{\sigma}_{\mathbf{y,k,i}}{}^{n})^{-1}(\boldsymbol{\mu}_{\mathbf{y},k,i}{}^{n} - \mathbf{T}^{n}(\boldsymbol{\mu}_{\mathbf{x},k,i}))^{T}) \\
&- \log(p(\mathbf{T}^{n}))
\end{aligned}$$

where we heuristically assume that the mixture proportions in the target model are the same as in the template model ($\boldsymbol{\pi}_{\mathbf{y}} = \boldsymbol{\pi}_{\mathbf{x}}$).

To obtain the optimal $(\boldsymbol{\mu}_{\mathbf{y}}{}^{n}, \boldsymbol{\sigma}_{\mathbf{y}}{}^{n})$ that minimizes Equation 3.7, the below two differential equations are solved,

$$\frac{dE_{EM}}{d\boldsymbol{\mu}_{\mathbf{y}}{}^{n}} = \sum_{j=1}^{M}\sum_{k=1}^{K} m_{j,k}{}^{n} \sum_{i=1}^{N_k}((\mathbf{y}_{j,i} - \boldsymbol{\mu}_{\mathbf{y},\mathbf{k},\mathbf{i}}{}^{n})(\boldsymbol{\sigma}_{\mathbf{y},\mathbf{k},\mathbf{i}}{}^{n})^{-1}) + \sum_{k=1}^{K}\sum_{i=1}^{N_k} c((\mathbf{T}^{n-1}(\boldsymbol{\mu}_{\mathbf{x},k,i}) - \boldsymbol{\mu}_{\mathbf{y},k,i}{}^{n})(\boldsymbol{\sigma}_{\mathbf{y},\mathbf{k},\mathbf{i}}{}^{n})^{-1}) = 0$$

,

$$\frac{dE_{EM}}{d\sigma_y} = \sum_{j=1}^{M}\sum_{k=1}^{K} m_{j,k}{}^{n} \sum_{i=1}^{N_k}(-\frac{1}{2}\frac{1}{|(\boldsymbol{\sigma}_{\mathbf{y},\mathbf{k},\mathbf{i}}{}^{n})^{-1}|}|(\boldsymbol{\sigma}_{\mathbf{y},\mathbf{k},\mathbf{i}}{}^{n})^{-1}|\boldsymbol{\sigma}_{\mathbf{y},\mathbf{k},\mathbf{i}}{}^{n} + \frac{1}{2}(\mathbf{y}_{j,i} - \boldsymbol{\mu}_{\mathbf{y},\mathbf{k},\mathbf{i}}{}^{n})^{T}(\mathbf{y}_{j,i} - \boldsymbol{\mu}_{\mathbf{y},\mathbf{k},\mathbf{i}}{}^{n}))$$

$$+ \sum_{k=1}^{K}\sum_{i=1}^{N_k} c(-\frac{1}{2}\frac{1}{|(\boldsymbol{\sigma}_{\mathbf{y},\mathbf{k},\mathbf{i}}{}^{n})^{-1}|}|(\boldsymbol{\sigma}_{\mathbf{y},\mathbf{k},\mathbf{i}}{}^{n})^{-1}|\boldsymbol{\sigma}_{\mathbf{y},\mathbf{k},\mathbf{i}}{}^{n} + \frac{1}{2}(\boldsymbol{\mu}_{\mathbf{y},k,i}{}^{n} - \mathbf{T}^{n-1}(\boldsymbol{\mu}_{\mathbf{x},k,i}))^{T}(\boldsymbol{\mu}_{\mathbf{y},k,i}{}^{n} - \mathbf{T}^{n-1}(\boldsymbol{\mu}_{\mathbf{x},k,i}))) .$$

Using the knowledge from matrix calculus $\frac{d(x^T Ax)}{dx} = x^T(A^T + A)$ for the first equation, where A and x denote a matrix and a vector respectively, we obtain the below solution for $\boldsymbol{\mu}_{\mathbf{y}}{}^{n}$,

$$\boldsymbol{\mu}_{\mathbf{y},\boldsymbol{k},\boldsymbol{i}}{}^{n} = \frac{\sum_{j=1}^{M} m_{j,k}{}^{n}\mathbf{y}_{j,i} + c\mathbf{T}^{n-1}(\boldsymbol{\mu}_{\mathbf{x},k,i})}{\sum_{j=1}^{M} m_{j,k}{}^{n} + c} \quad . \tag{3.8a}$$

Recalling the formula $\frac{d(trace(AXB))}{d(X)} = BA, \frac{d(|X|)}{dX} = |X|X^{-1}$, where B and X are also matrices, we obtain the solution for $\boldsymbol{\sigma}_{\mathbf{y}}{}^{n}$,

$$\boldsymbol{\sigma}_{\mathbf{y},\boldsymbol{k},\boldsymbol{i}}{}^{n} = \frac{\sum_{j=1}^{M} m_{j,k}{}^{n}(\mathbf{y}_{j,i} - \boldsymbol{\mu}_{\mathbf{y},\boldsymbol{k},\boldsymbol{i}}{}^{n})(\mathbf{y}_{j,i} - \boldsymbol{\mu}_{\mathbf{y},\boldsymbol{k},\boldsymbol{i}}{}^{n})^{T} + c(\boldsymbol{\mu}_{\mathbf{y},k,i}{}^{n} - \mathbf{T}^{n-1}(\mu_{\mathbf{x},k,i}))(\boldsymbol{\mu}_{\mathbf{y},k,i}{}^{n} - \mathbf{T}^{n-1}(\boldsymbol{\mu}_{\mathbf{x},k,i}))^{T}}{\sum_{j=1}^{M} m_{j,k}{}^{n} + c} . \tag{3.8b}$$

Equation 3.8 can be rearranged as follows,

$$\boldsymbol{\mu}_{\mathbf{y},k,i}{}^{n}$$

$$= \left(\frac{\sum_{j=1}^{M} m_{j,k}{}^{n}}{\sum_{j=1}^{M} m_{j,k}{}^{n} + c}\right)\left(\frac{\sum_{j=1}^{M} m_{j,k}{}^{n}\mathbf{y}_{j,i}}{\sum_{j=1}^{M} m_{j,k}{}^{n}}\right) + \left(\frac{c}{\sum_{j=1}^{M} m_{j,k}{}^{n} + c}\right)\mathbf{T}^{n-1}(\boldsymbol{\mu}_{\mathbf{x},k,i}) \quad , \tag{3.9a}$$

$$= \left(1 - \frac{c}{\sum_{j=1}^{M} m_{j,k}{}^{n} + c}\right)\left(\frac{\sum_{j=1}^{M} m_{j,k}{}^{n}\mathbf{y}_{j,i}}{\sum_{j=1}^{M} m_{j,k}{}^{n}}\right) + \left(\frac{c}{\sum_{j=1}^{M} m_{j,k}{}^{n} + c}\right)\mathbf{T}^{n-1}(\boldsymbol{\mu}_{\mathbf{x},k,i})$$

$$\boldsymbol{\sigma}_{\mathbf{y},k,i}{}^{n}$$

$$= \left(1 - \frac{c}{\sum_{j=1}^{M} m_{j,k}{}^{n} + c}\right)\left(\frac{\sum_{j=1}^{M} m_{j,k}{}^{n}(\mathbf{y}_{j,i} - \boldsymbol{\mu}_{\mathbf{y},k,i}{}^{n})(\mathbf{y}_{j,i} - \boldsymbol{\mu}_{\mathbf{y},k,i}{}^{n})^{T}}{\sum_{j=1}^{M} m_{j,k}{}^{n}}\right) \quad . \tag{3.9b}$$

$$+ \left(\frac{c}{\sum_{j=1}^{M} m_{j,k}{}^{n} + c}\right)\left((\boldsymbol{\mu}_{\mathbf{y},k,i}{}^{n} - \mathbf{T}^{n-1}(\mu_{\mathbf{x},k,i}))(\boldsymbol{\mu}_{\mathbf{y},k,i}{}^{n} - \mathbf{T}^{n-1}(\boldsymbol{\mu}_{\mathbf{x},k,i}))^{T}\right)$$

Equation 3.9 is then further simplified as

$$\boldsymbol{\mu}_{\mathbf{y}}{}^{n} = (1 - C)\boldsymbol{\mu}_{b/\mathbf{y}}{}^{n} + C\boldsymbol{\mu}_{r/\mathbf{y}}{}^{n}, \tag{3.10a}$$

$$\boldsymbol{\sigma}_{\mathbf{y}}{}^{n} = (1 - C)\boldsymbol{\sigma}_{b/\mathbf{y}}{}^{n} + C\boldsymbol{\sigma}_{r/\mathbf{y}}{}^{n}, \tag{3.10b}$$

where

$$C = \left(\frac{c}{\sum_{j=1}^{M} m_{j,k}{}^{n} + c}\right)$$

$$\boldsymbol{\mu}_{b/\mathbf{y},k,i}{}^{n} = \left(\frac{\sum_{j=1}^{M} m_{j,k}{}^{n}\mathbf{y}_{j,i}}{\sum_{j=1}^{M} m_{j,k}{}^{n}}\right),$$

$$\boldsymbol{\sigma}_{\boldsymbol{b/y,k,i}}{}^{n} = \frac{\sum_{j=1}^{M} m_{j,k}{}^{n}(\mathbf{y}_{j,i} - \boldsymbol{\mu}_{\mathbf{y},\boldsymbol{k,i}}{}^{n})(\mathbf{y}_{j,i} - \boldsymbol{\mu}_{\mathbf{y},\boldsymbol{k,i}}{}^{n})^{T}}{\sum_{j=1}^{M} m_{j,k}{}^{n}},$$

$$\boldsymbol{\mu}_{\boldsymbol{r/y,k,i}}{}^{n} = \mathbf{T}^{n-1}(\boldsymbol{\mu}_{\mathbf{x},k,i}),$$

$$\boldsymbol{\sigma}_{r/\mathbf{y},\boldsymbol{k,i}}{}^{n} = (\boldsymbol{\mu}_{\mathbf{y},k,i}{}^{n} - \mathbf{T}^{n-1}(\mu_{\mathbf{x},k,i}))(\boldsymbol{\mu}_{\mathbf{y},k,i}{}^{n} - \mathbf{T}^{n-1}(\boldsymbol{\mu}_{\mathbf{x},k,i}))^{T}.$$

$\boldsymbol{\mu}_{\boldsymbol{b/y}}{}^{n}$ and $\boldsymbol{\sigma}_{\boldsymbol{b/y}}{}^{n}$ denote the central fibers and covariance matrices that are obtained by maximizing bundling term $p(\mathbf{y} \mid \boldsymbol{\mu}_{\mathbf{y}}, \boldsymbol{\sigma}_{\mathbf{y}}, \boldsymbol{\pi}_{\mathbf{y}})$ alone (Equation 3.2). $\boldsymbol{\mu}_{\boldsymbol{r/y}}{}^{n}$ denote the warped template central fibers using the transformation estimated in the previous iteration. The central fibers $\boldsymbol{\mu}_{\mathbf{y}}{}^{n}$ in the proposed algorithm are actually computed as a weighted sum of $\boldsymbol{\mu}_{\boldsymbol{b/y}}{}^{n}$ and $\boldsymbol{\mu}_{\boldsymbol{r/y}}{}^{n}$, with their relative weight *C* controlled by the parameter *c* (Equation 3.10a). The weight *C* is chosen to be one of the core adjustable parameters in the algorithm. The choice of *C* and its effect on the performance of the UFIBRE algorithm will be studied experimentally.

In principle, evaluations of the above formulas (Equation 3.10) for each bundle involve all the fibers in target fiber set. However, the fibers with low membership probability $m_{j,k}{}^{n}$ are excluded from the computation of $\boldsymbol{\mu}_{\mathbf{y},k}$ for the sake of computational efficiency. To do so, the target fibers are first sorted in an ascending order of Mahalanobis distance to the target central fibers, which is computed as follows,

$$Dist_{j,k} = \sum_{i=1}^{N_k}((\mathbf{y}_{j,i} - \boldsymbol{\mu}_{\mathbf{y},\boldsymbol{k,i}}{}^{n})(\boldsymbol{\sigma}_{\mathbf{y},\boldsymbol{k,i}}{}^{n})^{-1}(\mathbf{y}_{j,i} - \boldsymbol{\mu}_{\mathbf{y},\boldsymbol{k,i}}{}^{n})^{T}),$$

where $Dist_{j,k}$ denotes the distance between the *j*th fiber and the *k*th bundle in the target fiber set. Assuming the number of fibers in the *k*th template bundle is M_k, the first M_k

target fibers with smallest $Dist_{j,k}$ are retained for the kth target bundle while the remaining fibers are excluded as outliers.

Lastly, the optimal $\mathbf{T}^n$ is given by minimizing the following objective function:

$$E_{EM}(\mathbf{T}) = \sum_{k=1}^{K}\sum_{i-1}^{N_k} c(\boldsymbol{\mu}_{\mathbf{y},k,i}{}^n - \mathbf{T}^n(\boldsymbol{\mu}_{\mathbf{x},k,i}{}^n))(\boldsymbol{\sigma}_{\mathbf{y},\boldsymbol{k},\boldsymbol{i}}{}^n)^{-1}(\boldsymbol{\mu}_{\mathbf{y},k,i}{}^n - \mathbf{T}^n(\boldsymbol{\mu}_{\mathbf{x},k,i}{}^n))^T + \log(p(\mathbf{T}^n)). \quad (3.11)$$

5. Transformation

The above EM framework does not assume any form of transformation, i.e. transformation from rigid, affine to more complex forms may be used in this framework. Both rigid and non-rigid transformations are integrated in the UFIBRE algorithm to achieve a robust and accurate mapping between template and target datasets. Thin plate spline (TPS) is chosen as the non-rigid transformation, because it has high degrees of freedom and smoothness in deformation and closed-form solution for warping and parameter estimation. A unit quaternion is used to represent the rotation part of the rigid transformation, as it can lead to simple optimization.

Let $\mathbf{v}_m$, $\boldsymbol{\delta}_m$ and $\mathbf{p}_m$ denote $\boldsymbol{\mu}_{\mathbf{x},k,i}{}^n$, $\boldsymbol{\sigma}_{\mathbf{y},k,i}{}^n$ and $\boldsymbol{\mu}_{\mathbf{y},k,i}{}^n$ respectively, where $m = i + \sum_{j=1}^{k-1} N_j, k \in [1,...,K], i \in [1,...,N_k], m \in [1,...,S]$. With these simplified notations, Equation 3.11 is rewritten as,

$$E_{EM}(\mathbf{T}) = \sum_{m=1}^{S}(\mathbf{p}_m - \mathbf{T}(\mathbf{v}_m))(\boldsymbol{\delta}_m)^{-1}(\mathbf{p}_m - \mathbf{T}(\mathbf{v}_m))^T + \log(p(\mathbf{T})). \quad (3.12)$$

A. Estimation of rigid transformation

A rigid transformation for a point u can be expressed as,

$$\mathbf{T}(u) = \mathbf{R}\mathbf{u} + \mathbf{t}, \quad (3.13)$$

where **t** is a 3×1 translation vector, and **R** is a 3×3 rotation matrix that is subject to $\mathbf{R}^T\mathbf{R}=\mathbf{I}$ and the determinant of **R** is 1 (proper rotation).

The objective function in Equation 3.12 is expressed as,

$$E_{EM}(\mathbf{R},\mathbf{t}) = \sum_{m=1}^{S} (\mathbf{p}_m - \mathbf{R}\mathbf{v}_m - \mathbf{t}))(\boldsymbol{\delta}_m)^{-1}(\mathbf{p}_m - \mathbf{R}\mathbf{v}_m - \mathbf{t})^T \ . \qquad (3.14)$$

So far there is no existing closed-form solution for estimating **R** that minimizes $E_{EM}(\mathbf{R},\mathbf{t})$, so an iterative algorithm (Ohta et al., 1998) is used to find **R**. The algorithm represents the rotation matrix **R** with a unit quaternion for simple optimization. A rotation by angle Ω around a 3×1 unit vector **l** can be represented by a 4×1 unit vector **q** such that,

$$\mathbf{q} = \begin{bmatrix} q_0 \\ \mathbf{q}_l \end{bmatrix} = \begin{bmatrix} \cos\frac{\Omega}{2} \\ \sin\frac{\Omega}{2}\mathbf{l} \end{bmatrix}.$$

The iterative algorithm (Ohta et al., 1998) that finds an optimal R can be summarized as follows,

---

Sub-algorithm 1: estimating **q** that minimizes $E_{EM}(\mathbf{R},\mathbf{t})$

Input: $\mathbf{v}_m, \boldsymbol{\delta}_m, \mathbf{p}_m$. *Output:* **q**.

1: Compute a 3×4 matrix $\mathbf{X_m}$:

$$\mathbf{X_m} = \left[(\mathbf{p}_m - \mathbf{v}_m), (\mathbf{p}_m - \mathbf{v}_m) \times \mathbf{I}_{3\times 3}\right]$$

where the product $\mathbf{a} \times \mathbf{A}$ of a vector **a** and a matrix **A** is a matrix whose column vectors are the cross product of **a** and column vectors of **A**.

2: Set b = 0 and $\mathbf{W}_m = \mathbf{I}_{3\times 3}$.

3: Compute a 4×4 matrix **M**:

$$\mathbf{M} = \sum_{m=1}^{S} \mathbf{X}_m{}^T \mathbf{W}_m \mathbf{X}_m \ .$$

4: Compute a 4×4 matrix **N**:

$$\mathbf{N} = \begin{bmatrix} n_0 & \mathbf{n}^T \\ \mathbf{n} & \mathbf{N'} \end{bmatrix},$$

where

$$n_0 = \sum_{m=1}^{S} (\mathbf{W}_m : \boldsymbol{\delta}_m) \,,$$

$$\mathbf{n} = 2\sum_{m=1}^{S} t_3[A[\mathbf{W}_m \boldsymbol{\delta}_m]] \,,$$

$$\mathbf{N'} = \sum_{m=1}^{S} (\mathbf{W}_m \times \boldsymbol{\delta}_m) \,.$$

The inner product (**A**: **B**) of matrices $\mathbf{A} = (A_{i,j})$ and $\mathbf{B} = (B_{i,j})$ is a scalar value that is defined by $\sum_{i,j} (A_{i,j} B_{i,j})$ .The outer product **A**×**B** is a matrix whose element in the ith row and the jth column is defined as $\sum_{k,l,m,n} \varepsilon_{i,k,l} \varepsilon_{j,m,n} A_{k,m} B_{l,n}$, where $\varepsilon_{i,k,l}$ is levi-civita symbol,

$$\varepsilon_{i,k,l} = \begin{cases} +1, if\,(i,k,l) is (1,2,3),(3,1,2),(2,3,1) \\ -1, if\,(i,k,l) is (3,2,1),(1,3,2),(2,1,3) \\ 0, otherwise \end{cases}.$$

The matrix operator $A[]$ is $A[\mathbf{A}] = (\mathbf{A} - \mathbf{A}^T)/2$. The matrix operator *t3*[] is $t3[\mathbf{A}] = [A_{3,2}, A_{1,3}, A_{2,1}]^T$.

5: Compute the smallest eigenvalue of matrix **M**-b**N** and the corresponding normalized eigenvector **q**.

6: If the absolute value of the eigenvalue is close to zero, stop and return **q**. Otherwise,

update b and $\mathbf{W}_m$ as follows and go to step 3,

$$\mathbf{W}_m = (q_0{}^2\delta_m + 2q_0 S[\mathbf{q}_l \times \delta_m] + \mathbf{q}_l \times \delta_m \times \mathbf{q}_l)^{-1},$$

where the matrix operator S[] is $S[\mathbf{A}] = (\mathbf{A} + \mathbf{A}^T)/2$. The outer product $\mathbf{a} \times \mathbf{A} \times \mathbf{a}$ of a vector $\mathbf{a}$ and a matrix $\mathbf{A}$ is a matrix whose element in the ith row and the jth column is defined as $\sum_{k,l,m,n} \varepsilon_{i,k,l}\varepsilon_{j,m,n} a_k a_m A_{l,n}$.

The rotation matrix **R** is then computed using the resulting **q**,

$$\mathbf{R} = (q_0{}^2 - |\mathbf{q}_l|)\mathbf{I}_{3\times3} + 2(\mathbf{q}_l\mathbf{q}_l{}^T + q_0\mathbf{q}_l \times \mathbf{I}_{3\times3}). \qquad (3.15)$$

The translation vector **t** is then computed using the **R**,

$$\mathbf{t} = (\sum_{m=1}^{S} \boldsymbol{\delta}_m)^{-1} \sum_{m=1}^{S} \boldsymbol{\delta}_m (\mathbf{p}_m - \mathbf{R}\mathbf{v}_m). \qquad (3.16)$$

B. Estimation of a TPS transformation

Using $\{\mathbf{v}_1, \mathbf{v}_2, ..., \mathbf{v}_m, ...\}$ as control points, a TPS transformation for a point *u* can be expressed as,

$$\mathbf{T}(u) = \mathbf{d}\mathbf{u} + \mathbf{w}\boldsymbol{\varphi}(\mathbf{u}), \qquad (3.17)$$

where **u** is a column vector $(u_x, u_y, u_z, 1)^T$ that represents the coordinate of a point; **d** denotes a 3×4 matrix that contains the affine part of TPS; $\boldsymbol{\varphi}(\mathbf{u})$ is an S×1 vector whose mth component $\phi_m(\mathbf{u})$ is $-\|\mathbf{u} - \mathbf{v}_m\|^2$; **w** is a 3×S coefficient matrix that transforms $\boldsymbol{\varphi}(\mathbf{u})$ to a coordinate.

The objective function in Equation 3.12 is then expressed as,

$$E_{EM}(\mathbf{d},\mathbf{w}) = \sum_{m=1}^{S} (\mathbf{p}_m - \mathbf{d}\mathbf{v}_m - \mathbf{w}\boldsymbol{\varphi}(\mathbf{v}_m))(\boldsymbol{\delta}_m)^{-1}(\mathbf{p}_m - \mathbf{d}\mathbf{v}_m - \mathbf{w}\boldsymbol{\varphi}(\mathbf{v}_m))^T + \lambda P(\mathbf{d},\mathbf{w}), \quad (3.18)$$

where $\lambda P(\mathbf{d},\mathbf{w})$ is the prior term of TPS and λ is a parameter that controls the degree of freedom in the TPS transformation (Rohr et al., 2001). A large λ implies a TPS with smaller freedom. In the extreme cases of $\lambda = +\infty$ and $\lambda = 0$, the TPS becomes an affine and a completely free transformation respectively.

To estimate the coefficients **d** and **w** that minimize $E_{EM}(\mathbf{d},\mathbf{w})$ (Equation 3.18), we solve the following system of linear equations,

$$\begin{matrix} (\mathbf{U} + S\lambda\mathbf{W}^{-1})\tilde{\mathbf{w}} + [\mathbf{V},\mathbf{V},\mathbf{V}]\tilde{\mathbf{d}} = \mathbf{P} \\ \mathbf{V}^{\mathbf{T}}\mathbf{w} = 0 \end{matrix}, \quad (3.19)$$

where **U** is a block matrix, each 3×3 component of which can be represented as $U_{m,n} = \mathbf{I}_{3\times3}\phi_m(v_n)$. Here $\mathbf{I}_{3\times3}$ is a 3×3 identity matrix. To incorporate anisotropic point localization errors, a weighting matrix **W** is introduced to the equations as follows (Rohr et al., 2001),

$$\mathbf{W}^{-1} = \begin{bmatrix} \boldsymbol{\delta}_1 & & & 0 \\ & \ddots & & \\ & & \ddots & \\ 0 & & & \boldsymbol{\delta}_S \end{bmatrix}.$$

V is a matrix composed of the coordinates of all the control points:

$$\mathbf{V} = \begin{bmatrix} 1 & v_{1x} & v_{1y} & v_{1z} \\ \vdots & \vdots & \vdots & \vdots \\ \vdots & \vdots & \vdots & \vdots \\ \vdots & \vdots & \vdots & \vdots \\ 1 & v_{Sx} & v_{Sy} & v_{Sz} \end{bmatrix}.$$

Similarly, **P** is expressed as:

$$\mathbf{P} = [p_{1x} \quad p_{1y} \quad p_{1z} \quad . \quad . \quad . \quad p_{Sx} \quad p_{Sy} \quad p_{Sz}]^T .$$

Note that in Equation 3.19, $\tilde{\mathbf{d}}$ and $\tilde{\mathbf{w}}$ are column vectors rearranged from the coefficient matrices **d** and **w**.

C. Coarse-to-fine registration

Rigid registration coarsely matches template to target fibers in a stable manner due to its limited freedom. On the other hand, TPS can accurately register two sets of fibers thanks to its high degree of freedom, but this freedom could also result in mapping template fibers to outlier target fibers. Therefore, the UFIBRE algorithm achieves a both stable and accurate registration of fiber bundles by smoothly increasing the degree of transformation freedom, from rigid to highly non-rigid. In our implementation, a rigid transformation is used for the first seven iterations to achieve a coarse but stable alignment between fiber bundles. Our pilot experiments show that seven iterations of rigid registration are sufficient to remove inter-subject differences that are caused by global rotation and translation. Following the rigid registration, a TPS transformation is used in subsequent eight iterations. To make the TPS smoothly transit from affine to highly non-rigid, we decrease λ in each iteration by a factor of ten from a starting value of 10^4 (instead of setting λ to a constant). The value of $\lambda = 10^4$ at the beginning yields a nearly pure affine transformation and the value of $\lambda = 10^{-4}$ ($10^4/10^8$) in the last iteration makes the TPS a highly free transformation.

6. Outline of the UFIBRE algorithm

Implementations of the UFIBRE algorithm are outlined as follow:

1) Rigid UFIBRE algorithm

Input: $\mathbf{x}$, $\mathbf{y}$ and $(\boldsymbol{\pi}_x, \boldsymbol{\mu}_x, \boldsymbol{\sigma}_x)$.

Output: **R, t.**

1: Initialize n, **R, t** and $(\boldsymbol{\pi}_y, \boldsymbol{\mu}_y, \boldsymbol{\sigma}_y)$ as 0, **I** and $(\boldsymbol{\pi}_x, \boldsymbol{\mu}_x, \boldsymbol{\sigma}_x)$.

2: Compute membership probability $m_{j,k}^{\,n+1}$ using Equation 3.3 and Equation 3.6.

3: Compute updated target bundle parameters $(\boldsymbol{\mu}_y^{\,n+1}, \boldsymbol{\sigma}_y^{\,n+1})$ using Equation 3.8 and Equation 3.13.

4: Compute unit quaternion **q** using sub-algorithm 1.

5: Compute updated rotation $\mathbf{R}^{n+1}$ using Equation 3.15.

6: Compute updated rotation $\mathbf{t}^{n+1}$ using Equation 3.16.

7: If n<7, go to step 2 and n = n+1; otherwise stop and return $\mathbf{R}^{n+1}$, $\mathbf{t}^{n+1}$.

2) Transform **x** *using the resulting rigid transformation and recalculate* $(\boldsymbol{\pi}_x, \boldsymbol{\mu}_x, \boldsymbol{\sigma}_x)$.

3) Non-rigid UFIBRE algorithm

Input: $\mathbf{x}$, $\mathbf{y}$ and $(\boldsymbol{\pi}_x, \boldsymbol{\mu}_x, \boldsymbol{\sigma}_x)$.

Output: **d**, **w**.

1: Initialize λ n, **d**, **w** and $(\boldsymbol{\pi}_y, \boldsymbol{\mu}_y, \boldsymbol{\sigma}_y)$ as 10^4, 0, **I** and $(\boldsymbol{\pi}_x, \boldsymbol{\mu}_x, \boldsymbol{\sigma}_x)$.

2: Compute membership probability $m_{j,k}^{\,n+1}$ using Equation 3.3 and Equation 3.6.

3: Compute updated target bundle parameters $(\boldsymbol{\mu}_y^{\,n+1}, \boldsymbol{\sigma}_y^{\,n+1})$ using Equation 3.8 and Equation 3.11.

4: Compute updated TPS $\mathbf{d}^{n+1}$ $\mathbf{w}^{n+1}$ by solving Equation 3.19.

5: If n<8, go to step 2 and n = n+1, $\lambda = \lambda/10$; otherwise, return $\mathbf{d}^{n+1}$, $\mathbf{w}^{n+1}$ and

$(\boldsymbol{\mu}_{\mathbf{y}}^{n+1}, \boldsymbol{\sigma}_{\mathbf{y}}^{n+1})$.

7. A 2D example

To illustrate the UFIBRE algorithm, we provide a simple 2D example that graphically shows the optimization process of this algorithm. The template contained three fiber bundles, as indicated in Fig. 1a. The target was constructed by rotating the template bundles 30° clockwise. To demonstrate the robustness of the algorithm, an outlier bundle, which did not have a correspondence in the template, was added to the target (see Figure 3.1b). To make the problem more challenging, the outlier bundle was deliberately positioned such that it could be easily misjudged to correspond to the 3rd bundle in the template.

Figure 1

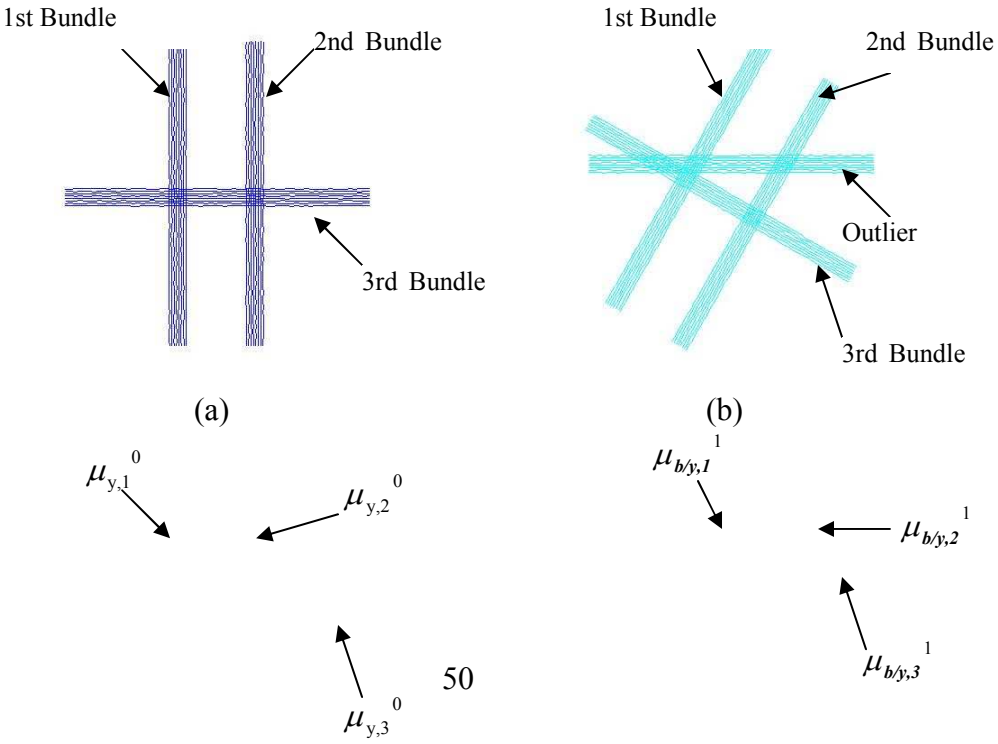

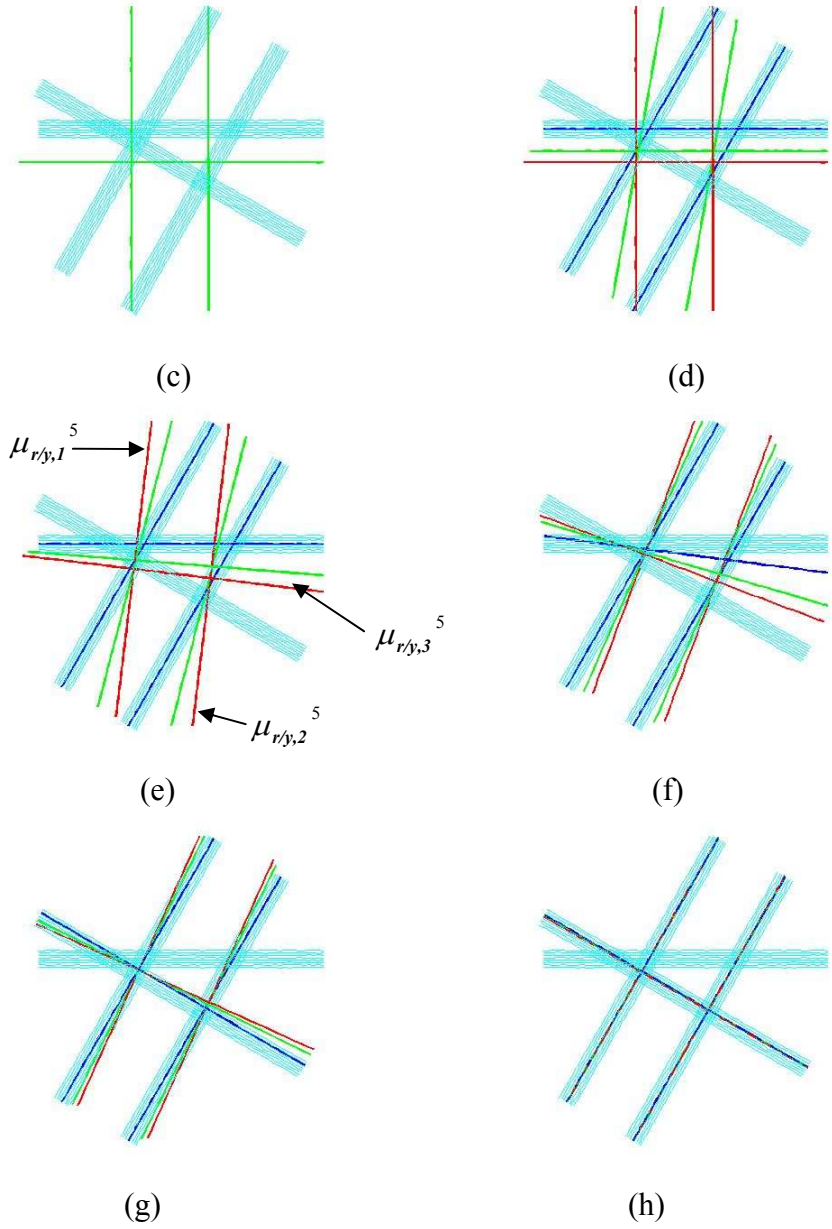

Figure 3.1 Illustrations of the optimization process of the proposed UFIBRE algorithm with a simple 2D example. (a) Template fibers with known bundle classification. (b) Target fibers with unknown bundle classification. The target fibers (cyan), $\mu^{b}{}_{y}{}^{n}$ (blue), $\mu^{r}{}_{y}{}^{n}$ (red) and $\mu_{y}{}^{n}$ (green) at 0th (c), 1st (d), 5th (e), 12th (f), 15th (g), and 20th (h) iteration respectively.

The UFIBRE algorithm was applied to the target as described in the preceding sections. The intermediate and final results of the optimization are illustrated in Figure 3.1 c-h. Each of these figures shows the target fibers (cyan), $\boldsymbol{\mu}_{b/y}^{\ n}$ (blue), $\boldsymbol{\mu}_{r/y}^{\ n}$ (red) and $\boldsymbol{\mu}_{y}^{\ n}$ (green). In this 2D example, *C* was empirically set to 0.5, and a rigid transformation was used.

Figure 3.1c displays the target fibers and $\boldsymbol{\mu}_{\mathrm{y}}^{\ 0}$, which were initialized as the unwarped template central fibers. In the first iteration, $\boldsymbol{\mu}_{\mathrm{y}}^{\ 0}$ was used to compute the membership probability $m_{j,k}^{\ 1}$, which was then used to calculate $\boldsymbol{\mu}_{b/\mathrm{y}}^{\ 1}$. Due to the close proximity to $\boldsymbol{\mu}_{\mathrm{y},3}^{\ 0}$, the outlier target bundle had high membership probability of belonging to the 3rd bundle, resulting in an incorrect $\boldsymbol{\mu}_{b/\mathrm{y},3}^{\ 1}$ as shown in Figure 3.1d. On the other hand, $\boldsymbol{\mu}_{b/\mathrm{y},1}^{\ 1}$ and $\boldsymbol{\mu}_{b/\mathrm{y},2}^{\ 1}$ were correctly determined, leading to more reasonable estimates of $\boldsymbol{\mu}_{\mathrm{y},1}^{\ 1}$ and $\boldsymbol{\mu}_{\mathrm{y},2}^{\ 1}$. In the last step of the first iteration, a rigid transformation was calculated to align the template central fibers with $\boldsymbol{\mu}_{\mathrm{y}}^{\ 1}$. In spite of the incorrect $\boldsymbol{\mu}_{b/\mathrm{y},3}^{\ 1}$, the template fibers were still rotated in a favorable direction as driven by the other two correct target bundles, and thus $\boldsymbol{\mu}_{r/\mathrm{y},3}^{\ n}$ was gradually pulled toward the correct target bundle as shown in Figure 3.1d and e. As the weighted sum of $\boldsymbol{\mu}_{r/\mathrm{y},3}^{\ n}$ and $\boldsymbol{\mu}_{b/\mathrm{y},3}^{\ n}$, $\boldsymbol{\mu}_{\mathrm{y},3}^{\ n}$ was also driven to the correct position by the movement of $\boldsymbol{\mu}_{r/\mathrm{y},3}^{\ n}$ (Figure 3.1d-f). In the 12th iteration, $\boldsymbol{\mu}_{\mathrm{y},3}^{\ n}$ had become quite close to the correct 3rd target bundle and thus generated correct membership probability $m_{j,k}^{\ 12}$ that led to a correct estimation of $\boldsymbol{\mu}_{b/\mathrm{y},3}^{\ 12}$ (Figure 3.1g).

Finally, the warped template bundles converged to the correct target bundles as shown in Figure 3.1h. This example demonstrates that the registration process helps reduce the influence of the outlier so that the target fibers can be bundled consistently with the template.

8. Conclusions and Discussions

In this chapter we proposed a novel algorithm for joint bundling and registration of white matter fibers reconstructed from DTI data (Xu et al., 2009). Given a set of segmented template bundles and a whole-brain target fiber set, the algorithm optimally bundles the target fibers and registers them with those in the template.

The framework we proposed has two salient and mutually beneficial features. First, the registration process guides fibers in the target to converge to bundles that are consistent with the template. This consistency is not guaranteed in conventional fiber clustering algorithms, which exclusively operate on individual datasets separately. Second, the bundling process helps simplify fiber-based registration to bundle-to-bundle registration. This avoids the process of fiber pre-clustering, and considerably improves the computational efficiency.

Image registration as a general image processing problem has long been the interest of many researchers. Essentially, it involves searches in a high dimensional space for transformation parameters that deform one image to optimally match another. The image registration problem, however, is ill-posed since a unique solution may not exist, and has very high computational complexity due to the high dimensional searches needed. The situation is worse for white matter fiber registration, as the structures to be registered are finer and hence more complicated scenarios may occur. To approach the ill-posed,

highly complex problem, it is typical to employ some regularization mechanisms and iterative optimizations, so that practically useful solutions can be obtained.

In this work, we also use regularization and iterative optimization, but further make three assumptions on fiber distributions for WM fiber registration: (1) A set of fibers in the human brain observe a Gaussian mixture model; (2) fibers in a bundle and points along the fibers are identically and independently distributed; and (3) the probability distribution of errors between the central fiber of a target and that of a template is Gaussian. These assumptions offer considerable computational benefits to parameter optimization, which renders the fiber registration problem more tractable. Although the validity of these assumptions still warrants further proof, experiments in this work demonstrate that quite appealing results can be obtained based on them. We recognize, however, more sophisticated models may better describe white matter fiber distributions. For example, it was reported that a Gamma mixture distribution (Maddah et al., 2005) may model the white matter fiber distribution more accurately. Since parameters in the Gamma model can also be estimated by the EM algorithm, it can be in principle incorporated into our framework as well. However, a major drawback of using this or other more sophisticated models is disproportionally increased complication in the parameter optimization. We therefore note that, for fiber registration, the fiber distribution model should be chosen judiciously so that an optimal trade-off between the accuracy of model representation and the efficiency of parameter optimization is achieved.

It should be mentioned that, in this work, alignment of fiber bundles between the template and the target is only based on matching of the first order statistics (central

fibers) of the bundles. The central fiber alone, however, does not carry complete information about the morphology of the fiber bundle. To align two fiber bundles more accurately, higher order statistics need to be considered. For instance, minimizing the difference in the second order statistics (covariance matrices) would provide better matching of bundle cross-sectional profiles. However, using higher order statistics may create difficulties in modeling the conditional probability, $p(\boldsymbol{\mu}_y, \boldsymbol{\sigma}_y, \boldsymbol{\pi}_y \mid \boldsymbol{\mu}_x, \boldsymbol{\sigma}_x, \boldsymbol{\pi}_x)$. A solution to this exists for the second order statistics (i.e., using Kullback Leibler divergence), but optimization of the target bundle parameters becomes too complicated. Therefore, high order statistics are not included in this work, in order to achieve a compromise between the accuracy of bundle alignment and the efficiency of parameter optimization.

A most direct and useful application of joint bundling and registration of white matter fibers is group analysis. It allows fibers from different subjects to be bundled consistently and registered into a common space, in which statistical characterization of bundle structural, architectural or geometric properties can be conveniently implemented. In addition, consistent and co-registered bundles from a group of subjects may be used to construct a parametric bundle atlas, which can be further utilized to guide other processes such as fiber tracking, bundling/labeling and registration. This application has been debuted in the present work with construction of a bundle atlas using eight human datasets. Here we want to point out that the Gaussian variances in atlas bundles are contributed by three factors, registration errors, the inter-subject and the intra-subject variances. The intra-subject variances are related to sizes of fiber bundles, and the inter-subject variances are determined by the structural differences of bundles across subjects.

Any mis-registration in this process would also cause certain level of variances in the atlas bundles.

Finally, we point out that the initial template bundles are segmented manually in this work. As mentioned earlier, this offers great flexibility in selecting or defining the bundles of interest. Notwithstanding this flexibility, the manual initial segmentation has the drawback of potentially producing subjective errors, and involving a certain amount of human labor. Manual segmentation can be avoided by using an atlas that contains well defined bundle models of interest for initialization. We have demonstrated the possibility of constructing an atlas of this kind, and plan to develop a more reliable atlas with more comprehensively defined fiber bundle models from a larger group of subjects, to enable our UFIBRE algorithm to work in a fully automated and objective fashion.

CHAPTER IV

UNIFIED FIBER BUNDLING AND REGISTRATION: EVALUATIONS

The goal of this chapter is to evaluate the proposed UFIBRE algorithm with a set of carefully designed and conducted experiments.

1. Experiment and evaluation methods

A. Imaging

The UFIBRE algorithm was applied to *in vivo* DWI data obtained from eight healthy human subjects. Prior to imaging, informed consent was given by the subject according to a protocol that was approved by the local ethics committee. The data were acquired in vivo using a 3T Philips Achieva MR scanner with 32 non-collinear weighting directions ($b = 1000$ s/mm^2), which generated a volume of $256\times256\times120$ mm^3 at an isotropic resolution of $2\times2\times2$ mm^3 for each subject. Three repeated scans were obtained from each subject, which were motion and distortion corrected and then averaged using Philips diffusion registration PRIDE tool (Release 0.4). Diffusion tensors were estimated from the averaged DWI data using a linear least-square fitting procedure.

B. Fiber reconstruction

To generate the WM fibers, we employed a first order Euler integration method (Basser et al., 2000). The voxels whose FA was greater than 0.5 were selected as seed points, from which the fibers were reconstructed by sequentially following the local principal

diffusion direction at a step size of 2mm. The fiber tracking process was terminated when voxels with FA below 0.1 were met or the angle between the principal diffusion directions of two consecutive points exceeded 45°. The above procedure yielded around 15,000 fibers for each dataset.

C. Bundle selection

Nine WM fiber bundles of interest were manually segmented for each of the eight subjects by referring to their known anatomy. These bundles include the left and right corticospinal tracts (CST), the left and right medial lemniscus (ML), the left and right superior cerebellar peduncle (SCP), middle cerebellar peduncle (MCP) and the lower half of the splenium (SCC) and genu bundle (GCC), respectively. The bundle set from one subject was arbitrarily selected as the template fiber bundle, and Gaussian statistics $(\mu_{x,k}, \sigma_{x,k}, k = 1,...,9)$ of the bundles were calculated.

D. Performance evaluation

With the template, the proposed UFIBRE algorithms were applied to the remaining seven target fiber sets individually. The resulting bundles were compared with the manually segmented target bundles, which served as the "ground truth" in this comparison.

Since our algorithm achieves joint bundling and registration, the performance was evaluated by (1) the consistency of the estimated bundles with the ground truth, and (2) registration errors between their central fibers. Let $\mathbf{b}_k, \overline{\mathbf{b}_k}$ be the estimated and the ground truth fiber bundles respectively and $\boldsymbol{\mu}_k, \overline{\boldsymbol{\mu}_k}$ be their central fibers ($k \in \{1,..,9\}$). The consistency for bundle k is measured by the Dice's coefficient (Dice, 1945):

$$PCC_k = \frac{|\overline{\mathbf{b}_k} \cap \mathbf{b}_k|}{(|\mathbf{b}_k| + |\overline{\mathbf{b}_k}|)/2} \times 100\%, \quad (4.1a)$$

where $|\bullet|$ denotes the cardinality, i.e., the number of fibers in a bundle, and $\cap$ represents the intersection of two fiber bundles. The bundle registration error is measured by the root mean squared error (RMSE) between the central fibers $\boldsymbol{\mu}_k$ and $\overline{\boldsymbol{\mu}_k}$ ($k \in \{1,..,9\}$), which is defined as:

$$RMSE_k = \sqrt{\sum_{i=1}^{N_k} (\boldsymbol{\mu}_{k,i} - \overline{\boldsymbol{\mu}_{k,i}})^2 / N_k}\ . \quad (4.1b)$$

To comprehensively evaluate the proposed algorithm, we used a variety of parameter settings and tested the following aspects:

1) Effect of the parameter C: To see how the weighting factor *C* affects the performance, we evaluated the UFIBRE algorithm with different values of *C* ranging from zero to one. The mean overall Dice's coefficient and RMSE were presented as functions of *C* in order to find an optimal *C* that yields the best overall performance. Here the overall Dice's coefficient and RMSE were calculated for each subject by averaging them across the nine bundles. Their means across seven subjects were further computed for each value of *C*.

2) Optimal performance: To examine the performance of the algorithm with the optimal *C*, we reported the bundle specific mean Dice's coefficient and RMSE instead of overall Dice's coefficient and RMSE. To give a sense of the original differences between the template and target spaces, the RMSE between template central fibers and $\overline{\boldsymbol{\mu}_k}$ were also given ("Un-registered" in Table 2). With this information, one can see the effect of the UFIBRE algorithm on *in vivo* datasets. In addition to the quantitative evaluation, the resulting fiber bundles were also assessed visually.

3) Effect of the number of bundles used: The above experiments were based on the use of the nine fiber bundles chosen (the left and right CST, the left and right ML, the left and right SCP, MCP, SCC and GCC). To test the effect of the number of bundles on the performance, we excluded some bundles from the experiments. The bundle specific mean Dice's coefficient and RMSE were reported for the case when ML and SCP were excluded and also for the case when MCP was excluded.

4) Consistency of factional anisotropy (FA): To examine the consistency of diffusion parameters between the fiber bundles from the UFIBRE algorithm and those from manual segmentation, we performed group comparisons of the FA values along the nine fiber bundles studied. Let $\mathbf{b}_{k,j,i}$ and $\overline{\mathbf{b}}_{k,j,i}$ be the ith point at the jth fiber in the kth bundle from implementation of the UFIBRE algorithm and the manual segmentation respectively. The mean FA value along the kth bundle $F_{k,i}$ $\overline{F}_{k,i}$ can then be computed for each subject as follows,

$$F_{k,i} = \frac{\sum_j \mathbf{FA}(\mathbf{b}_{k,j,i})}{|\mathbf{b}_k|},$$

$$\overline{F}_{k,i} = \frac{\sum_j \mathbf{FA}(\overline{\mathbf{b}}_{k,j,i})}{|\overline{\mathbf{b}}_k|},$$

where **FA**(**a**) denotes the FA value at the position **a** in DTI data, and $|\bullet|$ denotes the cardinality. Treating $F_{k,i}$ and $\overline{F}_{k,i}$ as two random variables whose values for each subject as samples from their probability distributions, we statistically compared $F_{k,i}$ with $\overline{F}_{k,i}$ to see whether there are significant differences between the diffusion measurement resulting from the UFIBRE algorithm and that of manually segmented bundles. Paired t-tests were

used to test the group difference along the fiber bundles, with each group containing the seven subjects studied.

5) Convergence: To analyze the convergence, the overall RMSE between the estimated central fibers $\boldsymbol{\mu}_y^n$ and manual segmentations were recorded for each of the 15 iterations.

E. Atlas construction

The bundle correspondence and transformation information from the UFIBRE algorithm can be readily used to construct a fiber bundle atlas, which can serve as a statistical template for many purposes, such as guiding fiber tracking or bundle segmentation. To demonstrate the use of this algorithm for atlas construction, all the seven target datasets were transformed into the template coordinate system using the inverse of the transformation T previously obtained; then the corresponding bundles, which had already been estimated by the algorithm, were combined to construct a bundle atlas on the basis of the seven target and the template fiber sets. The statistics (central fiber and model covariance) of each bundle in the atlas were subsequently computed.

2. Results

A. Performance evaluations

1) Effect of the parameter C: Figure 4.1 shows that the UFIBRE algorithm achieves an optimal performance (maximum Dice's coefficient and minimum RMSE) at $C = 0.5$. This indicates that the algorithm works best when the bundling term $\boldsymbol{\mu}_{b/\mathrm{y}}{}^n$ and registration term $\boldsymbol{\mu}_{r/\mathrm{y}}{}^n$ contribute equally to $\boldsymbol{\mu}_{\mathrm{y}}{}^n$ (Equation 3.10). Therefore, C is set to 0.5 for all the following studies.

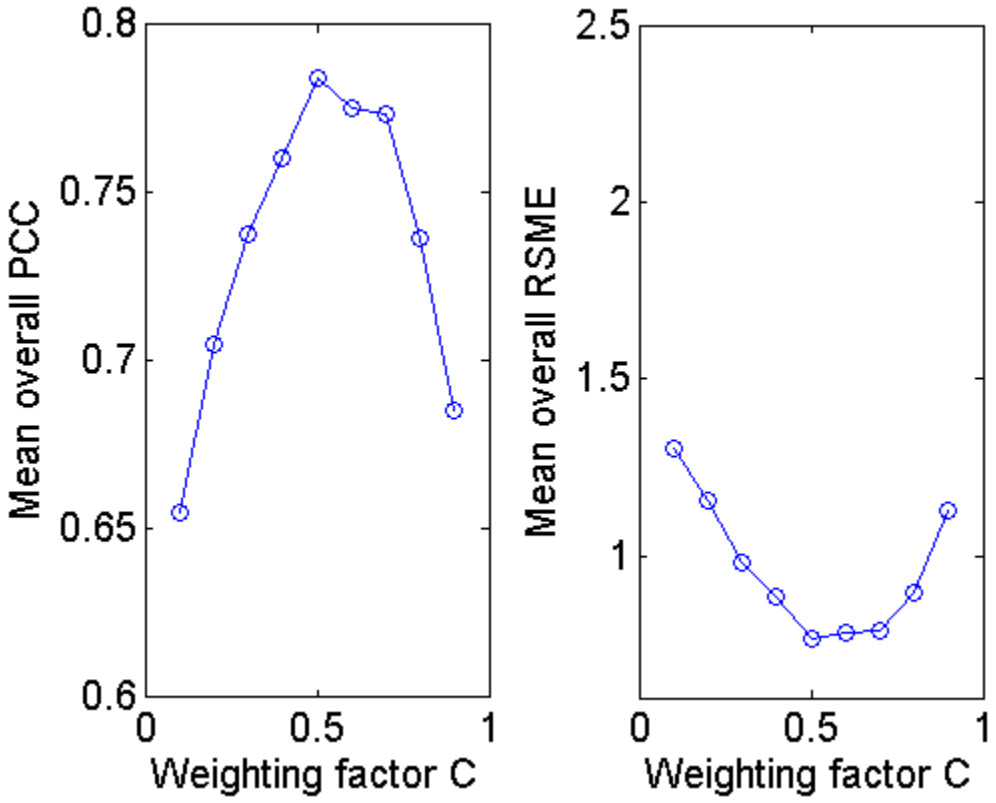

Figure 4.1 Variations of the mean overall Dice's coefficient and RMSE with respect to the weighting factor *C*.

2) Optimal performance: Table 1 and 2 show the statistics of Dice's coefficient and RMSE respectively for each of the fiber bundles studied. From the second and third columns in Table 4.1, it can be seen that the estimated CST, MCP, SCC and GCC achieve an overall consistency of 85% Dice's coefficient (minimum: 79%, maximum: 94% Dice's coefficient) with the manually segmented bundles. From the fourth and fifth columns in Table 4.2, it can also be seen that all the bundles give a very small average RMSE (less than 1 voxel) except the ML and SCP, whose average RMSEs are slightly greater than 1 voxel. These results indicate that our algorithm is capable of segmenting most of target bundles at a sub-voxel accuracy. The relative smaller Dice's coefficients

and larger average RMSEs in ML and SCP may be attributable to two factors. First, the fibers of the ML and SCP mutually overlap for a significant distance, which makes them rather difficult to distinguish for both the UFIBRE algorithm and manual segmentation. Second, there is considerable variability among the individual subjects in the course and size of the ML and SCP. Such variability contributes significantly to the difference between the template and the target data.

Table 4.1 Statistics of Dice's coefficient for nine fiber bundles over the seven subjects using the UFIBRE with $C = 0.5$.

	No bundles excluded		ML, SCP excluded	MCP excluded
	Mean	Std	Mean	Mean
CST(Left)	0.8862	0.1091	0.718	0.8611
CST(Right)	0.7898	0.1114	0.7175	0.7948
ML(Left)	0.6936	0.2831	N/A	0.6924
ML(Right)	0.6383	0.3420	N/A	0.6049
SCP(Left)	0.6931	0.2786	N/A	0.6652
SCP(Right)	0.6553	0.2933	N/A	0.6560
MCP	0.9366	0.0718	0.9320	N/A
SCC	0.9000	0.0624	0.8955	0.8968
GCC	0.8632	0.0760	0.8492	0.8593

Table 4.2 Statistics of RMSE for nine fiber bundles over the seven subjects using the UFIBRE with C = 0.5. (unit: voxel)

	Un-registered		Registered			
			No bundles excluded		ML, SCP excluded	MCP excluded
	Mean	Std	Mean	Std	Mean	Mean
CST(Left)	2.8145	0.6231	0.2315	0.2901	0.3048	0.3243
CST(Right)	4.1739	1.1585	0.6064	0.3384	0.8357	0.5831
ML(Left)	3.9206	1.3966	1.0983	0.9406	N/A	1.0961
ML(Right)	4.3691	0.3160	1.1823	1.1128	N/A	1.4149
SCP(Left)	3.3592	1.1830	1.0400	1.2057	N/A	1.1201
SCP(Right)	5.5162	1.6030	1.0033	0.7939	N/A	1.0352
MCP	4.8298	2.0292	0.2212	0.2632	0.2696	N/A
SCC	4.1748	1.2064	0.7514	0.3495	0.7883	0.7621
GCC	3.9300	1.4934	0.7465	0.3571	0.7913	0.7515

To demonstrate the capability of the algorithm for joint bundling and registration, estimated bundles in one of the seven target datasets were superimposed onto the template bundles, as shown in Figure 4.2. In Figure 4.2a, the CST, ML and SCP bundles of the template (red) and the target fiber (blue) set are overlaid on one coronal (top row) and sagittal (bottom row) slice of the target FA map. Note that the blue bundles, which were found by the UFIBRE algorithm, exhibit gross similarity to the manually segmented template bundles with respect to bundle structures and shapes. This indicates that our algorithm is able to bundle the target fibers in a way consistent with the template bundles. The left column of Figure 4.2a displays the target bundles and un-registered template

bundles, which shows obvious differences in the location and course between them due to differences in subject brain morphology, scan positions and orientations. The right column shows the results of registering the template bundles with the target, in which it can be seen that the post-registered template bundles overlap well with the target fibers. There is noticeable mismatch between the boundaries of the post-registered and target SCP, because the algorithm only registers their central fibers and thus does not guarantee the match of the whole bundles. Figure 4.2 b-c respectively displays the MCP (b), SCC and GCC (c) bundles for template and target fibers overlaid on a transverse (top row) and sagittal (bottom row) view of the target FA map. We can also see increased similarity in the location and course for the post-registered template bundles.

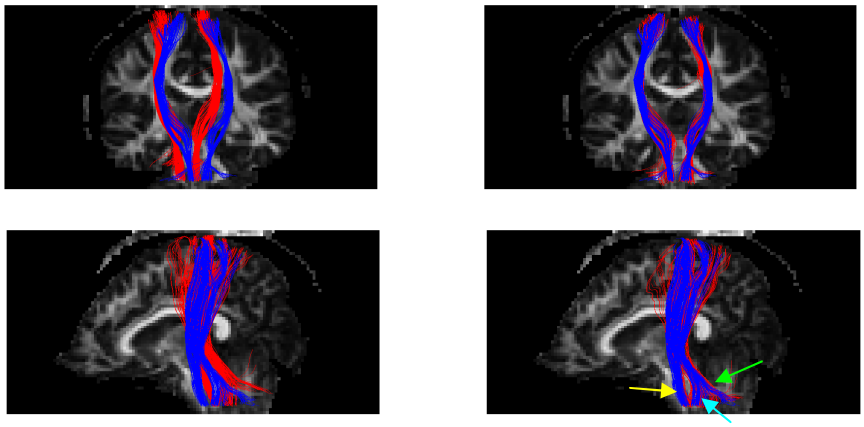

(a)

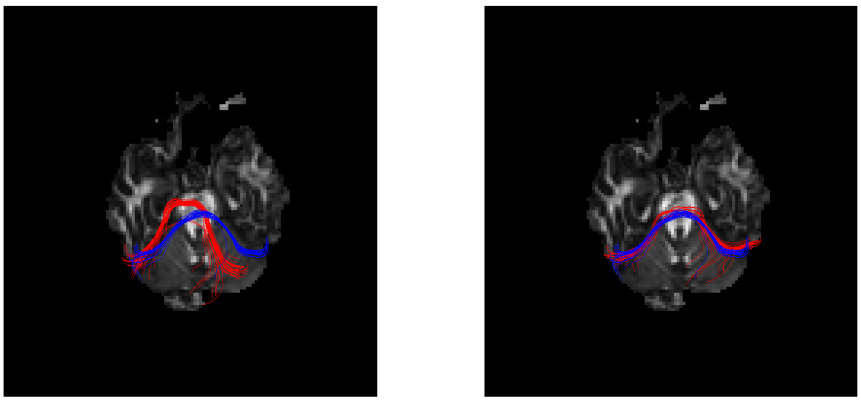

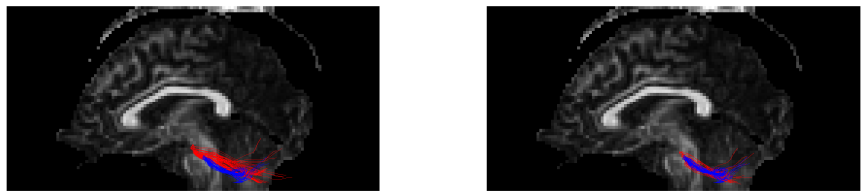

(b)

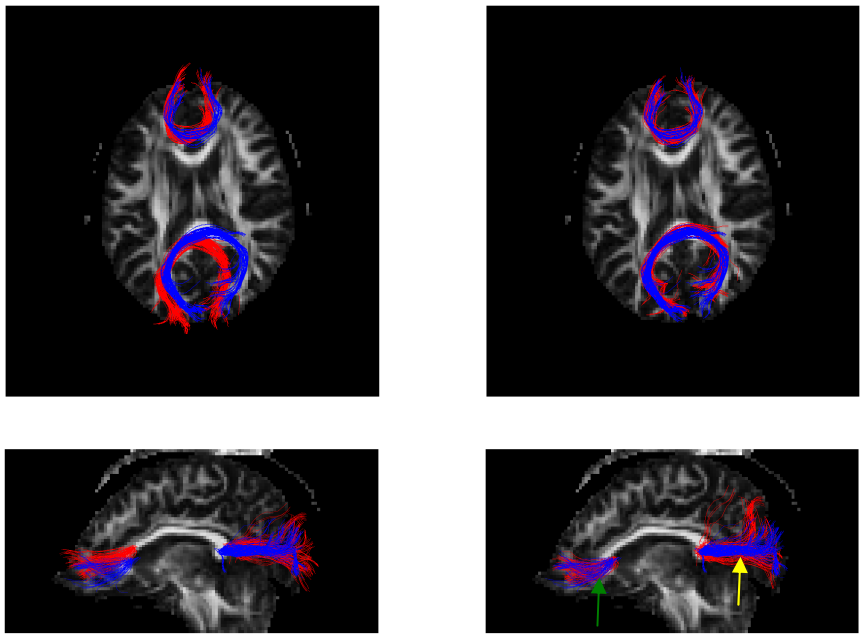

(c)

Figure 4.2 Superimposition of the template (red) and target fiber (blue) bundles on the FA map of the target data. The left column displays the unregistered template bundles with the target bundles, and the right column shows the registered and warped template bundles with the same target bundles. (a) CST (yellow arrow), ML (cyan arrow) and SCP (green arrow) bundles in coronal (top row) and sagittal (bottom row) views. (b) MCP bundle in transverse (top row) and sagittal (bottom row) views. (c) SCC (yellow arrow) and GCC (green arrow) bundles in transverse (top row) and sagittal (bottom row) views.

The estimated target bundles for a typical case were visually compared with manual segmentation in Figure 4.3. In this figure, the first and third columns (red) are the fiber bundles estimated by the UFIBRE algorithm and the second and fourth columns (blue) are the bundles from manual segmentation. Note that the saggital view only displays the left CST, ML and SCP to avoid overlap with their right homologues. It can be appreciated that, for all structures, the courses and positions of the estimated target bundles are quite consistent with those from manual segmentation (blue).

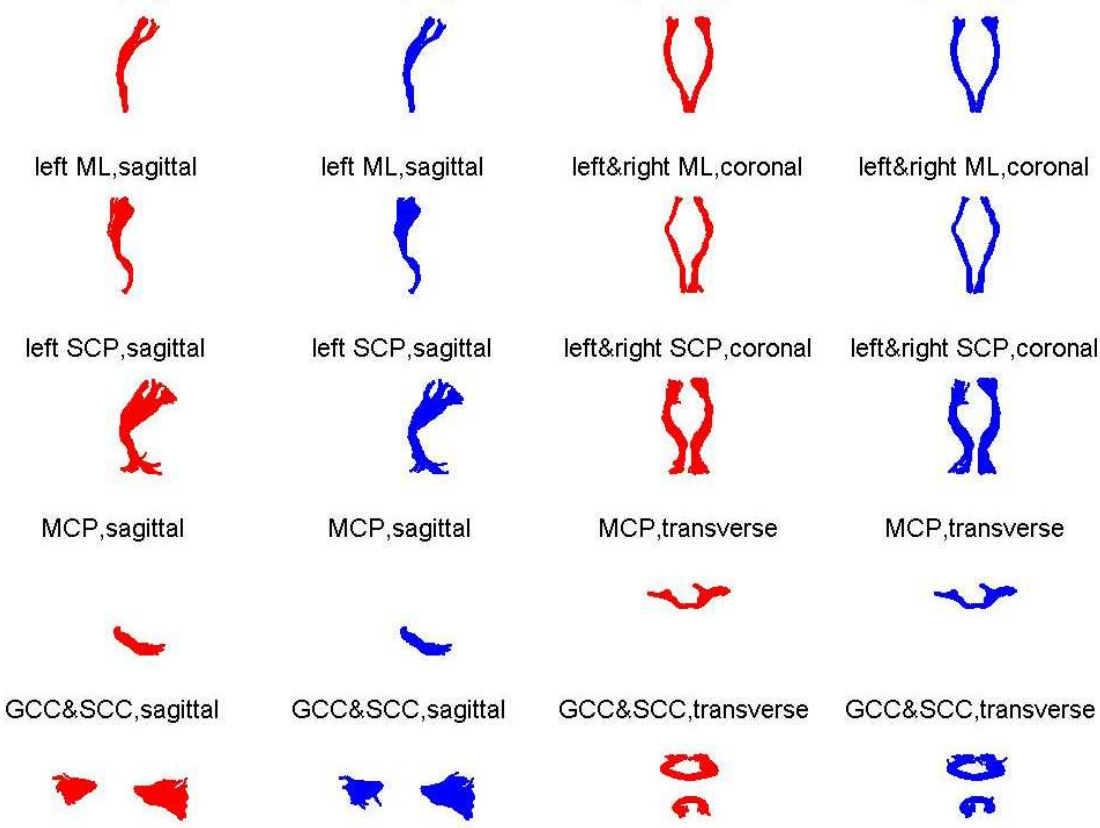

Figure 4.3 Comparisons between ground truth obtained by manual segmentation (blue) and the bundles estimated by the UFIBRE algorithm (red) for one typical dataset.

3) Effect of the number of bundles used: Table 4.1 and 4.2 also show the resulting Dice's coefficient and RMSE when some fiber bundles were excluded from the nine template bundle models. Comparing the 3th with the 1st column in Table 4.1 and the 5th with the 3th column in Table 4.2, it can be seen that the Dice's coefficients and RMSEs with MCP excluded are very comparable to those with all the nine bundles used (with generally a slightly worse performance when MCP was excluded). With ML and SCP excluded, it can be found that the Dice's coefficients (the 4th column in Table 4.1) and RMSEs (the 6th column in Table 4.1) of the CST deteriorate greatly due to the fact that the ML and SCP fibers are close and similar to the CST fibers, which leads to incorrect classification of some ML and SCP fibers as CST by the algorithm. On the other hand, the performance for MCP, SCC and GCC bundles only decreases slightly when ML and SCP were excluded. These observations indicate that including more bundles in the registration improves the performance of registering bundles in their vicinity, but the effect is very small on remote fiber bundles.

4) Consistency of factional anisotropy (FA): Figure 4.4 shows the group mean and standard deviation of F and $\overline{F}$ together with the p value of their paired t-tests along the nine fiber bundles studied. Comparing the first and second columns, it can be seen the curves of F 's and $\overline{F}$'s group mean along the bundles are quite similar. Rigorous paired t-tests between F and $\overline{F}$ show that there are no statistically significant differences between them along any of the bundles (the third column) at p=0.05 level, as all the p-values are greater than 0.2 and ~90% of them are even greater than 0.5. Of particular notes, the ML and SCP bundles exhibit relatively smaller p-values than the other bundles; this is

consistent with earlier observations that the Dice's coefficient and RMSE of these two bundles are worse than others.

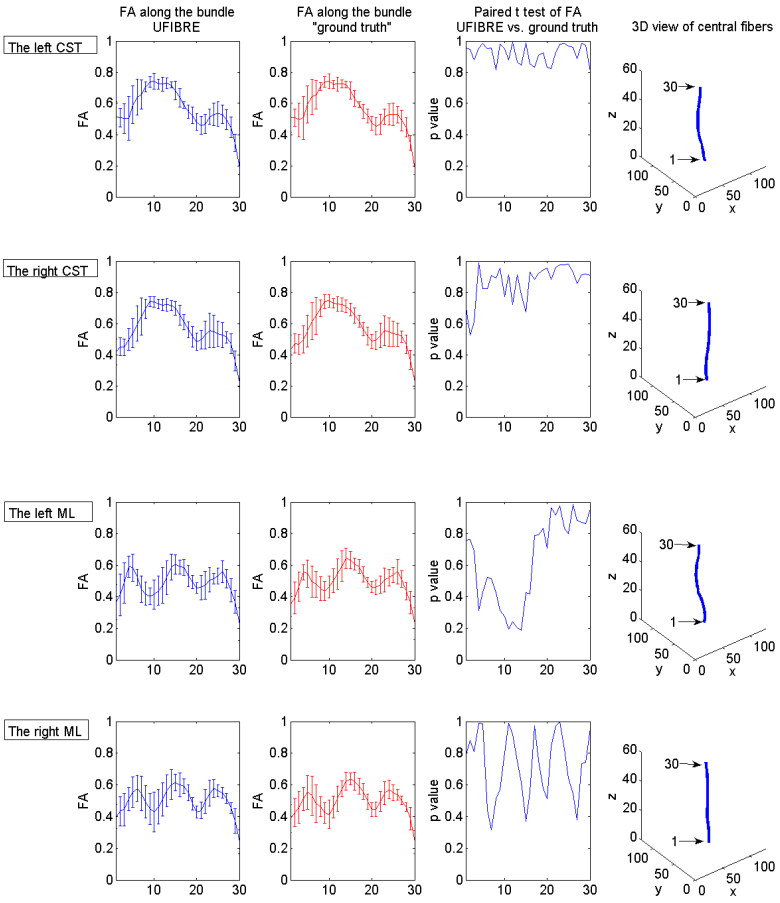

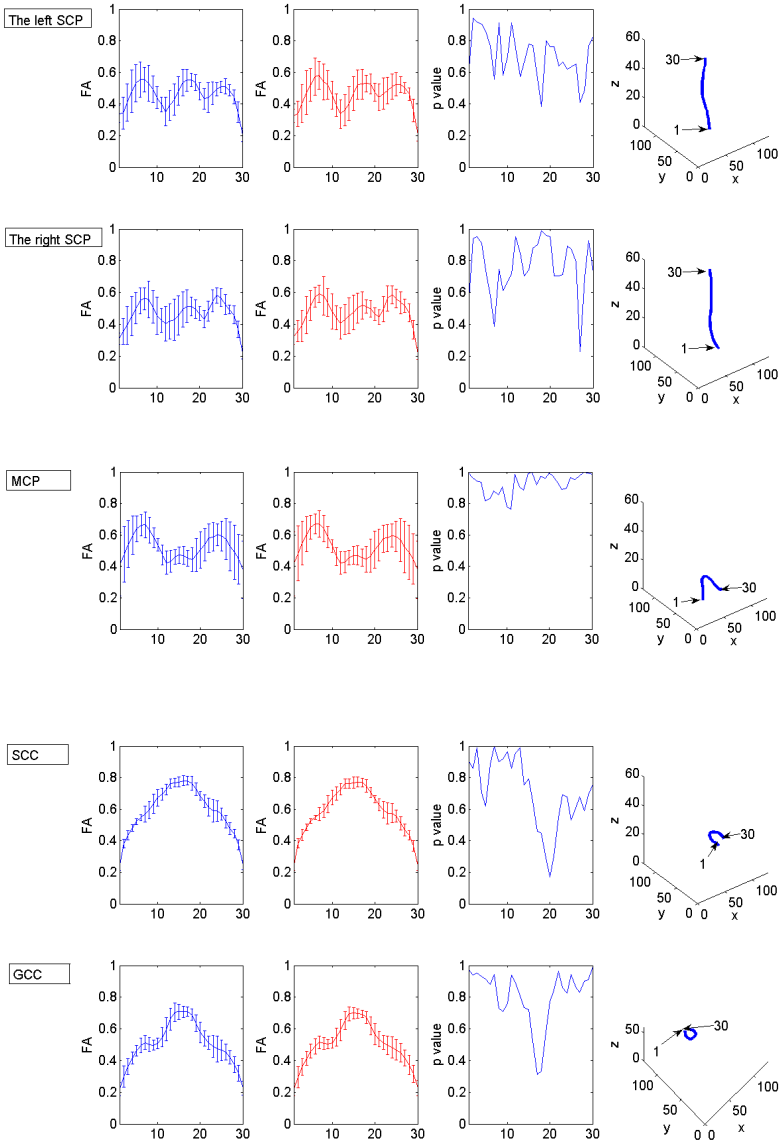

Figure 4.4 Comparisons between F and $\overline{F}$ along bundles. The curve in the first column shows the group mean F with its standard deviation as error bars. Similarly the second column shows the group mean and standard deviation of $\overline{F}$. The p-values of paired t-tests of F and $\overline{F}$ are plotted in the third column. The last column shows the locations of the proximal and distal ends of each of the fiber bundles studied.

5) Convergence: Starting from a significantly large value (~4 voxels), the overall RMSE stabilizes at a small value (less than 1 voxel) after 13 iterations. This indicates that 15 iterations are sufficient for the UFIBRE algorithm to achieve convergence.

6) Computational complexity: In our experiments, there are a total of 1000 fibers approximately in the template bundles (~100 in each of the SCP, the MCP, the ML and the CST; ~500 in the SCC and the GCC). The number of fibers in one target dataset is usually around 15,000. Each fiber was downsampled to 30 discrete points. It takes up to 15 iterations at ~60 seconds per iteration for our Matlab implementation to complete bundling and registering a whole target fiber set with the nine template bundles on an AMD Athlon 64X2 Dual-Core processor.

B. WM fiber atlas construction

The atlas bundles were constructed by combining the fibers from the corresponding bundles in the eight datasets. The calculated central fibers and covariance $(\mu_{x,k}, \sigma_{x,k}, k = 1,2,...9)$ of the atlas bundles are graphically displayed in a 3D view in Figure 4.5. At each point along the central fiber, the covariance matrix is represented by an ellipsoid. The orientations of the three axes of the ellipsoid are the same as the eigenvectors of the covariance matrix, and the lengths of the axis are equal to the square roots of the eigenvalues of the corresponding eigenvectors respectively. The ellipsoid at each central fiber point describes the distribution of all the points that belong to the same bundle and has correspondence to the central fiber point. It can be seen that the middle portion of the bundles have smaller ellipsoids or tighter distributions of points, and the ellipsoids tend to become larger towards to the ends of the bundles. In particular, the

ellipsoids at the ends of some of the bundles (MCP, SCC and GCC) sharply expanded. The compact middle portion indicates that the target bundles have been reasonably well-registered with the template. The gradually increasing covariance towards the ends is largely attributable to divergent nature of WM fiber bundles as they approach cortical regions and also partly due to accumulative errors that may occur in fiber tracking. The sudden increase of covariance at the ends suggests the tensors and thus the derived fiber tracts are less reliable near the cortical regions, where the FA is typically quite low.

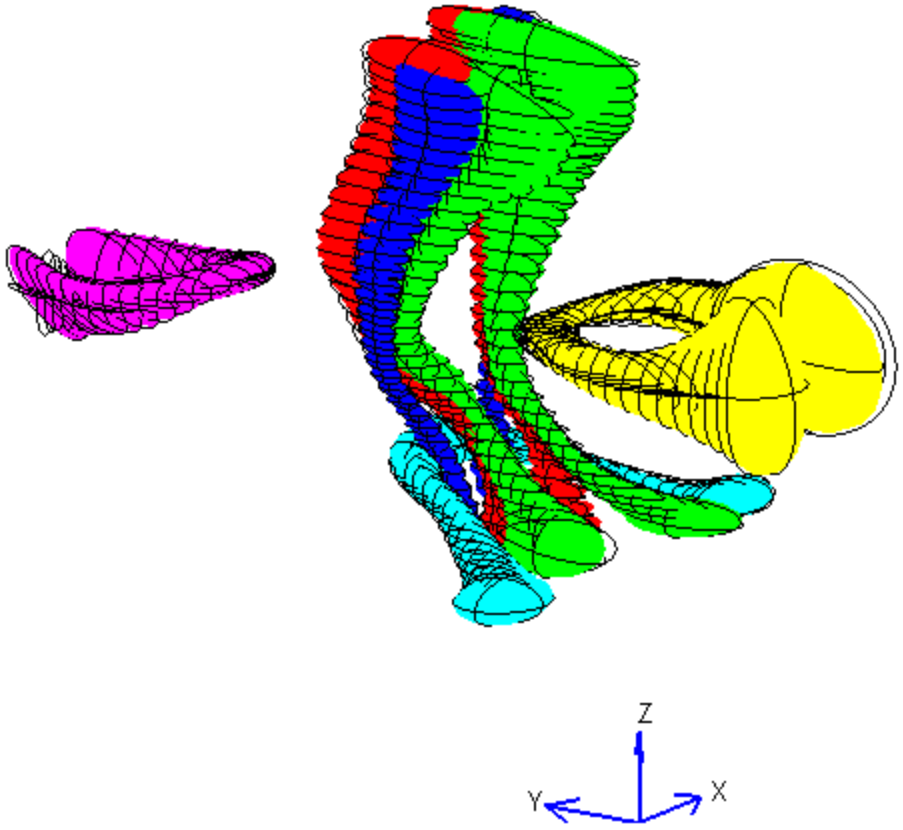

Figure 4.5 A 3D view of the constructed bundle atlas from the template and seven target datasets (Red: the CST, Green: the ML, Blue: the SCP, Cyan: the MCP, Yellow: the SCC, Magenta: the GCC).

3. Conclusions

Experiments with *in vivo* data demonstrate that the bundles estimated by the UFIBRE algorithm have an ~80% consistency with ground truth and the root mean square error between their bundle medial axes is less than one voxel (Xu et al., 2009). The proposed algorithm is highly efficient, offering potential routine use for group analysis of white matter fibers.

CHAPTER V

GREY MATTER PARCELLATION CONSTRAINED FULL BRAIN BUNDLING

In the previous two chapters, several major white matter fiber pathways are automatically segmented and aligned across subjects using the proposed UFIBRE algorithm. Group comparison of these resulting bundles can reveal possible structural abnormalities for certain neurological and psychiatric disorders, e.g. multiple sclerosis, schizophrenia, and so on. In this chapter, the goal is to automatically group a full brain fiber set into bundles that connect cortical/sub-cortical basic units, which can help us understand the structural architecture of the neural network (Gong et al., 2008). However, the UFIBRE algorithm can't be applied to this scenario, as it is fairly difficult to construct such a full brain bundle template due to challenges in cortex parcellation.

The contribution of this work is to solve the challenging problem by proposing an automatic clustering algorithm that leverages Montreal Neurological Institute (MNI) T1 template to bundle a full brain fiber set into connections between cortical/sub-cortical basic units.

1. Introduction

To date there is a plethora of bundling algorithms that have been proposed and applied to DTI, including mainly three types of methods, manual bundling (Stieltjes et al., 2001; Wakana et al., 2004; Catani et al. 2002), clustering-based (Ding et al., 2003; O'Donnell et

al. 2005, 2006b; Maddah et al., 2006, 2007a, 2007b, 2008; Zhang et al., 2002, 2005, 2006, 2008; Moberts et al., 2005; Corouge et al., 2004; Brun et al., 2003, 2004; Shimony et al., 2002) and atlas-based bundling (Zhang et al., 2007; Maddah et al., 2005; O'Donnell et al. 2006a, 2007; Xia et al., 2005). However, few of these algorithms are capable of generating a full brain cortical/sub-cortical connection network due to their own limitations.

Manual bundling procedures group fibers based on a set of manually placed regions of interest (ROIs) that they pass (Stieltjes et al., 2001; Wakana et al., 2004; Catani et al. 2002). Performance of such a bundling relies significantly on the accuracy of manual segmentation of these ROIs. However, in some cases it is difficult to achieve an accurate segmentation of desired ROIs, particularly the basic units of brain cortex. Furthermore, the manual parcellation process is fairly time-consuming and suffers from inter- and intra- operators' errors.

To gain an efficient definition of ROIs, bundling approaches based on an atlas/template with pre-defined ROIs has been proposed (Zhang et al., 2007; Maddah et al., 2005; O'Donnell et al. 2006a, 2007; Xia et al., 2005). Firstly, an atlas/template brain is manually partitioned into a set of anatomic ROIs, e.g., corpus callosum, thalamus, and a fine-grained parcellation of cortex. The atlas/template images, e.g. T2 weighted MR image, and fractional anisotropy (FA) map, are registered with a target image of the same modality, which shall be in the same space of DTI fibers. The transformation output by registration is then used to warp the pre-defined atlas/template ROI masks to DTI fiber space. Finally, fibers are grouped based on these transformed ROIs in a manner similar to manual bundling. Unfortunately it is well known that registration is particularly prone to

errors in grey matter due to poor image contrast and fairly complex structures therein, which renders transformed ROIs to be an unreliable basis for fiber bundling. This problem may lead to questionable incoherent fiber bundles.

In parallel to atlas-based and manual approaches, there is a rich literature of computer clustering based bundling methods (Ding et al., 2003; O'Donnell et al. 2005, 2006b; Maddah et al., 2006, 2007a, 2007b, 2008; Zhang et al., 2002, 2005, 2006, 2008; Moberts et al., 2005; Corouge et al., 2004; Brun et al., 2003, 2004; Shimony et al., 2002). With no reliance on ROI definitions, these methods usually generate bundles by grouping fibers with similar geometrical properties, such as shapes, locations, and other attributes. While these algorithms have been used to yield a coherent full brain bundle set in an efficient and automatic manner, they do not have inherent reference to a brain anatomy and hence the resulting bundles would often lack anatomical interpretations, not to mention a cortical/sub-cortical connection network.

To achieve a both coherent and anatomically consistent fiber bundling, a novel clustering framework is proposed to combine the clustering- and template-based bundling approach. In this algorithmic framework, the fiber clustering is constrained with a brain parcellation or a set of ROIs, which is transformed to fiber space by registration. The clustering portion in the algorithm serves to preserve the bundling coherence while the ROI constrain forces anatomical correspondence on resulting bundles.

2. Methods

Let $\mathbf{r}$ denote an end point of fiber $\mathbf{x}$. Given an atlas, whose grey matter has already been divided into a set of cortical/sub-cortical ROIs, a registration algorithm maps the ROI

labels from the atlas to the subject space. Therefore, for each voxel in the subject space, there is an associated ROI label $l = 0,1,....L$. When registration and fiber tracking is perfect and thus $\mathbf{r}$ and $l(\boldsymbol{r})$ represents the true coordinate and ROI label, $\mathbf{x}$ can be classified as a fiber connecting $l(\mathbf{r1})$ and $l(\mathbf{r2})$, where $\mathbf{r1}$ and $\mathbf{r2}$ denote the starting and the end point respectively.

A. Uncertainties

However, the two measurements $\mathbf{r}$ and $l(\mathbf{r})$ are observations corrupted with a certain level of noises.

The uncertainties of $l(\mathbf{r})$ is caused by the fact that image registration is in particular prone to errors in cortex due to several reasons: (1) the poor MR imaging contrast in grey matter makes it difficult to differentiate different cortical regions; (2) cortical structures are fairly complex and inconsistent across subjects so that image registration can't accurately deform an atlas to match an arbitrary subject; (3) imaging noises and distortions make the measured intensity values less likely represent the true underlying tissue properties.

On the other hand, it is difficult to accurately reconstruct neural fibers, particularly their end points $\mathbf{r}$, which play important roles in determining what ROIs fibers connect. Due to the use of single-shot echo-planar imaging sequences, the DTI usually have poor signal-to-noises ratio (SNR). In another word, estimated tensors quite often don't reflect correct underlying fiber orientations. This problem becomes even worse near the grey matter due to its low anisotropy, where a small amount of noises could impact the measured tensors significantly. As fiber tracking algorithms use the principal diffusion

directions of tensors to induce fiber orientations, noisesd tensor measurements would cause incorrect fibers to be generated. Moreover, as the orientation errors could be cumulated in a fiber tracking process, the two end points of a fiber might deviate most from the true positions.

B. Cortex projection model

The likelihood of $\mathbf{r}$ falling into ROI l can be expressed as follows,

$$p(l \mid \mathbf{r}) = (2\pi\sigma^2)^{-3/2} \exp(-\frac{(\mathbf{v}(l,\mathbf{r}) - \mathbf{r})^T (\mathbf{v}(l,\mathbf{r}) - \mathbf{r})}{2\sigma^2}), \quad (5.1)$$

where $\mathbf{v}(l,\mathbf{r})$ is the point closest to $\mathbf{r}$ in the ROI l. The proposed model projects the starting and the end point into their closest points in cortical/sub-cortical regions and uses their distances to model the end-to-ROI probability. The isotropic variance σ is a parameter related to the magnitude of registration and fiber tracking errors. When registration and fiber tracking is accurate, σ can be set to a small value, which makes the end point $\mathbf{r}$ unable to deviate much from its true ROI. In the case of poor registration and fiber tracking, a large σ shall be used, which assumes that end point $\mathbf{r}$ can be far away from its true ROI.

To compute the probability $p(l \mid \mathbf{r})$ in Equation 5.1, the distance transform of ROI l is pre-computed, yielding an image volume $\phi_l(\bullet)$. Therefore, $p(l \mid \mathbf{r})$ can be expressed as follows,

$$p(l \mid \boldsymbol{r}) = (2\pi\sigma^2)^{-3/2} \exp(-\frac{(\phi_l(\boldsymbol{r}))^2}{2\sigma^2}). \quad (5.2)$$

With this formula, evaluation of $p(l \mid \mathbf{r})$ doesn't require a search for $\mathbf{r}$'s closest point in ROI l and only needs a constant-time lookup for value $\phi_l(\mathbf{r})$.

C. Cortex projection bundle model

A Gaussian model may be chosen to represent the distribution of fibers inside a bundle for simplicity and efficiency. With further assumption of point independence, the probability of a fiber $\mathbf{x}$ belonging to the bundle connecting $l1$ and $l2$ can be expressed as below,

$$p(\mathbf{x} \mid \boldsymbol{\mu}_{l1,l2}, \sigma_{l1,l2}) = \prod_{i=1}^{m} (2\pi\sigma_{l1,l2}{}^2)^{-3/2} \exp\left(-\frac{(\mathbf{x}_i - \boldsymbol{\mu}_{i,l1,l2})^T (\mathbf{x}_i - \boldsymbol{\mu}_{i,l1,l2})}{2\sigma_{l1,l2}^2}\right), \quad (5.3)$$

where i indexes point on the fiber and $\boldsymbol{\mu}_{l1,l2}$ is the medial axis of bundle $(l1, l2)$. Here an isotropic variance $\sigma_{l1,l2}$ is used for all points, as there are some bundles containing a small number of fibers, which makes the computation of point-specific covariance and its inverse matrix unstable.

Using a clustering solely based on this Gaussian model, fibers with similar shapes and locations would be grouped into a bundle without considering the pair of ROIs that they connect. To incorporate the cortex parcellation information, the two end points of a fiber are projected into specific cortical/sub-cortical areas. For a fiber $\mathbf{x}$, whose two end points are denoted as $\mathbf{r1}$ and $\mathbf{r2}$ respectively, the likelihood of $\mathbf{x}$ being in bundle $(l1, l2)$ can be expressed as follows,

$$p(\mathbf{x} \mid l1, l2) = p(\mathbf{x} \mid \boldsymbol{\mu}_{l1,l2}, \sigma_{l1,l2}) p(l1, l2 \mid \mathbf{r1}, \mathbf{r2}), \quad (5.4)$$

where

$$p(l1, l2 \mid \mathbf{r1}, \mathbf{r2})$$
$$= \max(p(l1 \mid \mathbf{r1})p(l2 \mid \mathbf{r2}), p(l2 \mid \mathbf{r1})p(l1 \mid \mathbf{r2}))$$

Note that the correspondences between $\mathbf{r1}$, $\mathbf{r2}$ and $l1, l2$ are chosen to be the one yielding bigger overall likelihood, which is evaluated with the Equation 5.2. The above metric makes no difference on different permutations of $l1, l2$.

With the bundle model Equation 5.4, similarities of fiber shapes and locations are not the only factors that affect the bundle that a fiber is assigned to. A fiber $\mathbf{x}$ is assigned to a bundle $(l1, l2)$ only if this fiber exhibits high similarity to the majority of fibers in this bundle and its end points $\mathbf{r1}$ and $\mathbf{r2}$ are sufficiently close to $l1$ and $l2$. On the contrary, a fiber that ends exactly in $l1$ and $l2$ may still be excluded from bundle $(l1, l2)$ due to significant deviation from the medial axis; a fiber that resembles most of the fibers in the bundle $(l1, l2)$ may be assigned to a different bundle based on the proximity of its end points to another set of ROIs. The contribution of shape and end points factors are balanced by the bundle variance $\sigma_{l1,l2}$ and end point variance σ, which will be denoted as $\sigma 1$ and $\sigma 2$ respectively in the following text. Decreasing one of the variance would increase the contribution of the corresponding factor while increasing variance would decrease the contribution.

D. Objective function

Given a cortical/sub-cortical parcellation, the model for a full brain fiber set $\mathbf{x}$ can be expressed as a mixture of cortex projection bundle models,

$$p(\mathbf{x} \mid \boldsymbol{\mu}, \sigma 1, \sigma 2) = \sum_{l1=1}^{L} \sum_{l2=l1+1}^{L} p(\mathbf{x} \mid \boldsymbol{\mu}_{l1,l2}, \sigma 1, \sigma 2)\,, \tag{5.5}$$

where $\sigma 1, \sigma 2$ are the bundle and the cortex projection variance respectively. They are set to fixed values. Therefore, the only variable that needs to be estimated is the medial axis $\boldsymbol{\mu}_{l1,l2}$. Note that the second summation is taken from $l1+1$ to L for the index $l2$. It is guaranteed that there is no difference between the bundle connecting $l1$ to $l2$ and the bundle from $l2$ to $l1$. Bundles with two ends in the same ROI are not considered in this work.

Assuming each fiber is an independent sample from this distribution, an optimal $\boldsymbol{\mu}$ can be estimated by maximizing the below likelihood,

$$\hat{\boldsymbol{\mu}} = \arg\max_{\boldsymbol{\mu}} p(\mathbf{x} \mid \boldsymbol{\mu}, \sigma 1, \sigma 2) = \arg\max_{\boldsymbol{\mu}} \prod_{j=1}^{J} \sum_{l1=1}^{L} \sum_{l2=l1+1}^{L} p(\mathbf{x}_j \mid \boldsymbol{\mu}_{l1,l2}, \sigma 1, \sigma 2), \tag{5.6}$$

where j indexes a fiber in the full brain fiber set and there are totally J fibers.

E. EM algorithm

The classic solution to this type of problem, expectation and maximization (EM) algorithm, is used to solve an optimal $\boldsymbol{\mu}$. Given an initial $\boldsymbol{\mu}^0$, the expectation (E) and maximization (M) step are alternatively performed until convergence is achieved. In E step, based on the current estimation $\boldsymbol{\mu}^{n-1}$, the fiber-to-bundle membership is computed using the below formula,

$$m^n_{j,(l1,l2)} = \frac{p(\mathbf{x}_j \mid \boldsymbol{\mu}^{n-1}_{l1,l2}, \sigma 1, \sigma 2)}{\sum_{l1=1}^{L} \sum_{l2=l1+1}^{L} p(\mathbf{x}_j \mid \boldsymbol{\mu}^{n-1}_{l1,l2}, \sigma 1, \sigma 2)}, \tag{5.7}$$

where $m^n_{j,(l1,l2)}$ represents the membership of fiber $\mathbf{x}_j$ to bundle $(l1, l2)$. In essence, $m^n_{j,(l1,l2)}$ is the likelihood of fiber $\mathbf{x}_j$ to bundle $(l1, l2)$ normalized cross all bundles.

In the M step, using the estimated $m^n_{j,(l1,l2)}$, an optimal $\boldsymbol{\mu}^n$ is found to maximize the below likelihood,

$$E(\boldsymbol{\mu}^n) = \sum_{j=1}^{J} \sum_{l1=1}^{L} \sum_{l2=l1+1}^{L} m^n_{j,(l1,l2)} \log(p(\mathbf{x}_j \mid \boldsymbol{\mu}^n_{l1,l2}, \sigma 1, \sigma 2))^{,}$$

which leads to the below update formula for $\boldsymbol{\mu}^n$,

$$\boldsymbol{\mu}^n_{l1,l2} = \frac{\sum_{j=1}^{J} m^n_{j,(l1,l2)} \mathbf{x}_j}{\sum_{j=1}^{J} m^n_{j,(l1,l2)}}. \tag{5.8}$$

The above updated scheme is essentially a weighted sum of all fibers with the memberships. Using only the Gaussian bundle model (Equation 5.3), memberships are solely determined by distances between individual fibers to their corresponding bundle medial axes. This leads to a maximization of the bundle coherences. Using the cortex projection bundle model, an exponential decay term is added to attenuate memberships based on end-to-ROI distances, which would constrain the bundling process so that the bundle centroid would not deviate much from their corresponding ROI regions. The

inherent coherence preserving force is to correct inaccurate ROI labeling caused by image mis-registration while the parcellation constrain places a certain level of confidence on registered ROI masks.

F. Implementation issues

From Equation 5.7 and 5.8, it can be seen that the computational complexity is linearly proportional to the total number of fibers, which is huge (~40,000) for each subject. To reduce the total number of fibers, $m_{j,(l1,l2)}$ is set to zero if one of $\mathbf{x}_j$'s end points is more than $3\sigma 2$ far away from ROI $l1$ or $l2$. Then $m_{j,(l1,l2)}$ would be never evaluated, nor is $\mathbf{x}_j$ involved into the update of $\boldsymbol{\mu}_{l1,l2)}$. With these simplifications, a significant amount of computation are avoided, leading to one minute for each iteration (Intel Xeon 5150 2.66 G Hz).

In E step, each fiber is assigned to the bundle with the maximum membership. The algorithm automatically terminates when the total number of changes to fiber-to-bundle assignment is below a threshold (set to 20 in this work) or the number of iterations reaches 10.

3. Experiments and results

A. Grey matter parcellation template

In Tzourio-Mazoyer's work (2002), the grey matter in a MNI single subject MRI data is manually parcellated into 90 regions of interest (ROIs), the so called automated anatomical labeling (AAL) mask. This set of ROIs includes 39 cortical regions on each brain hemisphere and 12 sub-cortical regions. The definitions of all the ROIs are listed in table 5.1. Similar to Gong et al's work (2008), these ROIs are considered to be basic units

of the brain grey matter, and the goal of this study is to automatically group fibers to bundles connecting pairs of ROIs.

Table 5.1 The list for all ROI definitions in the AAL mask.

Gyrus Rectus	Middle occipital gyrus
Olfactory Cortex	Inferior occipital gyrus
Superior frontal gyrus, orbital part	Calcarine fissure and surrounding cortex
Superior frontal gyrus, medial orbital	Cuneus
Middle frontal gyrus orbital part	Lingual gyrus
Inferior frontal gyrus, orbital part	Fusiform gyrus
Superior frontal gyrus, dorsolateral	Heschl gyrus
Middle frontal gyrus	Superior temporal gyrus
Inferior frontal gyrus, opercular part	Middle temporal gyrus
Inferior frontal gyrus, triangular part	Inferior temporal gyrus
Superior frontal gyrus, medial	Temporal pole: superior temporal gyrus
Supplementary motor area	Temporal pole: middle temporal gyrus
Paracentral lobule	Parahippocampal gyrus
Precentral gyrus	Anterior cingulate and paracingulate gyri
Rolandic operculum	Median cingulate and paracingulate gyri
Postcentral gyrus	Posterior cingulate gyrus
Superior parietal gyrus	Insula
Inferior parietal, but supramarginal and angular gyri	Hippocampus
Supramarginal gyrus	Amygdala
Angular gyrus	Caudate
Precuneus	Putamen
Superior occipital gyrus	Pallidum
	Thalamus

B. Imaging and fiber tracking

T1 weighted and DWI images were acquired for ten healthy human subjects using a 3T Philips Achieva MR scanner. Informed consent was given by the subjects according to a protocol that was approved by a local ethics committee. Each T1 volume contains a 170×256×256 matrix with an isotropic solution of 1×1×1 mm^3. The DWI data were acquired with 32 non-collinear weighting directions (b = 1000 s/mm^2), yielding a volume of 128×128×60 voxels at an isotropic resolution of 2×2×2 mm^3 for each direction. Three

repeated scans were performed then registered in order to correct motion and distortion. A linear least-square fitting was used to estimate diffusion tensors. Then a streamline tracking algorithm was started at all the voxels with FA above 0.15, and then sequentially followed the local PDDs at a step size of 2mm. A fiber was terminated when voxels with FA below 0.15 are met or the angles between two consecutive PDDs exceed 41°. The above procedure generated a whole volume fiber set (~40,000 fibers) for each subject (see Figure 5.1 for an example).

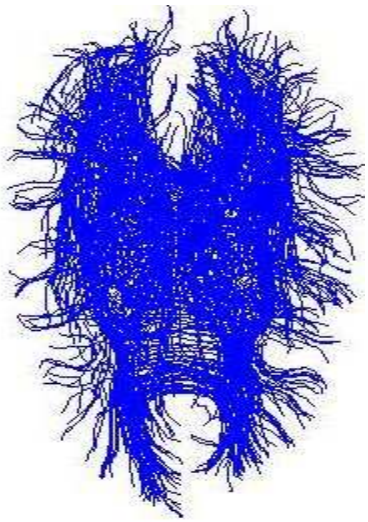

Figure 5.1 The axial view of a whole volume fiber set. (For the efficiency of rendering, only 10% fibers are randomly selected and displayed.)

C. Registration of AAL mask with fibers

A series of image registration and transformation steps are taken to map fibers from their native space to the MNI space. Firstly, a subject's b0 DWI image is registered to its T1 weighted image using normalized mutual information as a metric. As the b0 DWI image and fibers are in the same space, the resulting rigid transformation can warp fibers to the T1 scan space. Next, the subject's T1 image is registered to the MNI T1 template with

intensity difference as a metric. The output discrete cosine transformation is used to map fibers from the subject's T1 scan space to the MNI space, where the AAL mask is available. Although fibers can be directly bundled based on positions of their end points on the AAL mask, the possible registration errors could cause fibers to be transformed into a space slightly different from the MNI space and thus this kind of bundling could provide inaccurate results.

D. Metrics

Given the AAL mask, the proposed algorithm is used to bundle these fibers in the MNI space. To quantitatively characterize the bundling results, two metrics are proposed in this work: (1) the mean in-bundle variation (MIV) and (2) the mean end-to-ROI distance (MED). The MIV measures the coherence of bundles, which is expressed as the mean of distances between fibers and their bundle centroids,

$$MIV = \frac{1}{J}\sum_{j=1}^{J} | \mathbf{x}_j - \boldsymbol{\mu}_{\varphi(j)} | , \tag{5.9}$$

where $|\bullet|$ denotes the distance between two fibers and $\varphi(\bullet)$ is the fiber assignment function that maps fiber $\mathbf{x}_j$ to a bundle. The MED characterizes the deviation of fibers from their assigned ROI pairs. This metric is expressed as follows,

$$MED = \frac{1}{J}\sum_{j=1}^{J} \phi_{l1_{\varphi(j)}}(\mathbf{r1}_j) + \phi_{l2_{\varphi(j)}}(\mathbf{r2}_j) , \tag{5.10}$$

where $\mathbf{r1}_j$ $\mathbf{r2}_j$ are the starting and the end points of fiber $\mathbf{x}_j$ respectively, and $l1_{\varphi(j)}$ $l2_{\varphi(j)}$ are the two ROIs that $\mathbf{x}_j$ connects to. $\phi_{l1_{\varphi(j)}}(\bullet)$ and $\phi_{l2_{\varphi(j)}}(\bullet)$ are the distances transform of $l1_{\varphi(j)}$ and $l2_{\varphi(j)}$ respectively. A bundling with high consistency to the parcellation would have a small MED.

E. Convergence

The proposed bundling algorithm ($\sigma 1 = 2, \sigma 2 = 2$) is applied to all ten subjects. The number of fiber assignment changes is recorded at each iteration, and the algorithm achieves convergence (below 20 changes) in nine iterations for all ten cases (see Figure 5.2).

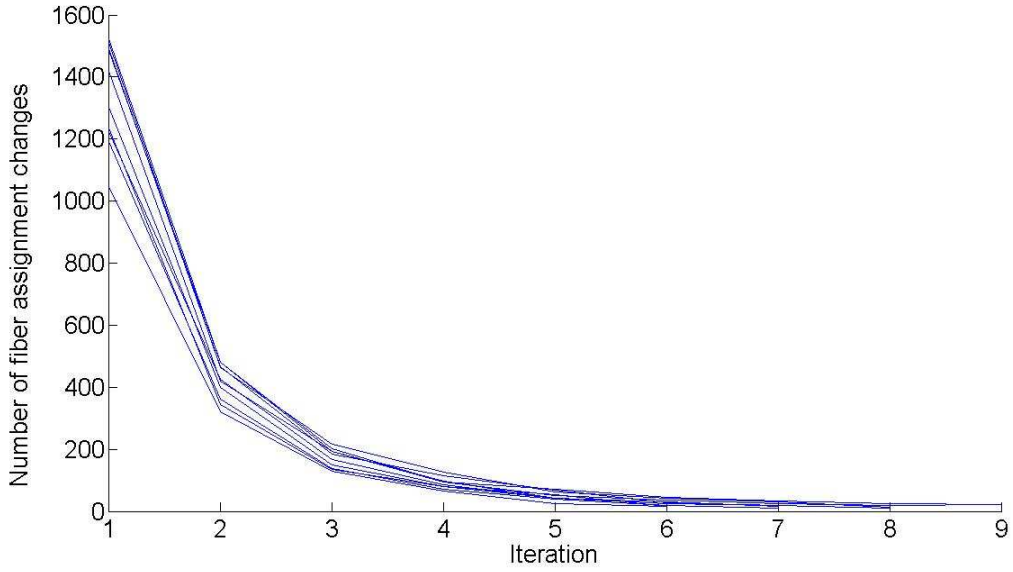

Figure 5.2 The variations of the number of fiber-to-bundle assignment changes with respect to the iteration index for all ten subjects.

F. Effect of the cortex projection variance

The proposed bundling algorithm is applied to one of the subjects several times with $\sigma 2$ changing from 0.5 to 5 and $\sigma 1$ fixed to be 2. The curve in Figure 5.3 (a) shows that the number of iterations for convergence increases with the increase of $\sigma 2$, so a smaller $\sigma 2$ would allow for faster algorithm converge. A big $\sigma 2$ implicitly results in less confidence on the ROI mapping and thus the effect of the ROI constrain is weakened, which makes the clustering process longer. In Figure 5.3 (b) the MIV decreases with the

increase of $\sigma 2$, which is caused by an increasing contribution of the clustering/coherence preserving "force". It also can be seen from Figure 5.3 (c) that the MED increases with the increase of $\sigma 2$, as this would reduce the "force" of dragging a bundle to its corresponding ROI pair so that the bundle can more easily move away from ROIs. In extreme cases, a zero $\sigma 2$ would turn the algorithm into a simple one that groups fibers based on their closest ROI pairs, while a positive infinite $\sigma 2$ would turn the algorithm into a pure clustering algorithm without using the anatomical information. $\sigma 2$ is set to 2 for following experiments to make a balance between MED and MIV.

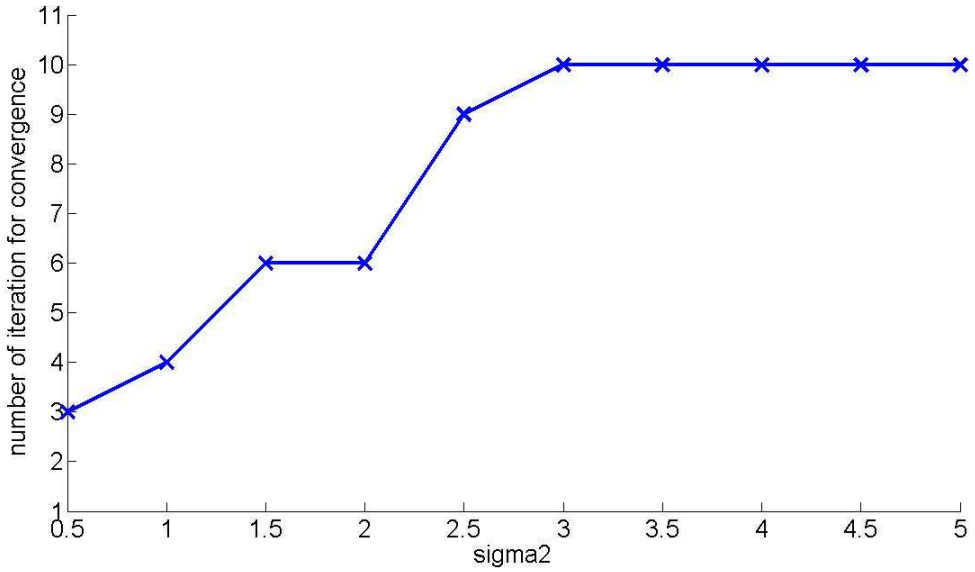

(a)

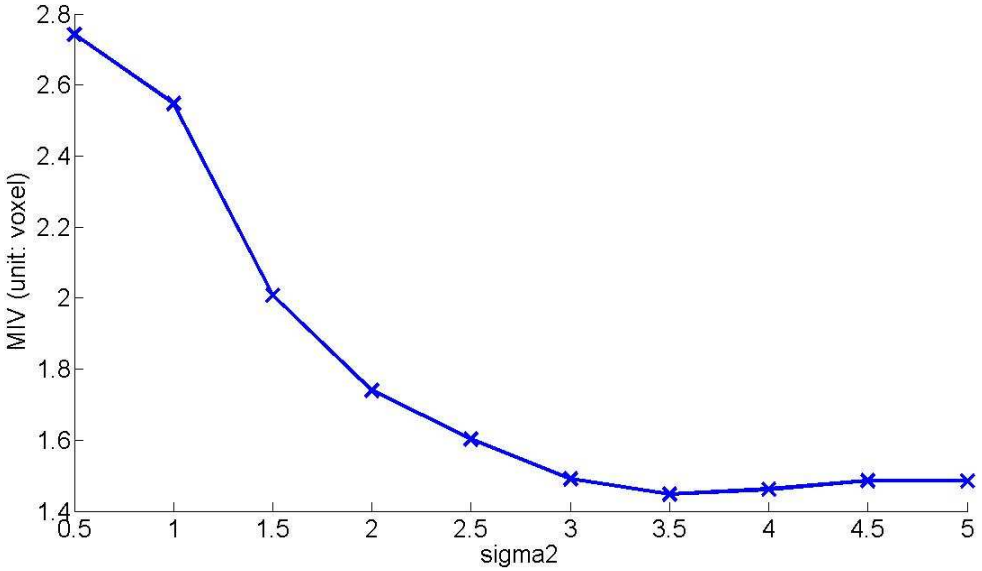

(b)

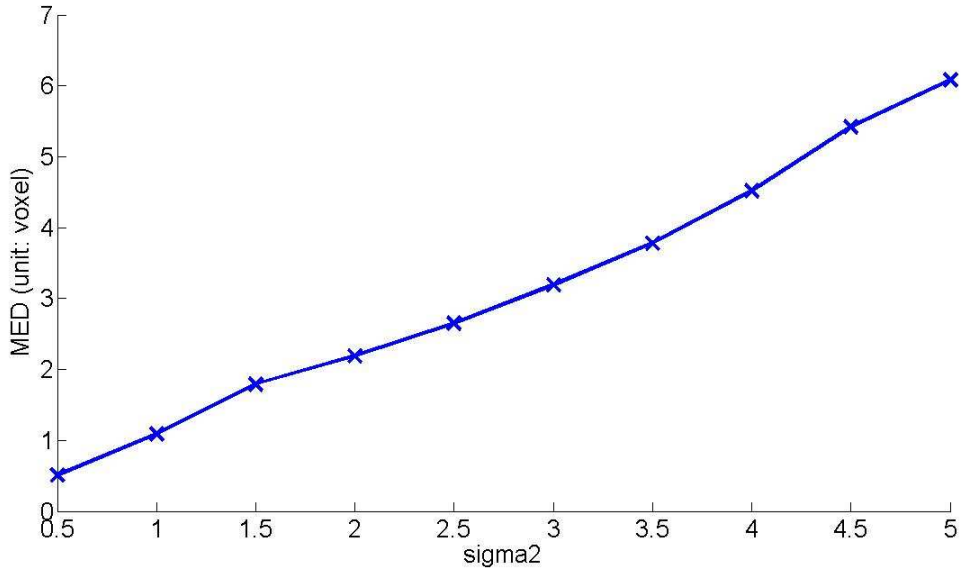

(c)

Figure 5.3 Variations of (a) numbers of iterations for convergences, (b) the MIV, and (c) the MED with respect to the cortex projection variance value.

G. Comparisons with baseline methods

In this experiment, the proposed algorithm is compared with two other baseline methods: (1) clustering without using the parcellation constraint (method I) and (2) bundling solely based on the parcellation (method II).

Two examples of the resulting bundles from these methods are illustrated in Figure 5.4. In Figure 5.4 (a) and (b), the bundle connecting the left hippocampus to the left Caudate is displayed for both the proposed method (a) and method II (b). It can be seen from Figure 5.4 (b) that method II incorrectly includes several outlier fibers (pointed by the green arrow), which deviate significantly from the majority of the bundle, as their end points fall into the left hippocampus to the left Caudate. These outliers are discarded by the proposed method, as their existence in this bundle would increase the in-bundle variation or reduce the coherence of bundle. On the other hand, method I that only aims at maximizing such coherence will also produce some erroneous results as in Figure 5.4 (d). Although initialized as a connection between the left inferior frontal gyrus, triangular part and the left supplementary motor area, the bundle finally converges to one that doesn't even connect these two ROIs. The proposed algorithm is capable of constraining the bundle to the two ROIs in the process of clustering.

To further quantify this performance, the MIV and MED are summarized in Figure 5.5 for all the ten subjects. Although method I and method II could achieve minimum MIV and MED respectively, they generate poor values for the other metric. On the other hand, the proposed algorithm yields close-to-minimum values for both the two metrics.

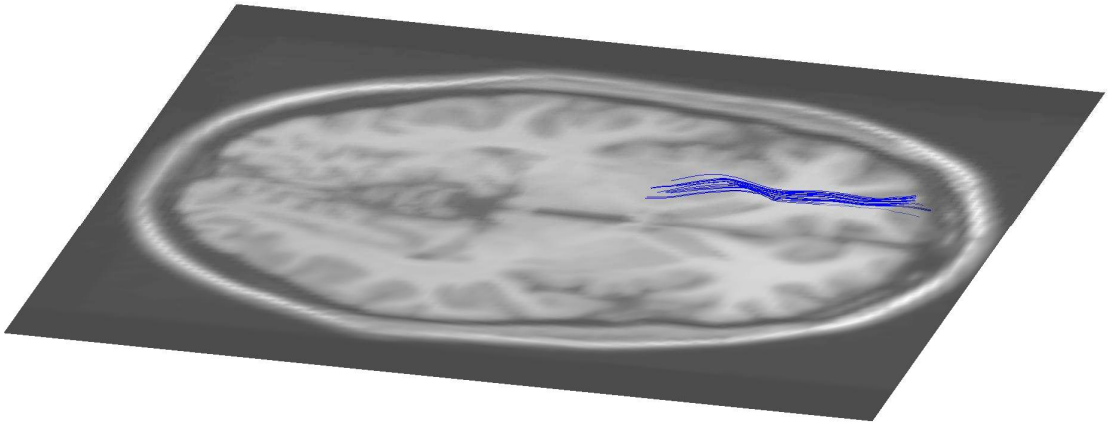

(a)

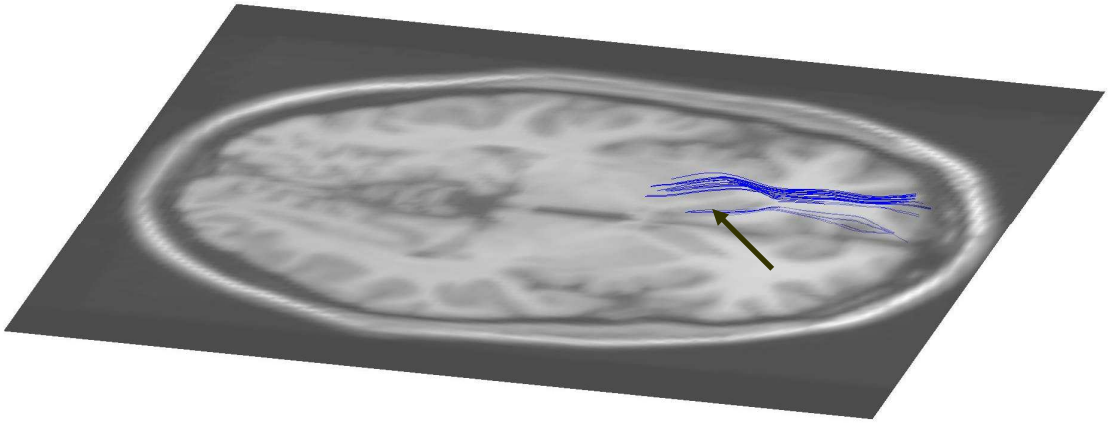

(b)

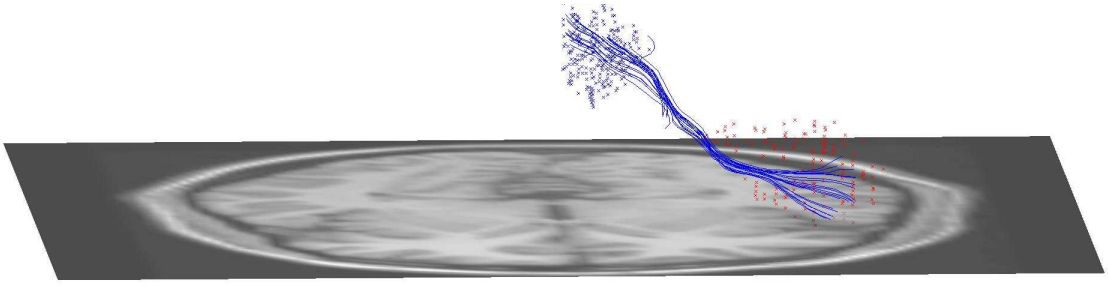

(c)

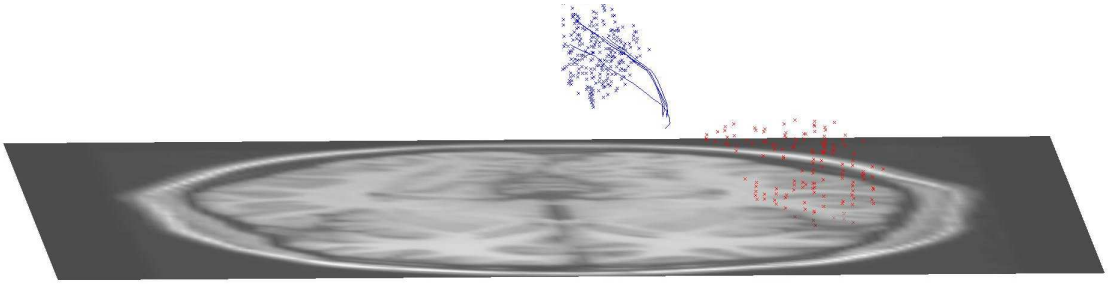

(d)

Figure 5.4 Illustrative comparisons between the proposed algorithm and the baseline methods. (a) (generated by the proposed algorithm) and (b) (generated by the method II) display the bundle connecting the left hippocampus to the left Caudate. (c) (generated by the proposed algorithm) and (d) (generated by method I) display the bundle connecting the left inferior frontal gyrus, triangular part to the left supplementary motor area.

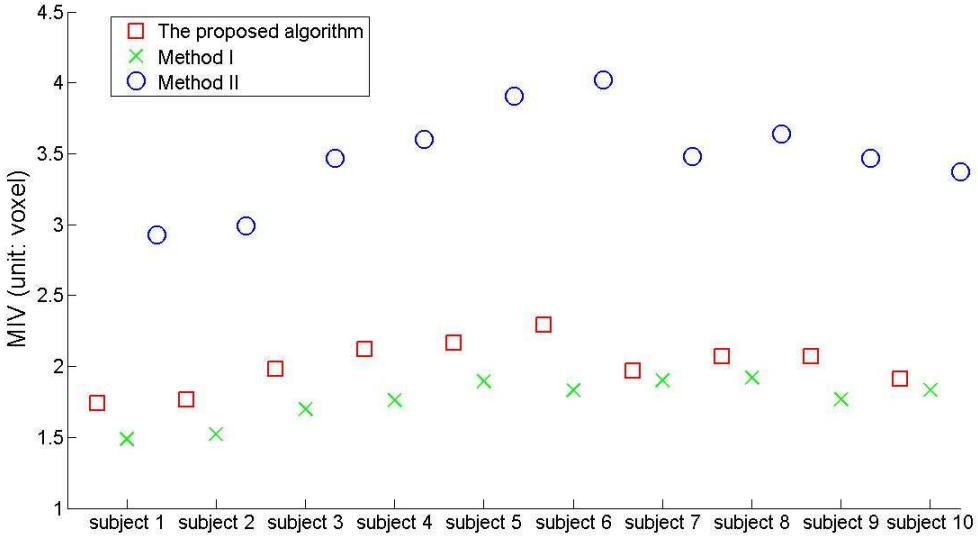

(a)

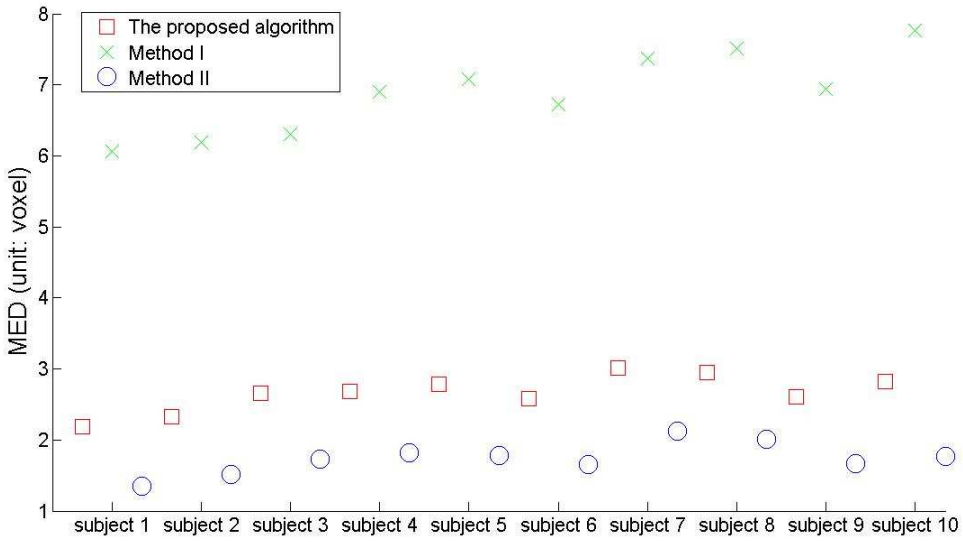

(b)

Figure 5.5 The MIV (a) and the MED (b) for the proposed parcellation constrained bundling and the two baseline methods.

H. Demonstrations of resulting bundles

Due to the image mis-registration and uncertainties in fiber tracking, it is possible that some bundles are falsely generated for non-existing connections between two cortical/sub-cortical units. To eliminate outlier bundles, only bundles consistent across the whole subject group are identified and retained as valid connections. To measure such a group consistency, we computed the variance for the bundle centroids. Bundles with variance above 2.5 are discarded, resulting in totally 36 consistent bundles rendered in Figure 5.6.

(1a)

(1b)

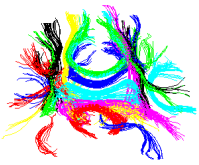

(1c)

(2a)

(2b)

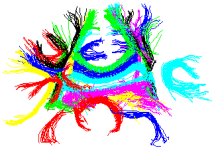

(2c)

(3a)

(3b)

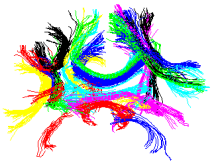

(3c)

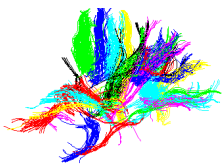

(4a)

(4b)

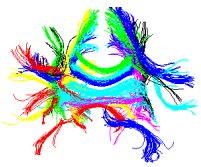

(4c)

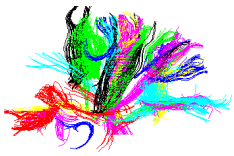

(5a)

(5b)

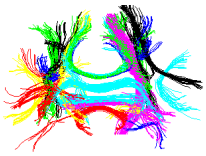

(5c)

(6a)

(6b)

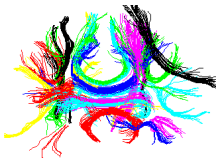

(6c)

(7a)

(7b)

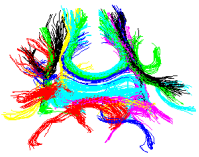

(7c)

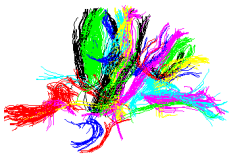

(8a)

(8b)

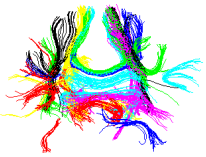

(8c)

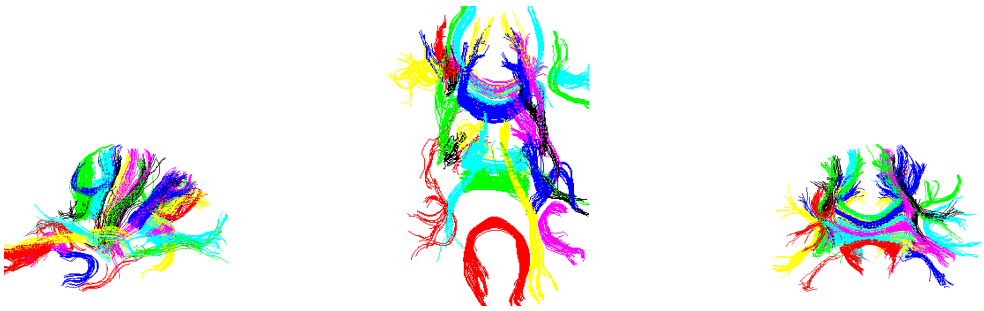

(9a) (9b) (9c)

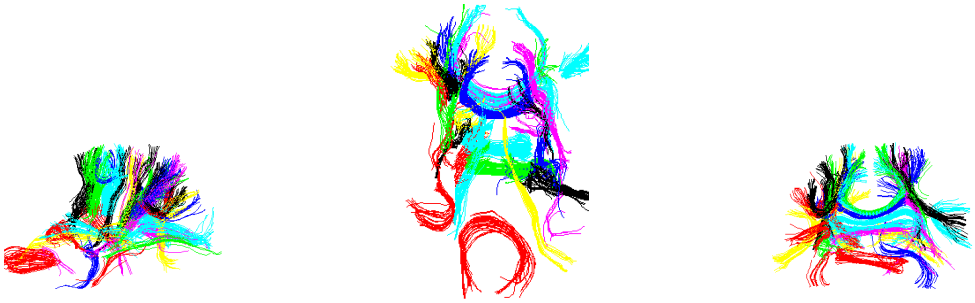

(10a) (10b) (10c)

Figure 5.6 Saggital (column (a)), axial (column (b)) and coronal (column (c)) view of the full brain bundling results using the proposed parcellation constrained approach.

4. Conclusions

The goal of this work is to automatically cluster DTI fibers into a set of anatomical bundles connecting cortical/sub-cortical basic units. However, there are three challenges: (1) traditional data-driven clustering algorithms, which solely rely on fibers' intrinsic similarities, could yield irrelevant bundles having no anatomical correspondences; (2) it is difficult to manually parcellate the cortical/sub-cortical units due to the complexity of grey matter and the lack of imaging contrast; (3) the cumulative process of fiber tracking magnifies noises introduced at imaging stages and hence generates fibers that deviate significantly from their true positions.

To address these issues, the anatomical information of grey matter is firstly incorporated into the fiber bundle model based on fibers' distances to anatomical mappings, e.g., the AAL mask. Such a model tolerates the possible inaccuracy of anatomical mappings, which is often aligned with fibers using image registration, and admits the possible errors of fiber tracking, which are particularly serious near the grey matter. Based on this model, a single-subject based bundling approach is further proposed to cluster fibers into connections between pairs of cortical/sub-cortical units. The experiments with real human brain DTI data has demonstrated that the algorithm is capable of generating bundles that are both spatially coherent and close to their corresponding cortical/sub-cortical units.

CHAPTER VI

CONSISTENT GROUP-WISE BUNDLING

In a typical clinical study, fibers from a group of subjects are quite often required to be bundled consistently and then analyzed. Using a single-subject based bundling approach would lead to two problems: (1) resulting bundles are possibly inconsistent between different subjects in terms of their numbers of fibers, shapes and locations; (2) bundle centroids are less likely aligned across subjects and bundle based morphometry can't be directly performed as a result. The goal of this work is to extend the proposed parcellation constrained bundling to a group-wise bundling algorithm that improves across-subject consistency of resulting bundles and aligns them as well.

1. Introduction

DTI fibers are constructed through a link of steps, including DWI acquisition, tensor fitting and fiber tracking. Each step introduces certain errors due to noises, model inadequacy etc., resulting in final noised fibers. Such noises are different from subject to subject so that a clustering algorithm based on an individual dataset may generate bundles that are tuned to fit their individual noises. This may cause resulting bundles to be inconsistent across subject group, even if subjects in the group have identical anatomical structures.

To reduce the effect of noises, multiple samles shall be collected to estimate the true measurements. In the case of fiber bundling, each fiber set can be considered to be an

independent sample from a full brain bundle model. Such an assumption can be made when fiber sets are reconstructed from a group of subjects with the same condition or even from the same subject. Let $\mathbf{x}^s$ denote the sth fiber set in the subject group, where s could range from 1 to S, the total number of subjects in the group. Using the cortex projection bundle model, the group-wise bundle centroids $\boldsymbol{\mu}$ can be estimated by maximizing the below likelihood,

$$\hat{\boldsymbol{\mu}} = \arg\max_{\boldsymbol{\mu}} \prod_{s=1}^{S} p(\mathbf{x}^s \mid \boldsymbol{\mu}, \sigma 1, \sigma 2),$$

where $\sigma 1, \sigma 2$ are the fiber variance and cortex projection variance respectively.

One problem with the above estimation is that each fiber set is in their own native space as subjects are usually scanned in different positions and orientations. Therefore, it is necessary to transform all fiber sets into a common space prior to the estimation. Although image-based registration using T1 weighted MR or FA map could be applied to this alignment, fiber orientations are not guaranteed to be well aligned due to the limited information considered. On the other hand, fiber-based registration using the full brain fibers might be too computationally complex and time-consuming, as there are usually a huge amount of fibers for each fiber set. Therefore, it would be more efficient to align bundle centroids. However, since fiber bundles are yet to be estimated, there are no reliable bundles that can be used to make this alignment.

As the solutions to the group-wise bundling and the spatial alignment could benefit each other, these two goals are coupled into a unified objective function, from which an optimal transformation and bundling are jointly estimated. Similar to the previous chapter,

the image-based registration procedure is firstly applied to map each fiber set into the Montreal Neurological Institute (MNI) space for two reasons: (1) this registration essentially provides an initial alignment so that local minimal solutions can be avoided in the optimization; (2) a cortical/sub-cortical mapping prior is naturally provided to support the cortex project bundle model.

2. Methods

A. Objective function

Let $\boldsymbol{T}^s$ be a transformation that warps the fiber set $\boldsymbol{x}^s$ from its native space into a common space, which is the MNI space in this work. The joint group-wise bundling and alignment can be cast as an optimization problem that simultaneously seeks an optimal model $\boldsymbol{\mu}$ and optimal transformations $\boldsymbol{T}^s$. Using a Bayesian framework, an optimal solution can be obtained by a maximum *a posteriori* (MAP) approach,

$$\begin{aligned}\boldsymbol{\theta} &= (\mathbf{T}^{1,2,\ldots,S}, \boldsymbol{\mu}) \\ &= \arg\max_{\mathbf{T}^{1,2,\ldots,S},\boldsymbol{\mu}} \prod_{s=1}^{S} p(\mathbf{x}^s \mid \boldsymbol{\mu}, \sigma 1, \sigma 2, \mathbf{T}^s)\end{aligned}. \tag{6.1}$$

It is assumed that each transformed fiber in the MNI space is an independent and identically distributed sample that is drawn from the distribution of the group bundle model, which leads to the below expression,

$$\begin{aligned}
&\prod_{s=1}^{S} p(\mathbf{x}^s \mid \mathbf{T}^s, \boldsymbol{\mu}, \sigma 1, \sigma 2) \\
&= \prod_{s=1}^{S} p(\mathbf{T}^s(\mathbf{x}^s) \mid \boldsymbol{\mu}, \sigma 1, \sigma 2) \\
&= \prod_{s=1}^{S} \prod_{j=1}^{M^s} p(\mathbf{T}^s(\mathbf{x}_j^s) \mid \boldsymbol{\mu}, \sigma 1, \sigma 2) \\
&= \prod_{s=1}^{S} \prod_{j=1}^{M^s} \sum_{k=1}^{K} p(\mathbf{T}^s(\mathbf{x}_j^s) \mid \boldsymbol{\mu}_k, \sigma 1, \sigma 2)
\end{aligned}, \tag{6.2}$$

where j, k, s index fibers, bundles and subjects respectively. There are totally $\boldsymbol{K}$ bundles that need to be estimated and $\boldsymbol{M}^s$ fibers for each subject $\mathbf{x}^s$. $p(\mathbf{T}^s(\mathbf{x}_j^s) \mid \boldsymbol{\mu}_k, \boldsymbol{\sigma}1, \boldsymbol{\sigma}2)$ is evaluated using the cortex projection bundle model. The optimal parameters $(\mathbf{T}^{1,2,\ldots,S}, \boldsymbol{\mu})$ can be found by maximizing the above probability.

B. Optimization

The above optimization problem can be solved with the Expectation and Maximization (EM) algorithm. Let $(\boldsymbol{T}^{n,1,2,\ldots,S}, \boldsymbol{\mu}^n)$ denote the parameters estimated in the nth iteration. In E step, the membership probability of a fiber $\mathbf{x}_j^s$ to the kth bundle is estimated as follows,

$$m_{j,k}^{s,n} = \frac{p(\mathbf{T}^{n,s}(\mathbf{x}_j^s) \mid \boldsymbol{\mu}_k^{n-1}, \sigma 1, \sigma 2)}{\sum_{k=1}^{K} p(\mathbf{T}^{n,s}(\mathbf{x}_j^s) \mid \boldsymbol{\mu}_k^{n-1}, \sigma 1, \sigma 2)}. \tag{6.3}$$

In M step, based on the fiber membership $m_{j,k}^{s,n}$, the original objective likelihood is turned into,

$$\begin{aligned}
&E_{EM}(\mathbf{T}^{n,1,2,\ldots S}, \boldsymbol{\mu}^n) \\
&= \sum_{s=1}^{S} \sum_{j=1}^{M^s} \sum_{k=1}^{K} m_{j,k}^{s,n} \log(p(\mathbf{T}^{n,s}(\mathbf{x}_j^s) \mid \boldsymbol{\mu}_k, \sigma 1, \sigma 2))
\end{aligned}. \tag{6.4}$$

The above objective function can be optimized by firstly fixing the transformations $\mathbf{T}^{n,1,2,...S}$ to be $\mathbf{T}^{n-1,1,2,...S}$ and then solve the differential equations,

$$\frac{dE_{EM}}{d\boldsymbol{\mu}^n} == 0,$$

which leads to the below solution,

$$\boldsymbol{\mu}_k^{\ n} = \frac{\sum_{s=1}^{S}\sum_{j=1}^{M^s} m_{j,k}^{s,n}\mathbf{T}^{s,n-1}(\mathbf{x}_j^s)}{\sum_{s=1}^{S}\sum_{j=1}^{M^s} m_{j,k}^{s,n}}, \tag{6.5}$$

Next $\boldsymbol{\mu}^n$ is computed and fixed, we minimize the below objective function to estimate transformations $\mathbf{T}^{n,1,2,...S}$,

$$E_{EM}(\mathbf{T}^{n,1,2,...S}) = \sum_{s=1}^{S}\sum_{j=1}^{M^s}\sum_{k=1}^{K} m_{j,k}^{s,n}(\mathbf{T}^{s,n}(\mathbf{x}_j^s)-\boldsymbol{\mu}_k^n)(\mathbf{T}^{s,n}(\mathbf{x}_j^s)-\boldsymbol{\mu}_k^n)^T.$$

The minimization of $E_{EM}(\mathbf{T}^{n,1,2,...S})$ is a least-squares fitting problem, and its computational cost depends mainly on the number of target fibers M^s and the total number of subjects S. To improve the computational efficiency, we circumvent the direct optimization of $E_{EM}(\mathbf{T}^{n,1,2,...S})$ by minimizing a simpler form $E_{EM}'(\mathbf{T}^{n,1,2,...S})$ as follows,

$$E_{EM}'(\mathbf{T}^{n,1,2,...S}) = \sum_{s=1}^{S}\sum_{k=1}^{K}(\mathbf{T}^{s,n}(\mathbf{y}_k^{s,n})-\boldsymbol{\mu}_k^n)(\mathbf{T}^{s,n}(\mathbf{y}_k^{s,n})-\boldsymbol{\mu}_k^n)^T, \tag{6.6}$$

where

$$\mathbf{y}_k^{s,n} = \sum_{j=1}^{M^s} m_{j,k}^{s,n} \mathbf{x}_j^s .$$

$\mathbf{y}_k^{s,n}$ can be interpreted as the current estimation of the kth bundle centroid for the sth individual subject. The optimization of Equation 6.6 is essentially aligning bundle centroids of each subject to their group centroids. This simplification would make the computation proportional to the size of number of bundles, which is much smaller than the total number of fibers in all data set. In the case of full brain bundling, even with this reduction, the computational complexity is still unacceptable due to a larger number of bundles (typically ~1000). Therefore, each centroid is further downsampled (3 times) in order to fit the computation to our hardware resources.

Theoretically any form of transformation can be used in the above framework. Thin-Plate Spline (TPS) transformation is chosen in this work due to its smoothness in deformation fields and closed-form solution for warping and parameter estimation (Rohr et al., 2001). For the optimization of Equation 6.6 please refer to the section 5B in chapter III.

3. Experiments and results

The data and the pre-processing procedures (tensor fitting, fiber tracking, and initial image registration) remain the same as what are used in chapter V. Figure 6.1 shows the initial position of an individual fiber set on the MNI T1 weighted template.

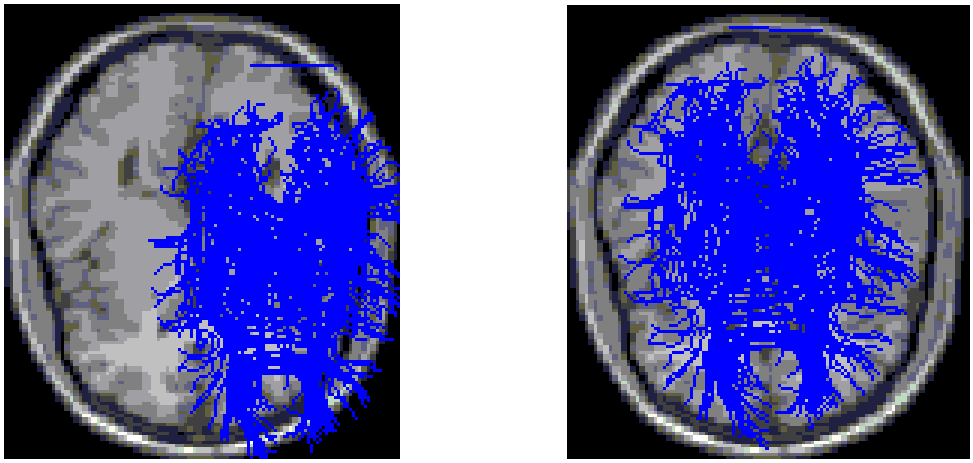

(a) (b)

Figure 6.1 Overlapping an individual fiber set on the MNI template. (a) An identity transformation is applied to the fibers. (b) The fibers are warped with the resulting transformation from the initial image registration.

A. Baseline methods

To demonstrate the main advantages of the proposed algorithm, we compared it with three baseline methods. The first method (method I) is a straightforward extension of the single-data based bundling from the previous chapter. Each fiber set from the subject group is individually bundled with the cortex projection bundle model. Then the individual bundling results are directly combined to form a group bundle set. To remove the group in-bundle variation caused by the mis-alignment of subjects' bundles, the second method (method II) further registers each subjects' bundle centroids from method I to the corresponding group centroids using a TPS transformation. The third method (method III) uses a joint clustering scheme that treats fibers from all the subjects as a single fiber set and performs the single-data based bundling on this combined data set.

B. Metrics

To measure the bundling consistency across subjects, two metrics are proposed and used in this work. Firstly, the mean group in-bundle variation (MGIV) is computed for the resulting fiber bundles as follows,

$$MGIV = \frac{1}{\sum_{s=1}^{S} M^s} \sum_{s=1}^{S} \sum_{j=1}^{M^s} | \mathbf{x}_j^s - \boldsymbol{\mu}_{\varphi(x_j^s)} |$$

where the assignment function $\varphi(\mathbf{x}_j^s)$ assigns the fiber $\mathbf{x}_j^s$ to a specific bundle. The MGIV measures the coherence of a group bundle set, so a consistent group-wise bundling would reduce the value of this metric by eliminating the variation caused by the inconsistency across the group. However, MGIV might be also contributed by the intrinsic bundle variance of each individual subject, so it is desirable to have a metric that directly measures only the consistency between different subjects. Considering the subject specific ($\boldsymbol{\mu}^s$) and the group bundle centroid ($\boldsymbol{\mu}$), the norm of their differences can be used to measure the deviation of each subject's model from the group mean, and hence this metric can be used to quantify the consistency. The mean bundle centroid difference (MBCD) can be computed as follows,

$$MBCD = \frac{1}{KS} \sum_{k=1}^{K} \sum_{s=1}^{S} | \boldsymbol{\mu}_k^s - \boldsymbol{\mu}_k | .$$

C. Results

The above metrics are computed and summarized in table 6.1 for all of the four methods, including the proposed method and the other three baseline methods. It can be seen that the proposed consistent group-wise bundling has the smallest values for both metrics, which indicates its superiority in consistency preserving. Although a non-rigid

transformation is used in method II to align bundle centroids with their group mean after the clustering, the resulting metric values still can't compete with the proposed algorithm due to the absence of this alignment within the clustering process. Different from this post-alignment, the proposed algorithm performs alignment in every iteration so that he clustering could more likely select the partition that generates more consistent bundles. Method III can't reduce much inconsistency either due to the mis-alignment caused by initial image registration. From this example, one can see that it is important to integrate the non-rigid alignment into the clustering process.

Table 6.1. The MGIV and MBCD for all of the four bundling methods.

	Consistent bundling	Method I	Method II	Method III
MGIV	3.7420	4.9774	4.5381	4.4109
MBCD	1.3144	2.7785	2.1989	1.9017

D. Demonstration of resulting bundles

To demonstrate the identified connections, the same elimination procedure as the previous chapter is applied to the resulting bundles, generating 45 bundles for each subject. These bundles are illustrated in Figure 6.2.

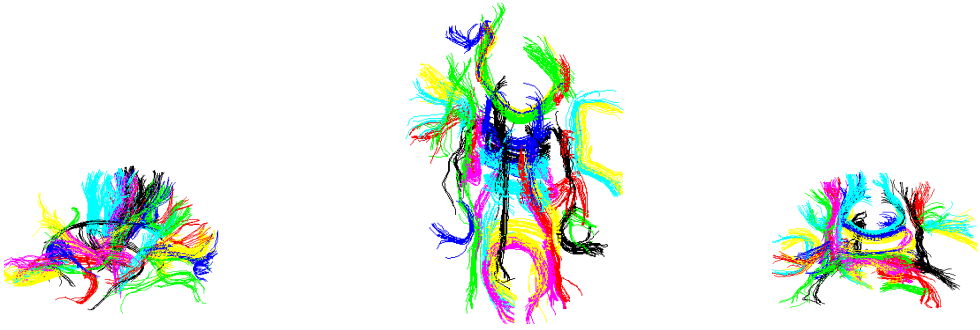

(1a) (1b) (1c)

(2a)

(2b)

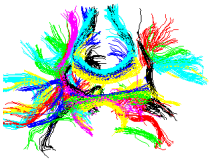

(2c)

(3a)

(3b)

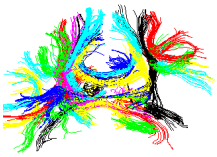

(3c)

(4a)

(4b)

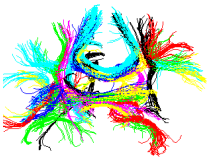

(4c)

(5a)

(5b)

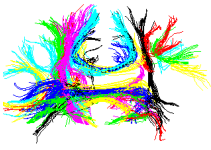

(5c)

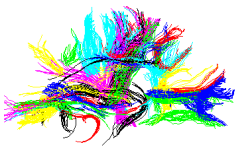

(6a)

(6b)

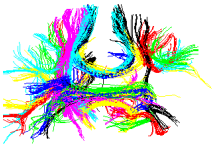

(6c)

(7a)

(7b)

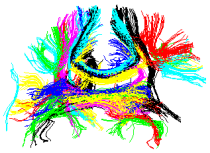

(7c)

(8a)

(8b)

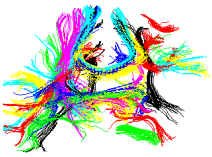

(8c)

(9a)

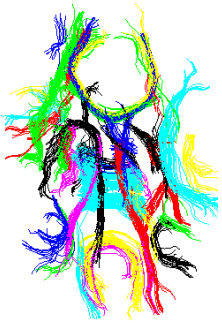

(9b)

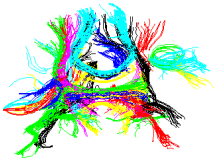

(9c)

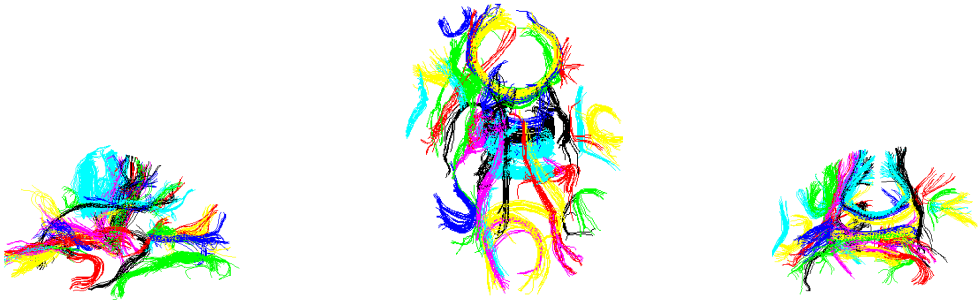

(10a) (10b) (10c)

Figure 6.2 Saggital (column (a)), axial (column (b)) and coronal (column (c)) view of the full brain bundling results using the proposed parcellation constrained approach.

4. Conclusions

To consistently bundle fibers from a group of subjects, a group-wise bundling algorithm is proposed in this work to jointly cluster a group of fiber sets and simultaneously register each individual fiber set to a common template space. The registration component reduces the cross-subject inconsistency caused by spatial mis-alignment, and thus makes it possible to combine fibers from the whole group for group-wising bundling. The clustering component provides bundle centroids for efficient spatial fiber registration so that computational cost is reduced to an acceptable level. The experiments with *in vivo* imaging data show that such an algorithm is able to produce more consistent fiber bundles than single-data based algorithms.

CHAPTER VII

CONCLUSIONS

The aims of this thesis were to develop methods that can be used to cluster DTI fibers into a set of anatomical bundles in a fully automatic and consistent manner. However, in the development process, we realized at least four major challenges: (1) traditional data-driven clustering algorithms, which sole rely on the intrinsic fiber similarity, could yield fiber bundles irrelevant to anatomic structures in the brain; (2) it is difficult to even manually delineate connections between cortical/sub-cortical units due to the low signal-to-noises ratio and the fairly complex structures in the grey matter; (3) The cumulative process of fiber tracking causes noises introduced at imaging stages to be magnified so that reconstructed fibers deviate significantly from their true underlying structures; (4) the uncertainties that are caused by all the above factors make algorithm resulting bundles inconsistent cross a group of subjects, even with the same conditions. To address these issues, several fiber bundling methods have been proposed and evaluated in this thesis.

The firstly proposed method, the unified fiber bundling and registration algorithm (UFIBRE), is to provide fiber bundling consistent with the well-defined major white matter pathways, e.g., the cortical-spinal and the corpus callosum tracts. One common property of these pathways is that they can be reliably delineated from a scalar image, e.g., factional anisotropy map and T1 weighted images, so that at least a bundle template

can be manually segmented. The UFIBRE algorithm then simultaneously clusters an arbitrary non-bundled fiber set and register it to this template. The registration and the clustering component benefit each other in every iteration of the algorithm: (1) The registration constrains the clustering process so that fibers are bundled into a shape consistent with the template; (2) the clustering provides estimated bundle centroids for efficient bundle-to-bundle alignment. This algorithm is evaluated using *in vivo* fiber data with a manually constructed group truth. Experiment results show that the UFIBRE algorithm can produce fiber bundles consistent with the human experts' ground truth (sub-voxel accuracies are achieved for bundle centroids.)

The secondly proposed method, a parcellation constrained full brain bundling algorithm, is applied to bundles whose templates cannot be reliably built, e.g., connections between pairs of cortical/sub-cortical units. Leveraging an anatomical parcellation, e.g., the AAL mask, this method firstly maps fibers from their native space to the parcellation space, e.g. the MNI space, using an image-based registration. A cortex projection model is then proposed to incorporate the information of brain anatomy into the regular Gaussian bundle model so that the clustering algorithm based on this can achieve both bundle coherence and anatomy consistency simultaneously. Experiments with the real human brain DTI data show that this approach is capable of generating bundles with a good balance between coherence and anatomy consistency within a reasonable computation time.

To overcome the final challenge, the bundling inconsistency cross a group of fiber sets, an algorithm is proposed to perform joint group-wise clustering and bundle alignment. In each iteration, the algorithm registers each individual fiber set to the group bundle model

and then clusters the whole group of fibers. The experiments show that such an algorithm is able to produce more consistent fiber bundles than single-data based algorithms.

We hope that the methods developed in this thesis would help people better characterize white matter bundles, better measure the connectivity of bundles and thus better understand the human brain neuronal network.

REFERENCES

P.J. Basser, J. Mattiello, and D. Le Bihan, “MR diffusion tensor spectroscopy and imaging”, *Biophys J.*, vol. 66(1), pp. 259-267, 1994.

P.J. Basser, S. Pajevic, C. Pierpaoli, J. Duda, A. Aldroubi, “In vivo fiber tractography using DT-MRI data”, *Magn. Reson. Med.,* vol. 44(4), pp. 625-632, 2000.

A. Brun, H. Park, H. Knutsson, and C.-F. Westin, "Coloring of DT-MRI fiber traces using laplacian eigenmaps", In EUROCAST’03, Conf. Proc., Lecture Notes in Computer Science, vol. 2809, pp. 564-572, 2003.

A. Brun, H. Knutsson, H. Park, M. E. Shenton, and C.-F. Westin, “Clustering fiber traces using normalized cuts”, Med. Image Comput. Computer-Assisted Intervention (MICCAI) 2004, pp. 368-375, 2004.

M. Catani, R.J. Howard, S. Pajevic, D.K. Jones, "Virtual in vivo Interactive dissection of white matter fasciculi in the human brain", NeuroImage, Vol. 17(1), pp. 77-94, 2002.

M.-C. Chiang, A.D. Leow, A.D. Klunder, R.A. Dutton, M. Barysheva, S.E. Rose, K.L. McMahon, G.I. de Zubicaray, A.W. Toga, P.M. Thompson, "Fluid registration of diffusion tensor images using information theory", IEEE Trans. Med. Imag., vol. 27(4), pp.442-456, 2008.

O. Ciccarelli, G. J. M. Parker, A.T. Toosy, C.A.M. Wheeler-Kingshott, G.J. Barker, P.A. Boulby, D.H. Miller, and A.J. Thompson, “From diffusion tractography to quantitative white matter tract measures: a reproducibility study”, NeuroImage., vol. 18(2), pp. 348-359, 2003.

T.E. Conturo, N.F. Lori, T.S. Cull, E. Akbudak, A.Z. Snyder, J.S. Shimony, R.C. McKinstry, H. Burton and M.E. Raichle, "Tracking neuronal fiber pathways in the living human brain", Proc. Natl Acad. Sci., vol. 96, pp. 10422-10427, 1999.

I. Corouge, S. Gouttard, and G. Gerig, "Towards a shape model of white matter fiber bundles using diffusion tensor MRI", in Proc. IEEE Int. Symp. Biomed. Imag. (ISBI) 2004, pp. 344-347, 2004.

Purves Dale, George J. Augustine, David Fitzpatrick, William C. Hall, Anthony-Samuel LaMantia, James O. McNamara, and Leonard E. White, "Neuroscience", Sinauer Associates, Maryland, 2008.

Lee. Z. Dice, "Measures of the Amount of Ecologic Association Between Species", Ecology, vol. 26 (3), pp. 297–302, 1945.

Z. Ding, J.C. Gore, and A.W. Anderson, "Classification and quantification of neuronal fiber pathways using diffusion tensor MRI", Magn. Reson. Med., vol. 49(4), pp. 716-721, 2003.

G. Gong, Y. He, L. Concha, C. Lebel, D. W. Gross, A. C. Evans, C. Beaulieu, "Mapping anatomical connectivity patterns of human cerebral cortex using In vivo diffusion tensor imaging tractography", Cereb. Cortex, vol. 20, pp. bhn102+, 2008.

G. Gerig, S. Gouttard, and I. Corouge, "Analysis of brain white matter via fiber tract modeling," EMBS 2004, vol. 2, pp. 4421-4424, 2004.

C. Gossla, L. Fahrmeirb, B. Pütza, L. M. Auerc and D. P. Auera, "Fiber tracking from DTI using linear state space models: detectability of the pyramidal Tract", NeuroImage, vol. 16(2), pp. 378-388, 2002.

A. Guimond, C. Guttmann, S.Warfield, and C.-F.Westin, "Deformable registration of DT-MRI data based on transformation invariant tensor characteristics," in Proc. IEEE Int. Symp. Biomed. Imag. (ISBI) 2002, pp. 761–764, 2002.

M. Guye, F. Bartolomei and J.P. Ranjeva, "Imaging structural and functional connectivity: towards a unified definition of human brain organization?", Current opinion in neurology, vol. 24(4), pp. 393-403, 2008.

O. Friman, G. Farneback and C.F. Westin, "A Bayesian approach for stochastic white matter tractography", IEEE Trans. Med. Imag., vol. 25(8), pp. 965-978, 2006.

P. Hagmann, J.P. Thiran, L. Jonasson, P. Vandergheynst, S. Clarke, P. Maeder and R. Meuli, "DTI mapping of human brain connectivity: statistical fibre tracking and virtual dissection", Neuroimage, vol. 19(3), pp.545-554, 2003.

E. Heiervang, T.E.J. Behrens, C.E. Mackay, M.D. Robson and H. Johansen-Berg, "Between session reproducibility and between subject variability of diffusion MR and tractography measures", NeuroImage, vol. 33(3), pp. 867-877, 2006.

D.K. Jones, A. Simmons, S.C. Williams and M.A. Horsfield, "Non-invasive assessment of axonal fiber connectivity in the human brain via diffusion tensor MRI", Magn. Reson. Med., vol. 42, pp. 37-41, 1999.

D. Jones, L. Griffin, D. Alexander, M. Catani, M. Horsfield, R. Howard, and S. Williams, "Spatial normalization and averaging of diffusion tensor MRI data sets", NeuroImage, vol. 17(2), pp. 592-617, 2002.

R.A. Kanaan, S.S. Shergill, G.J. Barker, M. Catani, V.W. Ng, R. Howard, P.K. McGuire, and D.K. Jones, "Tract-specific anisotropy measurements in diffusion tensor imaging," Psychiat. Res.: Neuroimag., vol. 146, pp.73-82, 2006.

N. Kang, J. Zhang, E.S. Carlson and D. Gembris, "White matter fiber tractography via anisotropic diffusion simulation in the human brain", IEEE Trans. Med. Imag., vol. 24(9), pp. 1127-1137, 2005.

E. Kraepelin, "Dementia praecox", Churchill Livingstone Inc., New York, 1919/1971.

M. Kubicki, R. McCarley, C.F. Westin, H.J. Park, S. Maier, R. Kikinis, F.A. Jolesz, and M.E. Shenton, "A review of diffusion tensor imaging studies in schizophrenia", J Psychiatr Res., vol. 41(1-2), pp. 15-30, 2007.

M. Lazar, D.M. Weinstein, J.S. Tsuruda, K.M. Hasan, K. Arfanakis, M.E. Meyerand, B. Badie, H.A. Rowley, V. Haughton, A. Field and A.L. Alexander, "White matter tractography using diffusion tensor deflection", Hum Brain Mapp., vol. 18(4), pp. 306-321, 2003.

D. Le Bihan, E. Breton, D. Lallemand, P. Grenier, E. Cabanis and M. Laval-Jeantet, "MR imaging of intravoxel incoherent motions: application to diffusion and perfusion in neurologic disorders", Radiology, vol. 161, pp. 401-407, 1986.

A. Leemans, J. Sijbers, S. De Backer, E. Vandervliet, and P. Parizel, “Affine coregistration of diffusion tensor magnetic resonance images using mutual information”, in Advanced Concepts for Intelligent Vision Systems, Lecture Notes Comput. Sci., vol. 3708, pp. 523-530, 2005.

A. Leemans, J. Sijbers, S. De Backer, E. Vandervliet, and P. Parizel, “Multiscale white matter fiber tract coregistration: A new feature-based approach to align diffusion tensor data”, Magn. Reson. Med., vol. 55(6), pp. 1414-1423, 2006.

Y. Lu, A. Aldroubi, J.C. Gore, A.W. Anderson and Z. Ding, "Improved fiber tractography with Bayesian tensor regularization", Neuroimage, vol. 31(3), pp. 1061-1074, 2006.

M. Maddah, A.U.J. Mewes, S. Haker, W.E.L. Grimson and S.K. Warfield, "Automated atlas-based clustering of white matter fiber tracts from DTMRI", Med. Image Comput. Computer-Assisted Intervention (MICCAI) 2005, pp. 188-195, 2005.

M. Maddah, W.E.L. Grimson, and S.K. Warfield, "Statistical Modeling and EM Clustering of White Matter Fiber Tracts", in Proc. IEEE Int. Symp. Biomed. Imag. (ISBI) 2006, pp. 53-56, 2006.

M. Maddah, W.M. Wells, S.K. Warfield, C.-F. Westin, and W.E.L. Grimson, "A spatial model of white matter fiber tracts", ISMRM, 2007a.

M. Maddah, W.M. Wells, S.K. Warfield, C.-F. Westin, W.E. Grimson, "Probabilistic clustering and quantitative analysis of white matter fiber tracts ", Inf. Process. Med. Imaging, vol. 20, pp.372-383, 2007b.

M. Maddah, W.E.L. Grimson, S.K. Warfield, W.M. Wells, "A unified framework for clustering and quantitative analysis of white matter fiber tracts", Med. Image Anal., vol. 12(2), pp. 191-202, 2008.

A. Mayer and H. Greenspan, “Direct registration of white matter tractographies and application to atlas construction,” MICCAI 2007 Workshop Statistical Registration: Pair-wise and Group-wise Alignment and Atlas Formation, 2007.

B. Moberts, A. Vilanova, and J.J. van Wijk, “Evaluation of Fiber Clustering Methods for Diffusion Tensor Imaging,” Proc. IEEE Conf. Visualization (VIS ’05), pp. 65-72, 2005.

S. Mori and P.C.M. van Zijl, "Fiber tracking: principles and strategies - a technical review", NMR in Biomed., vol. 15(7-8), pp. 468-480, 2002.

L. O’Donnell and C.F. Westin, “White matter tract clustering and correspondence in populations,” Med. Image Comput. Computer-Assisted Intervention (MICCAI) 2005, pp. 140-147, 2005.

L. O’Donnell and C.F. Westin, “High-dimensional white matter atlas generation and group analysis,” Med. Image Comput. Computer-Assisted Intervention (MICCAI), pp. 243-251,2006a.

L. O'Donnell, M. Kubicki, M.E. Shenton, M.E. Dreusicke, W.E.L. Grimson, C.-F. Westin, "A Method for Clustering White Matter Fiber Tracts", Am. J. Neuroradiol. (AJNR), vol. 27(5), pp. 1032-1036, 2006b.

L. O'Donnell and CF. Westin, "Automatic tractography segmentation using a high-dimensional white matter atlas", IEEE Trans. Med. Imag., vol. 26(11), pp. 1562-1575, 2007.

N. Ohta, K. Kanatani, “Optimal Estimation of Three-Dimensional Rotation and Reliability Evaluation”, *ECCV'98*, pp. 175- 183, 1998.

H. J. Park, M. Kubicki, M. Shenton, A. Guimond, R. McCarley, S. Maier, R. Kikinis, F. Jolesz, and C.-F. Westin, “Spatial normalization of diffusion tensor MRI using multiple channels”, NeuroImage, vol. 20(4), pp. 1995–2009, 2003.

G.J.M. Parker, C.A.M. Wheeler-Kingshott and G.J. Barker, "Estimating distributed anatomical connectivity using fast marching methods and diffusion tensor imaging", IEEE Trans. Med. Imag., vol. 21(5), pp. 505-512, 2002.

G.J.M. Parker, H.A. Haroon and C.A.M. Wheeler-Kingshott, "A framework for a streamline-based probabilistic index of connectivity (PICo) using a structural interpretation of MRI diffusion measurements", J. Magn. Reson. Imaging, vol. 18(2), pp. 242-254, 2003.

C. Poupon, C.A. Clark, V. Frouin, J. Régis, I. Bloch, D. Le Bihan and J. Mangin, "Regularization of diffusion-based direction maps for the tracking of brain white matter fascicles", Neuroimage, vol. 12(2), pp. 184-95, 2000.

K. Rohr, H.S. Stiehl, R. Sprengel, T.M. Buzug, J. Weese, Kuhn, and M.H., "Landmark-based elastic registration using approximating thin-plate splines", IEEE Trans. Med. Imag., vol. 20(6), pp. 526-534, 2001.

J. Ruiz-Alzola, C. Westin, S. Warfield, A. Nabavi, and R. Kikinis, "Nonrigid registration of 3D scalar, vector and tensor medical data", Med. Image Comput. Computer-Assisted Intervention (MICCAI) 2000, pp.541-550, 2000.

J. Ruiz-Alzola, C.-F.Westin, S.Warfield, C. Alberola, S. Maier, and R. Kikinis, "Nonrigid registration of 3D tensor medical data," Med. Image Anal., vol. 6, pp. 143–161, 2002.

J.S. Shimony, A.Z. Snyder, N. Lori and T.E. Conturo,"Automated fuzzy clustering of neuronal pathways in diffusion tensor tracking", ISMRM, 2002.

E.O. Stejskal and J.E. Tanner, "Spin Diffusion Measurements: Spin Echoes in the Presence of a Time-Dependent Field Gradient", J. Chem. Phys., vol. 42, pp. 288, 1965.

B. Stieltjes, W.E. Kaufmann, P.C.M. van Zijl, K. Fredericksen, G.D. Pearlson, S. Mori, "Diffusion tensor imaging and axonal tracking in the human brainstem", NeuroImage, vol. 14, pp. 723-735, 2001.

N. Tzourio-Mazoyer, B. Landeau, D. Papathanassiou, F. Crivello, O. Etard, N. Delcroix, B. Mazoyer, M. Joliot, "Automated anatomical labeling of activations in SPM using a macroscopic anatomical parcellation of the MNI MRI single-subject brain", Neuroimage, vol. 15, pp. 273—289, 2002.

D.S. Tuch, T.G. Reese, A.M. Dale, J.S. George, J.W. Belliveau and V.J. Wedeen, "High angular resolution diffusion imaging reveals intra-voxel white matter fiber heterogeneity", Magn. Reson. Med., vol. 48, pp. 577-582, 2002.

D.S. Tuch, T.G. Reese, M.R. Wiegell and V.J. Wedeen, "Diffusion MRI of complex neural architecture", Neuron, vol. 40, pp. 885-895, 2003.

W. Van Hecke, A. Leemans, E. D'Agostino, S. De Backer, E. Vandervliet, P.M. Parizel, J. Sijbers, "Nonrigid Coregistration of Diffusion Tensor Images Using a Viscous Fluid Model and Mutual Information", IEEE Trans. Med. Imag., vol.26(11), pp.1598-1612, 2007.

S. Wakana, H. Jiang, L.M. Nagae-Poetscher, P.C. van Zijl and S. Mori, "Fiber tract-based atlas of human white matter anatomy", Radiology, vol. 230(1), pp. 77-87, 2004.

D.M. Weinstein, G.L. Kindlmann and E.C. Lundberg, "Tensorlines: Advection-Diffusion based Propagation through Diffusion Tensor Fields", 10th IEEE Visualization 1999 (VIS '99) pp. 40, 1999.

C. Wernicke, “Grundrisse der Psychiatrie”, Thieme, Leipzig, 1906.

Y. Xia, U. Turken, S.L. Whitfield-Gabrieli, and J.D. Gabrieli, “Knowledge-based classification of neuronal fibers in entire brain,” Med. Image Comput. Computer-Assisted Intervention (MICCAI) 2005, pp. 205–212, 2005.

D. Xu, S. Mori, D. Shen, P.C.M. van Zijl and C. Davatzikos, "Spatial normalization of diffusion Tensor Fields", Magn. Reson. Med., vol. 50, pp. 175-182, 2003.

Q. Xu, A.W. Anderson, J.C. Gore and Z. Ding, “Unified bundling and registration of brain white matter fibers”, IEEE Trans. Med. Imaging, vol. 28(9), pp. 1399-1411, 2009.

F. Zhang, C. Goodlett, E. Hancock and G. Gerig, "Probabilistic fiber tracking using particle filtering", Med. Image Comput. Computer-Assisted Intervention (MICCAI) 2007, pp. 144-152, 2007.

H. Zhang, P.A. Yushkevich, and J.C. Gee, "Deformable registration of diffusion tensor MR images with explicit orientation optimization", Med. Image Comput. Computer-Assisted Intervention (MICCAI) 2005, pp. 172-179, 2005.

H. Zhang, P. Yushkevich, D. Alexander, and J. Gee, “Deformable registration of diffusion tensor MR images with explicit orientation optimization,” Med. Image Anal., vol. 10(5), pp. 764–785, 2006.

S. Zhang and D. Laidlaw, “Hierarchical Clustering of Streamtubes”, technical report, Dept. of Computer Science, Brown Univ., 2002.

S. Zhang and D.H. Laidlaw, “DTI Fiber Clustering and Cross-Subject Cluster Analysis”, ISMRM, 2005.

S. Zhang, S. Correia, D.F. Tate, and D.H. Laidlaw, “Correlating DTI Fiber Clusters with White-Matter Anatomy”, ISMRM, 2006.

S. Zhang, S. Correia, and D.H. Laidlaw, "Template-based Automatic DTI Fiber Bundle Labeling", ISMRM, 2007.

S. Zhang, S. Correia, and D. H. Laidlaw, "Identifying white-matter fiber bundles in DTI data using an automated proximity-based fiber-clustering Method", IEEE T. Vis. Comput. Gr, vol. 14, pp. 1044-1053, 2008.

U. Ziyan, M.R. Sabuncu, L.J. O’Donnell, and C.F. Westin, “Nonlinear registration of diffusion MR Images based on fiber bundles”, Med. Image Comput. Computer-Assisted Intervention (MICCAI) 2007, pp. 351-358, 2007.